EXPERIMENTAL INVESTIGATION OF THE DIAMETER EFFECT ON HEAT TRANSFER CHARACTERISTICS OF SUPERCRITICAL $CO_2$ FLOWS THROUGH HORIZONTAL MICROTUBES

by

Efe Öztabak

Submitted to Graduate School of Natural and Applied Sciences

in Partial Fulfillment of the Requirements

for the Degree of Master of Science in

Mechanical Engineering

Yeditepe University

2022

EXPERIMENTAL INVESTIGATION OF THE DIAMETER EFFECT ON HEAT TRANSFER CHARACTERISTICS OF SUPERCRITICAL $CO_2$ FLOWS THROUGH HORIZONTAL MICROTUBES

APPROVED BY:

Prof. Dr. Erdem An ………………………………
(Thesis Supervisor)
(Yeditepe University)

Assoc. Prof. Dr. Ali Bahadır Olcay ………………………………
(Yeditepe University)

Assoc. Prof. Dr. Mehmed Rafet Özdemir ………………………………
(Marmara University)

DATE OF APPROVAL: …./…./20…

I hereby declare that this thesis is my own work and that all information in this thesis has been obtained and presented in accordance with academic rules and ethical conduct. I have fully cited and referenced all material and results as required by these rules and conduct, and this thesis study does not contain any plagiarism. If any material used in the thesis requires copyright, the necessary permissions have been obtained. No material from this thesis has been used for the award of another degree.

I accept all kinds of legal liability that may arise in case contrary to these situations.

Name, Last name ……………………………………

Signature …..……………….……………………..

# ACKNOWLEDGEMENTS

Professor Erdem An (Hojin Ahn) has been an ideal teacher, mentor, and thesis supervisor, offering encouragement and advice with a perfect attitude. I'm proud of, and grateful for, my time working with him. All the things I have learned during the time that I've spent with him, are invaluable.

I thank my lab mate Oğuzhan Gökkaya for all the good times that we had during the course of two years. This project couldn't have been this much enjoyable without him. The help of undergraduate assistants, Ceren Özçakır and Mehmet Mert Dinç, and our workshop technician, Emirhan Şayhan, is also much appreciated. This thesis has been prepared as a part of the TÜBİTAK-1001 (119M051) project, and I am thankful for the support and funding of TÜBİTAK.

Finally, I would like to thank my mom, Saliha, and my dad, Mustafa, for their endless love and support, making everything easier and more beautiful in my life.

# ABSTRACT

## EXPERIMENTAL INVESTIGATION OF THE DIAMETER EFFECT ON HEAT TRANSFER CHARACTERISTICS OF SUPERCRITICAL $CO_2$ FLOWS THROUGH HORIZONTAL MICROTUBES

Experimental study on convective heat transfer through microtubes encounters many challenges such as measuring the wall temperature of the tube with a reasonable uncertainty, relatively high heat loss from the outer surface of the tube, and difficulty in measuring the fluid bulk temperature at the tube outlet. These issues become exacerbated with the flow at low Reynolds numbers. The present study presents a new method to measure the tube wall temperature with a small solder cast where a thermocouple is embedded. The net heat flux to flows, determined by the heat loss on the outer surface and the axial heat conduction, is integrated to obtain the local mean enthalpy of fluid and then the mean fluid temperature along the tube. Thus, convection heat transfer coefficients are calculated without measuring the mean temperature at the outlet. The new method is successfully validated with laminar water flows through a horizontally configured microtube, 0.501 mm in inner diameter. All Nusselt numbers are found to lie between 4.36 and 4.36 + 10 percent. Then, the new method was applied to supercritical carbon dioxide flows through horizontal microtubes with inner diameters of 0.317, 0.509, and 0.847 mm at 8.0 MPa. The inlet Reynolds number was kept lower than 1100 in all tests to examine the supercritical carbon dioxide at low Reynolds numbers. A peak in the Nusselt number was observed when the fluid temperature is near the pseudo-critical temperature. The heat transfer enhancement at the pseudo-critical temperature was associated with three mechanisms such as high specific heat, a high temperature gradient near the wall, and buoyancy-induced secondary flow in the transverse direction. Finally, the results show that the magnitudes of the Nusselt number increase with an increasing diameter since the effect of buoyancy significantly rises with the diameter.

# ÖZET


## YATAY MİKROTÜPLER İÇERİSİNDEKİ SÜPERKRİTİK $CO_2$ AKIŞLARINDA ÇAPIN ISI TRANSFERİ KARAKTERİSTİĞİ ÜZERİNDEKİ ETKİSİNİN DENEYSEL OLARAK İNCELENMESİ

Mikrotüpler için taşınım yoluyla ısı transferi üzerine yapılan deneysel çalışmalarda; makul bir belirsizlikle tüpün duvar sıcaklığının ölçülmesi, tüpün dış yüzeyinden nispeten yüksek ısı kaybı ve tüp çıkışındaki ortalama akışkan sıcaklığının ölçülmesi gibi birçok zorlukla karşılaşılmaktadır. Bu sorunlar, düşük Reynolds sayılarındaki akışlarda daha da kötüleşmektedir. Bu çalışma, bir termokuplın gömülü olduğu küçük bir lehim dökümü ile tüp duvar sıcaklığını ölçmek için yeni bir yöntem sunmaktadır. Dış yüzeydeki ısı kaybı ve eksenel yöndeki ısı iletimi ile belirlenmiş olan akışlara sağlanan net ısı akısı, sıvının bölgesel ortalama entalpisini ve ardından boru boyunca ortalama akışkan sıcaklığını elde etmek için entegre edilmiştir. Böylece, çıkıştaki ortalama akışkan sıcaklığı ölçülmeden taşınımla ısı transferi katsayıları hesaplanmıştır. Yeni yöntemin doğrulaması, 0,501 mm iç çapa sahip yatay olarak konumlandırılmış bir mikrotüp içinden laminer su akışları geçirilerek yapılmıştır. Tüm Nusselt sayılarının 4,36 ile 4,36 + yüzde 10 arasında olduğu bulunmuştur. Daha sonra, yeni yöntem 8,0 MPa'da 0,317, 0,509 ve 0,847 mm iç çaplara sahip yatay mikrotüplerden geçen süperkritik karbondioksit akışlarına uygulanmıştır. Süperkritik karbondioksiti düşük Reynolds sayılarında incelemek için tüm testlerde girişteki Reynolds sayısı 1100'den düşük tutulmuştur. Akışkan sıcaklığı, sözde kritik sıcaklığa yakın olduğunda Nusselt sayısında bir maksimum gözlemlenmiştir. Sözde kritik sıcaklıktaki ısı transferi artışı, yüksek özgül ısı, duvara yakın bir yüksek sıcaklık gradyanı ve enine yönde kaldırma kuvvetinin neden olduğu ikincil akış gibi üç farklı mekanizma ile ilişkilendirilmiştir. Son olarak kaldırma kuvvetinin etkisi çap ile birlikte önemli ölçüde arttığından, sonuçlar Nusselt sayısının büyüklüklerinin artan çapla birlikte arttığını göstermektedir.

# TABLE OF CONTENTS

## LIST OF FIGURES

# LIST OF TABLES

## LIST OF SYMBOLS

| | |
|---|---|
| $A_c$ | cross-sectional area of the tube wall ($m^2$) |
| $c_p$ | specific heat (kJ/kg·K) |
| $d$ | diameter (m) |
| $g$ | gravitational acceleration ($m/s^2$) |
| $G$ | mass flux ($kg/m^2s$) |
| $h$ | specific enthalpy (kJ/kg) |
| $htc$ | heat transfer coefficient ($W/m^2 \cdot K$) |
| $I$ | current (A) |
| $k$ | thermal conductivity (W/m·K) |
| $K$ | loss coefficient (-) |
| $L$ | length (m) |
| $m$ | parameter representing $hp/kA_c$ ($m^{-1}$) |
| $\dot{m}$ | mass flow rate (kg/s) |
| $P$ | perimeter (m) |
| $q$ | heat rate (W) |
| $q''$ | heat flux ($W/m^2$) |
| $\dot{q}$ | volumetric heat generation ($W/m^3$) |
| $r$ | radius (m) |
| $R$ | electrical resistance (Ω) |
| $V$ | mean velocity (m/s) |
| $T$ | temperature (°C) |

*Dimensionless numbers*

| | |
|---|---|
| $Gz$ | Graetz number (-) |
| $Nu$ | Nusselt number (-) |
| $Pr$ | Prandtl number (-) |
| $Ra$ | Rayleigh number (-) |
| $Re$ | Reynolds number (-) |
| $Ri$ | Richardson number (-) |

*Greek symbols*

| | |
|---|---|
| $\alpha$ | kinetic energy correction factor (-) |
| $\beta$ | volume expansivity (1/K) |
| $\mu$ | dynamic viscosity (Pa·s) |
| $v$ | kinematic viscosity ($m^2/s$) |
| $\rho$ | density ($kg/m^3$) or electrical resistivity (Ω·m) |

*Subscripts*

| | |
|---|---|
| *0* | reference |
| *ave* | average |
| *cond* | conduction |
| *d* | diameter |
| *f* | evaluated at the film temperature |
| *fd* | fully-developed |
| *i* | inner |
| *in* | inlet |
| *i+* | inner side between $x$ = 0 and $L$ |
| *i-* | inner side between $x$ = -$L$ and 0 |
| *k* | index |
| *m* | evaluated at the mean temperature |
| *net* | net |
| *o* | outer |
| *out* | outlet |
| *pc* | pseudo-critical |
| *s* | solder cast |
| *tp* | thermal paste |
| *w* | wall |
| *wi* | inner wall |
| *wo* | outer wall |
| *x* | location |
| ∞ | ambient or free stream |

*Superscripts*

| | |
|---|---|
| * | dimensionless |

# 1. INTRODUCTION

The end point of the phase equilibrium curve is defined as the critical point in thermodynamics. When the temperature and pressure of any substance are at or above its critical point, it means that this substance is in the supercritical region where it is neither a liquid nor gas. If the pressure exceeds the critical pressure, the critical temperature is defined as the pseudo-critical temperature since it is not exactly at its critical pressure. Moreover, the utilization of supercritical fluids as a working fluid is very important due to their superior properties. Firstly, the specific heat is very high near the critical point which means more heat can be dissipated by the fluid. Thus, efficiencies in the thermodynamic cycles can be raised by operating them at supercritical conditions rather than in the subcritical region. Secondly, there is no phase change in the supercritical region which is very essential and desirable for the heat exchanger designs.

$CO_2$ is a low-cost and environment-friendly refrigerant with its low ozone depletion potential (ODP) and global warming potential (GWP). Furthermore, the critical temperature and pressure of carbon dioxide ($CO_2$) are 31.0°C and 7.38 MPa, respectively. The low critical pressure and temperature of $CO_2$ in comparison with other common working fluids, such as water (374°C and 22.1 MPa), make it a more desirable candidate fluid since it is easier to reach these pressure and temperature values.

The pseudo-critical temperature of $CO_2$ is 34.7°C at 8.0 MPa where all the tests were conducted in this thesis. Thermophysical properties experience a dramatic change near the critical point and one example of this is given in Figure 1.1 for $CO_2$ at 8.0 MPa between 0 and 100°C. As mentioned before, the specific heat rapidly rises and drops around the pseudo-critical temperature. Density and dynamic viscosity monotonously decrease as the temperature increases but they experience a rapid drop at the pseudo-critical temperature. The thermal conductivity also monotonously decreases except for a little peak at the pseudo-critical temperature. Although it is not presented here, the Prandtl number and volume expansivity experience a peak at the pseudo-critical temperature similar to the specific heat. When the $CO_2$ is heated at supercritical pressures, the variation of properties near the critical point leads to changes in flow characteristics as follows. The mean fluid temperature changes slowly because of high specific heat, thermal acceleration and buoyancy effects appear due to the density, and the Reynolds number increases rapidly due to viscosity.

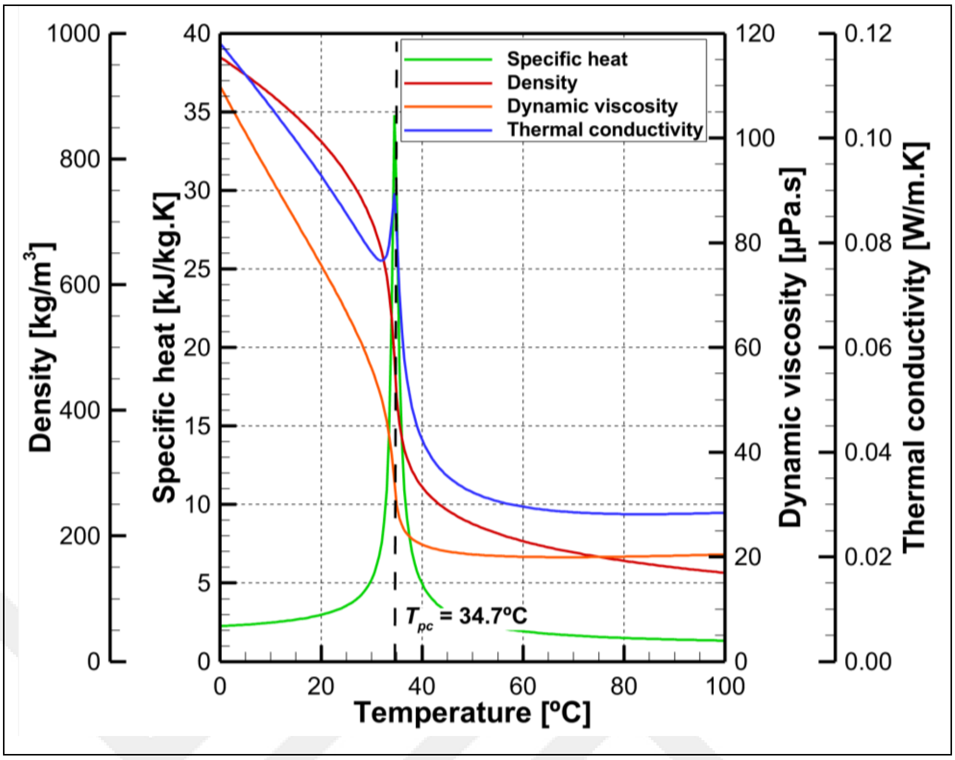


Figure 1.1. The variation of thermophysical properties (specific heat, density, dynamic viscosity, and thermal conductivity) of supercritical carbon dioxide at 8.0 MPa between 0 and 100ºC. The vertical black dashed line indicates the pseudo-critical temperature at 8.0 MPa ($T_{pc}$ = 34.7°C).

Heat transfer characteristics of flows through microtubes have extensively been investigated during the last two decades in response to the growing need to cool microdevices. Because convection heat transfer coefficient generally increases with decreasing diameter, microtubes may be able to dissipate a heat flux of up to 1000 W/cm$^2$ whereas the heat dissipation capacity of the conventional tubes is less than 20 W/cm$^2$ [1]. Furthermore, recent development to employ supercritical carbon dioxide ($sCO_2$) as a working fluid to cool electronic devices necessitates studies on characteristics of heat transfer and pressure drop of $sCO_2$ flows in microtubes. However, very little experimental data with low uncertainties are available in the literature regarding heat transfer in $sCO_2$ flows through tubes with a diameter of less than 1 mm. This thesis discusses difficulties in conducting heat transfer tests in a circular tube at the microscale, especially in laminar flow, and presents a novel method to overcome those difficulties and its application to study $sCO_2$ flows through a microtube.

I've organized the rest of the thesis as follows. Firstly, the development of the new technique to measure the tube wall temperature is described in detail. Then the validation process of the proposed method by heat transfer tests using laminar water flows is presented. A rigorous method to analyze data is discussed, which includes (1) non-uniform heat generation in the tube by electric current as the resistivity of the tube wall varies with the wall temperature, (2) local heat loss estimation from the outer surface of the tube, and (3) calculation of the mean temperature in the axial direction as it is impossible to measure the mean temperature at the tube outlet with low uncertainty, and (4) the effect of the solder cast on heat loss augmentation and axial conduction along the wall. Then, the new method was applied to study the heat transfer characteristics of horizontal $sCO_2$ flows through microtubes with inner diameters of 0.317, 0.509, and 0.847 mm. Heat transfer characteristics were examined for each diameter individually, and a comparison was made between different diameters. Finally, the effect of buoyancy on heat transfer activity was discussed.

# 2. LITERATURE SURVEY

In this section, the review of the wall temperature measurement methods available in the literature is given firstly, and the difficulties in conducting heat transfer tests in a circular tube at the microscale are discussed. Then, the general heat transfer characteristics of horizontal single-phase and supercritical flows are explained both at a macro-and microscale.

Most of the convection heat transfer experiments attempt to establish either constant surface temperature or constant surface heat flux boundary conditions. Bucci et al. [2] attempted to obtain the boundary condition of constant temperature at the tube surface by heating the microtubes with water vapor condensing on the outer surface of the tube, thus maintaining the wall temperature at the saturation temperature of the water. Though the heat transfer coefficient of water vapor condensation may be very high, however, it still reduces the overall heat transfer coefficient between the vapor and the fluid inside the tube. The constant surface heat flux boundary condition can be obtained either by applying direct current (DC) or alternating current (AC) directly to the tube wall or by wrapping the outer surface of the tube with a heating element. However, applying electric current to the tube may not provide the constant heat flux in a strict sense because the electrical resistance of the tube wall is a function of the wall temperature, and the tube wall temperature increases from the tube inlet to the outlet in a heating mode. For example, heat flux may vary from the tube inlet to the outlet by approximately 3 percent for a stainless-steel tube if the tube wall temperature rises from the tube inlet to the outlet by an order of 40°C.

One of the most challenging techniques in convective heat transfer experiments is the measurement of tube wall temperatures. The most popular way to measure the wall temperature is using thermocouples. Meyer and Everts [3] drilled 0.3-mm indentations into the copper tube, 11.5 mm in diameter, and then soldered thermocouples into the indentations. The outer wall of the tube was electrically insulated by using the Kapton adhesive tape and the tube wall is wrapped by a heating element. Another method used in [3] was that the stainless-steel tube, 4 mm in diameter, was drilled to create 0.5 mm indentations into which thermocouples were glued using the thermal adhesive with thermal conductivity of 9 W/m·K. The thermal adhesive also provided electrical insulation between the thermocouples and the tube wall, and the tube was heated by an electric current. Two important principles in their methods were to create an indentation that would provide more contact area between the tube wall and the thermocouple, and to insulate thermocouples from electric current. Some studies [4–7] welded thermocouples directly to the tube wall with no electrical insulation between the thermocouples and the tube wall. However, when an electric current is applied to the tube on which thermocouples are attached with no electrical insulation, the electric current leakage on the thermocouple tip would be experienced, resulting in inaccurate temperature measurements [8]. It was also observed that, when a thermocouple is soldered directly to the tube wall, electric current passing through the tube wall also flows through the solder at the tip of the thermocouple, thus creating electric potential over a very small electrical resistance of solder between two dissimilar metal wires of the thermocouple. This electric potential interferes with an electromotive force induced by the temperature difference between the tube wall and the junction in the data acquisition system, causing an erroneous temperature measurement. Some studies attempted to attach thermocouples to the tube wall by clamping them to the wall [9] or by applying thermal adhesives [10]. On the other hand, a number of the studies are not much informative on how they exactly attach thermocouples to the tube wall.

When a tube diameter becomes less than 1 mm, the tube wall temperature measurement faces more challenges due to its small dimension and vulnerable structure. Consequently, a tube, less than 1 mm in diameter, is often referred to as a microtube or mini-tube in the literature [11,12,14-21]. Jiang et al. [11] welded thermocouples to a tube, 0.27 mm in inner diameter and 1.59 mm in outer diameter. Sadaghiani and Koşar [12] used a thermal epoxy to attach thermocouples to microtubes whose outer diameters were 0.9 mm and 1.1 mm. The method of liquid crystal thermography was for the first time employed by Cooper et al. [13] to measure the surface temperature of the tube wall for their study on convective heat transfer. This non-contacted liquid crystal thermography method was then applied to investigate convective heat transfer in microtubes used by Muwanga and Hassan [14], Lin and Yang [15], and Yang et al. [16]. In order to overcome the difficulty of attaching thermocouples to the tube wall with electrical insulation, Baek et al. [17] soldered thermocouples directly to a microtube, 0.310 mm in outer diameter, and heated the tube by a heating element wrapped over the electrically insulated microtube. Thus, the electric current did not affect temperature measurement by the thermocouples. On the other hand, Wang et al. [18, 19] attempted to create the constant surface heat flux boundary condition as follows. A microtube, 1.6 mm in outer diameter, was covered by a copper cylinder that had cuts to insert thermocouples. Then the heat was supplied by electric current passing through another cylinder that covered the copper cylinder. Though experimental studies on convective heat transfer in microtubes have been attempted as mentioned above, it is not easy to find studies with low uncertainties in temperature measurement. It is especially true of flow at low Reynolds numbers.

A review article by Rosa et al. [20] extensively discusses the scaling effects as a tube diameter reduces to a micro-scale. Some scaling effects such as entrance effects, conjugate heat transfer, viscous heating, and surface roughness, often negligible in conventional tubes, become more significant for the microtubes, and measurement uncertainties may grow due to its reduced dimension. For example, Yang and Tin [21] showed that the entrance length for the microtubes is larger than that presented by a correlation for a tube with a large diameter, $L_T = 0.05Re_d Pr \cdot d_i$ in the textbook [22]. In order to decide whether the conjugate heat transfer is taken into account or not, Maranzana et al. [23] proposed a criterion. When these effects are properly taken into account, however, Rosa et al. conclude that the standard theories and correlations developed for tubes with large diameters may also be applicable to describe heat transfer characteristics in microtubes.

An experimental study with a circular tube in a microscale must overcome many obstacles that could be easily handled for a large tube. First, the size of commercial thermocouples is relatively large compared to the tube size. It is physically difficult to place thermocouples on a circular tube in a microscale. Furthermore, it is not easy to reduce the thermal contact resistance between the thermocouple and the microtube wall. When the thermal contact resistance is high, the free convection heat transfer rate from the surface of the thermocouple to the surrounding air is relatively high compared to heat conduction from the tube wall to the thermocouple, resulting that the thermocouple measures lower than what it should, for the case of the tube being heated. A conventional method to reduce the thermal contact resistance is to drill an indentation to the tube wall where a thermocouple is placed. However, this method cannot be applied to a microtube because of the small tube diameter and the thin wall. One way to reduce the thermal contact resistance between the thermocouple and the tube wall would be to solder the thermocouple to the wall directly. However, when the tube is heated by electric current, electric potential due to the current over the two wires of the thermocouple causes erroneous temperature measurement. The use of adhesive with high thermal conductivity may not be easy because the curing time of thermal adhesive is generally long and it is very difficult to hold the thermocouple fast to the microtube wall for a long time.

For turbulent flow, heat loss from the tube’s outer surface to the environment may be an order of a few percent of the total energy input. At a low Reynolds number, on the contrary, the ratio of the surface heat loss to the total energy is much higher and cannot be neglected in the data reduction process. However, the reduced dimension of a microtube makes it almost impossible to provide thermal insulation on its outer surface. It is because the critical radius of insulation, *k/h*, can be much larger than the tube radius and thus thermal insulation over the thermocouple and the tube wall may rather increase heat loss.

On the other hand, the accurate measurement of mean fluid temperature at the tube outlet is extremely difficult. The mean or bulk temperature of the fluid at the outlet is usually measured in a mixing chamber located at the outlet by a PT100 or a thermocouple. However, the size of the mixing chamber relative to the tube size is very large and thus the thermal mass of the mixing chamber is also very large compared to the enthalpy flux of flow through the microtube. Therefore, it would take very long to reach a steady-state mean temperature in the mixing chamber. Even if it reaches a steady-state mean temperature, it may be measured to be lower than what it should be, due to relatively large heat loss from the fluid to the mixing chamber wall and then to the surroundings.

Moreover, the thickness of a microtube wall is relatively large compared to its diameter. Consequently, when the tube is heated by an electric current, the temperature difference between the tube's outer surface and the inner surface tends to be larger than that encountered in a tube with a large diameter. In addition, heat conduction in the axial direction along the tube may have to be taken into consideration due to the relatively large cross-sectional area of the tube wall compared to the flow area. All these situations significantly increase measurement uncertainties.

It is more appropriate to understand the heat transfer characteristics of horizontal single-phase flows prior to supercritical flows since the strong property variations make them more complicated. Mori et al. investigated horizontal single-phase flows under constant heat flux boundary condition both experimentally [24] and theoretically [25]. They used air as a working fluid in a pipe with an inner diameter of 35.6 mm and their findings are as follows. If the product of $Re \cdot Ra$ is greater than $10^4$, a secondary flow caused by buoyancy becomes stronger in the transverse direction and forms vortices. For laminar flows, the velocity and temperature profile are affected by the secondary flow which makes them quite different from than Poiseuille flow when $Re{\cdot}Ra$ is large. The effect of secondary flows on the Nusselt number appears when $Re{\cdot}Ra$ is about $10^3$ in the laminar flow regime. However, it was shown that the effect of secondary flow on temperature and velocity profiles, and the Nusselt number is very small for turbulent flows. As mentioned above, the buoyancy in the transverse direction is significant for horizontal flows. Jackson et al. [26] and Kakac [27] theoretically proved that if $Gr/Re^2$ is less than 0.001 for horizontal channels, the buoyancy becomes insignificant.

The interest to investigate heat transfer characteristics of $sCO_2$ flows has arisen in the last years due to its applications to the Brayton power cycle [28, 29], cooling solutions in nuclear industries [29], and printed-circuit heat exchangers [30–32]. It is a great challenge to fully understand the cooling and heating of $sCO_2$ since the thermophysical properties rapidly change near the critical point. $sCO_2$ flows can be classified by the tube size (microtubes or conventional tubes), flow direction (horizontal, upward, or downward), boundary condition (constant heat flux or constant wall temperature) and flow regime (laminar or turbulent).

Although this thesis investigates heat transfer characteristics under constant heat flux boundary condition, it is beneficial to review studies with constant wall temperature and cooling applications. Liao and Zhao [33] studied $sCO_2$ flows flowing in horizontal tubes under constant wall temperature experimentally. The diameters of the tubes are ranging from 0.50 to 2.16 mm and all tests are conducted in the turbulent flow regime. They showed that the magnitudes of the Nusselt number increase with an increasing diameter due to the buoyancy effects. Yang et al. [34] numerically investigated the mixed convection through microtubes cooled at a constant temperature at various inclination angles. The diameter and length of the microtube are 0.5 mm and 1000 mm, respectively. In their study, horizontal laminar flows exhibited the largest heat transfer coefficients among other inclination angles. A numerical study by Cao et al. [35] investigated laminar convective heat transfer of $sCO_2$ in horizontal circular and triangular tubes. Flows with hydraulic diameters less than 1 mm under cooling condition were simulated. They found that the buoyancy is significant for horizontal flows and it enhances the heat transfer. Also, the secondary flow formed as a result of buoyancy distorts the temperature and velocity profiles.

Apart from cooling applications, there are many heating applications in the literature for inner diameters greater than 1 mm. Yu et al. [36] experimentally investigated the effect of buoyancy on supercritical water flowing in horizontal tubes. The diameters of the tubes are 26 and 43 mm and experiments were conducted in the turbulent flow regime. They found that the heat transfer characteristics are quite different at the top and bottom surfaces due to the buoyancy. As a result, heat transfer deterioration was observed at the top surface whereas heat transfer was enhanced at the bottom surface. In their study, the buoyancy effects become insignificant as the mass flux increases or inner diameter increases. Kim et al. [37] have reported the same conclusion as [36] for $sCO_2$ flows through a horizontal tube that has an inner diameter of 7.75 mm. Also, a recent experimental study [38] with $sCO_2$ flows through a horizontal tube with inner diameters of 4 and 8 mm concluded the same observations. Different from the previous studies, Zhang and Yamaguchi [39] numerically investigated laminar $sCO_2$ flows in a tube having a diameter of 6.0 mm. They stated that the buoyancy is not significant because $Gr/Re^2$ is less than 0.1 in contrast to the criterion proposed by [27]. They reasoned the heat transfer enhancement at the pseudo-critical temperature with three important points. Firstly, the temperature gradient is high and the boundary layer is thinner near the wall. Secondly, the rapid rise in the specific heat and drop in viscosity are effective. Finally, the flow does not become neither hydrodynamically nor thermally fully-developed along the tube, and this makes the flow turbulent.

Although there are some studies with a vertical configuration, fewer studies were found for horizontal microtubes. Wang et al. [40] experimentally investigated the turbulent $sCO_2$ flows through horizontally configured microtubes with inner diameters of 0.50, 0.75, and 1.00 mm. They showed that a higher mass flux results in heat transfer enhancement and heat transfer coefficients become higher as the inner diameter decreases. Also, the best heat transfer performance was observed when the outlet temperature is close to the pseudo-critical temperature. There are two numerical studies on laminar flow in horizontal microtubes [41, 42]. They both observed a dip before the peak of the Nusselt number at the pseudo-critical temperature. Also, they showed that the Nusselt number converges to 4.364 after the peak location. Finally, the heat transfer characteristics of supercritical carbon dioxide ($sCO_2$) at 8.0 MPa through a microtube, 0.509 mm in diameter, have experimentally been investigated under the constant heat flux boundary condition in our conference paper [43]. We studied the effect of three different flow configurations (namely, horizontal, upward, and downward flows) on heat transfer activity for both laminar and turbulent flow regimes. For laminar flow, the behavior of the Nusselt number is found to be highly dependent on the flow configuration and thus on the direction of the buoyancy force. For horizontal flows, only a single peak of the Nusselt number is observed. For downward flow, however, three peaks of the Nusselt number appear as the mass flux increases, while the Nusselt number for upward flow is characterized by two peaks at low mass flux. The physical mechanism of the multiple peaks in laminar flow is believed to be the fluid mixing between the wall boundary and core region.

Moreover, we developed a novel method of placing thermocouples onto a microtube [44] which aims to investigate the heat transfer characteristics of $sCO_2$ flows. In the new method to measure the tube wall temperature, a thermocouple is embedded into a small solder cast, which is later placed on the half part of the tube with a thermal paste and an instant adhesive. The details of this method and its application are given in the next sections of this thesis. The ultimate goal of developing the new temperature measurement method is to investigate supercritical carbon dioxide ($sCO_2$) flow at low Reynolds numbers as little experimental data for $sCO_2$ flow in a microtube is available in the literature.

# 3. EXPERIMENTAL METHOD

## 3.1. DEVELOPMENT OF THE NEW METHOD TO ATTACH A THERMOCOUPLE TO THE TUBE WALL

This section describes the new method of placing thermocouples on the wall of a microtube. Two primary aims that the new method desires to achieve in the present study are to reduce the thermal contact resistance between a thermocouple and the tube wall and to provide electrical insulation to the thermocouple from the tube wall as the tube is heated by electric current. One way to reduce the contact resistance between a thermocouple and the tube wall may be to increase the contact area between the two surfaces by drilling an indentation to the tube wall and placing the thermocouple inside the indentation. For a tube in a microscale, however, the tube wall cannot be drilled due to its small dimension. Another way to reduce the thermal contact resistance may be to solder the thermocouple directly to the tube wall. However, direct soldering is not desirable because no electrical insulation is provided between the thermocouple and the tube.

In the present study, therefore, a mold assembly is designed to shape a small piece of solder that covers the upper half of the microtube. Figure 3.1 shows the mold assembly consisting of three parts: (a) the main part of the mold design, (b) the second part of the mold, and (c) the probe to melt the solder. The procedure to make a solder cast is as follows. The probe (c) is placed on an electric stove to heat up to approximately 250°C. Then the microtube (7) and the thermocouples are placed in channels (1) and (2), respectively, such that the thermocouple tips (5) are positioned on the microtube. Next, the bolts are screwed through the holes (3) to fasten up parts (a) and (b). Then a small piece of solder is put on the microtube (6) and the hot probe (4) is pushed down to melt the solder. Finally, the probe is moved out, bolts are loosened up, the microtube is pulled out, and the thermocouple embedded with the solder cast is taken out. Figure 3.2 (a) shows the mold assembly made of aluminum. The resulting solder cast that would cover the upper half of the tube is shown in Figure 3.2 (b). If necessary, the surface of the solder cast is polished with a fine sandpaper. The final dimensions of the solder cast are approximately 2.0 × 2.8 × 1.3 mm.

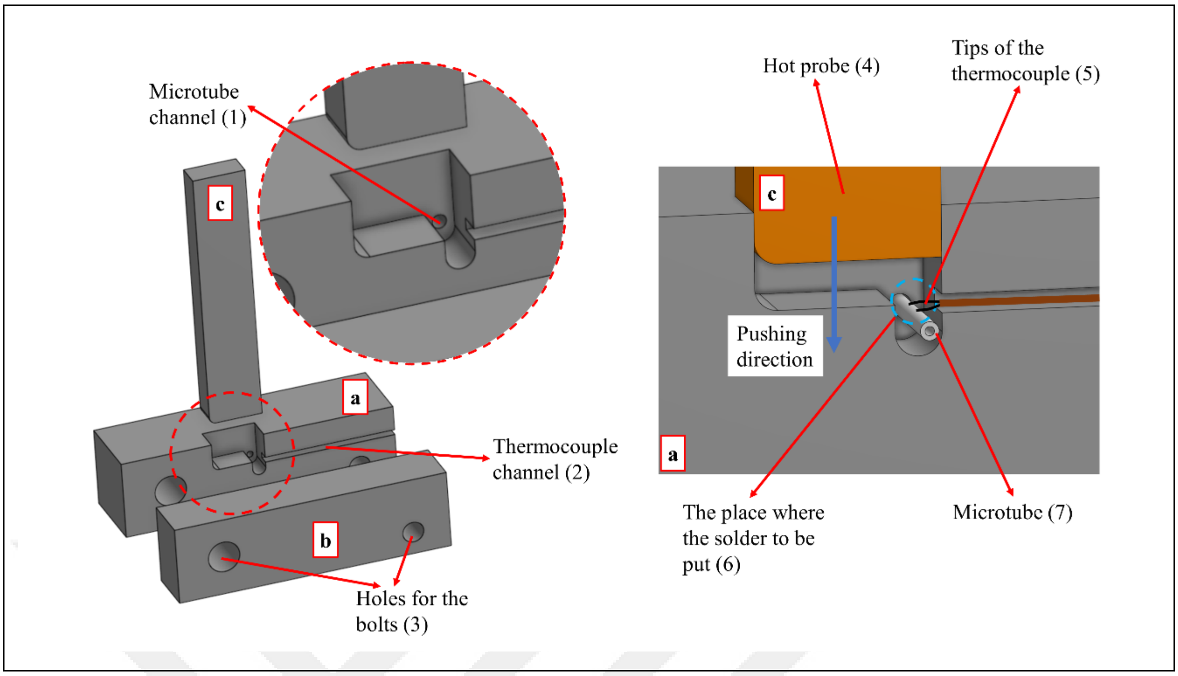


Figure 3.1. Detailed view of the mold design

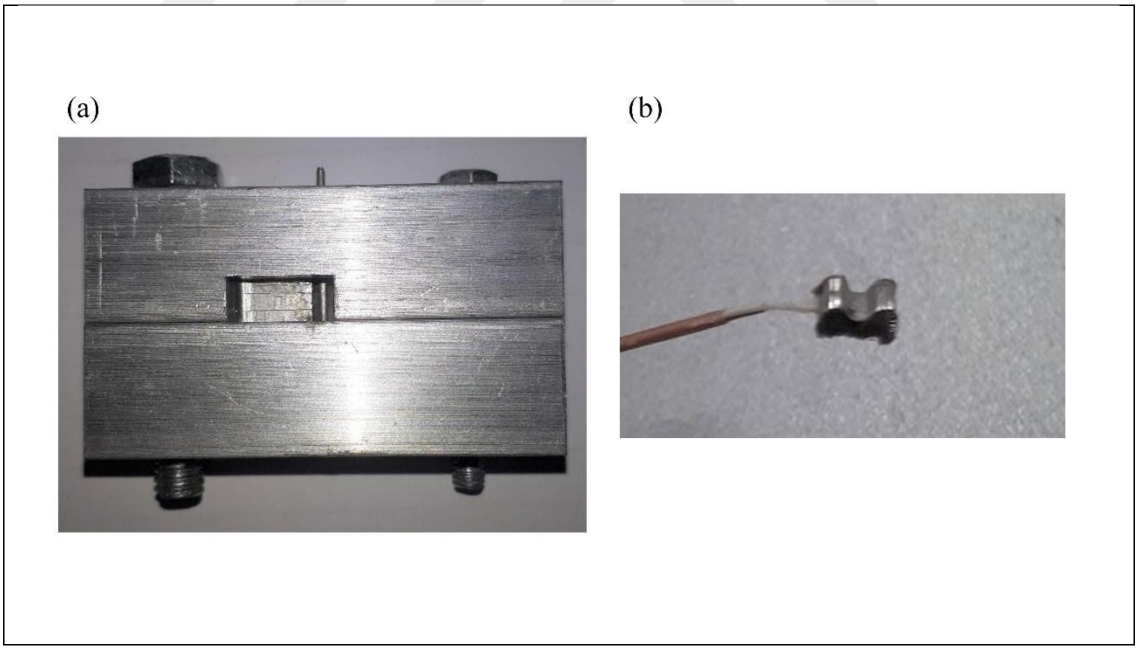


Figure 3.2. (a) The mold assembly manufactured, and (b) the resulting solder cast at the tip of the thermocouple

The process of attaching the produced solder cast to a microtube is shown in Figure 3.3 (a). A thermal paste (Arctic® MX-4, k = 8.5 W/m·K) is applied between the solder cast and the tube. The thermal paste significantly reduces the thermal contact resistance and also provides electrical insulation between the thermocouple and the tube wall. After applying the thermal paste, an instant adhesive (Pattex®) is applied to both sides of the solder cast to fasten it to the tube wall with a curing time of a few seconds. Figure 3.3 (b) shows the view of the thermocouples on a microtube after completion.

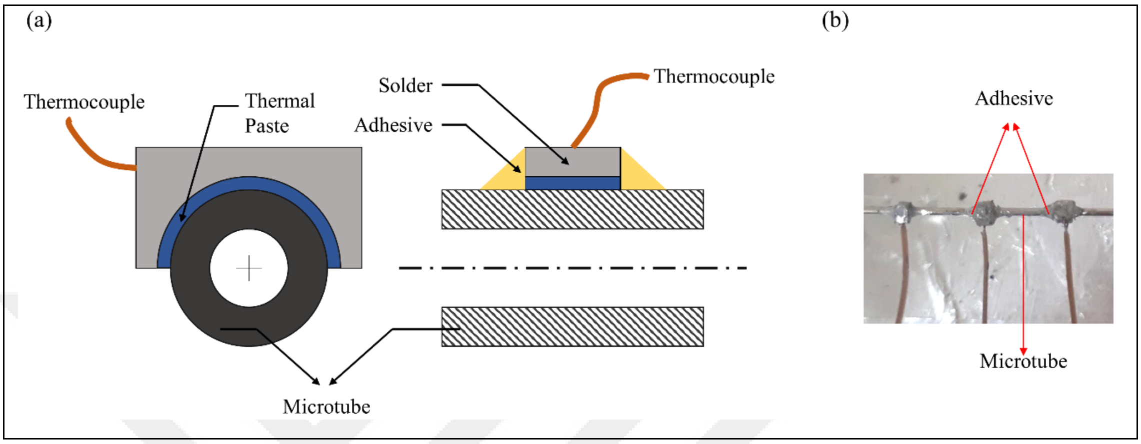


Figure 3.3. (a) Detailed view of attachment process of a thermocouple, and (b) View of thermocouples on the microtube after completion

Solder is selected as a material for the cast because of its high thermal conductivity (approximately 70 W/m°C) which makes the temperature of the cast virtually uniform. Furthermore, its low melting point makes it easy to produce the cast. The use of a thermal paste is preferred to a thermal epoxy, not only because the thermal conductivity of a thermal paste is generally higher than that of a thermal epoxy, but also because the curing time of a thermal epoxy is substantially long. An advantage of using a thermal paste and an instant adhesive together is that the thermal paste and the instant adhesive can be easily taken off from the surface of the tube with no damage to the tube and the same solder casts can be repeatedly used if necessary. However, one drawback is that the instant adhesive appears to lose its adhesiveness for a temperature higher than approximately 120°C. Therefore, the proposed method cannot be used for the wall temperature exceeding 120°C. The validation of the new method is described in Section 4.1.

## 3.2. WATER TEST SETUP

The method of using the solder casts with thermocouples to measure the tube wall temperature has been validated by laminar water flow tests as follows. The validation test employs a stainless steel (304 series) microtube and its inner diameter is calibrated by two methods. One method is to measure the outer diameter by a high-quality microscope and calculate the inner diameter using the length and mass of the tube with the known density of the 304 stainless steel. The tube is assumed to be perfectly circular. The second method is to calculate the inner diameter by allowing laminar water flows through the tube connected to a water tank. The tube is vertically configured and the water tank is open to the atmosphere. The extended Bernoulli equation is applied between the free surface of the water in the tank and the tube outlet as follows.

$$\rho g(H_t + L) = \Delta P_L + \frac{1}{2}(\alpha_{out} + K_{in})\rho V^2 \tag{3.1}$$

where $H_t$ is the water level in the tank, $L$ is the tube length, $\alpha_{out}$ is the kinetic energy correction factor at the tube outlet which is 2.0 for laminar flow, and $K_{in}$ is the loss coefficient at the tube inlet. The frictional pressure loss $\Delta P_L$ is given as $32\mu VL/{d_i}^2$ for a fully developed laminar flow. During this test, the mass flow rate ($\rho\pi d_i^2 V/4$) and $H_t$ are measured, and thus the inner diameter ($d_i$) is calculated from the known viscosity ($\mu$) and density ($\rho$) of water using Equation (3.1). Note that the rougness of the microtube does not affect the results since the tests are conducted in the laminar flow regime. The inner and outer diameters of the tube in the present test are determined to be 0.501 mm and 0.985 mm, respectively. The discrepancy of the inner diameters determined by the two methods is found to be less than 1 percent.

After the calibration of the tube diameter, the water test setup shown in Figure 3.4 has been built to validate the proposed temperature measurement method. The water tank is pressurized by a compressor to achieve desired mass flow rates in the microtube that is configured horizontally. A power supply with extremely low noises provides direct current (DC) to the microtube with the purpose of setting up constant heat flux boundary conditions. Other thin wires are also soldered on the microtube to measure the voltage across the tube, and thus the total power is calculated from the readings of current and voltage. The total 14 T-type thermocouples (Omega® TT-TI-36-SLE) prepared by the proposed method are placed on the microtube to measure local tube wall temperatures with an interval of approximately 25 mm. The total length of the tube is 398 mm while its heated length is 380 mm. In addition, three thermocouples measure the ambient temperature to determine free convection heat loss from the outer surface of the tube, and another thermocouple measures the mean (bulk) temperature of water at the tube outlet.

A very small mixing chamber made of Styrofoam is located at the outlet to measure the bulk temperature of the water. At the beginning of the test, water flow is initiated for approximately 60 seconds without applying current until the tube wall temperatures stabilize, and the average wall temperature from the first three thermocouples at the tube inlet is taken as water temperature at the inlet. Note that the temperatures of the tank, water, and air in the laboratory are kept very close to one another during the test. All the thermocouples and voltage cables are connected to the DAQ system (Keysight® 34972A) and the current that passes through the microtube is measured by the multimeter (Keysight® 34461A). The mass flow rate is measured by using a precise electronic balance (CAS Corp. CUX6200H) which is connected to the computer. Finally, the microtube is enclosed by a radiation shield to reduce the effects of radiation and undesired air disturbance around the tube.

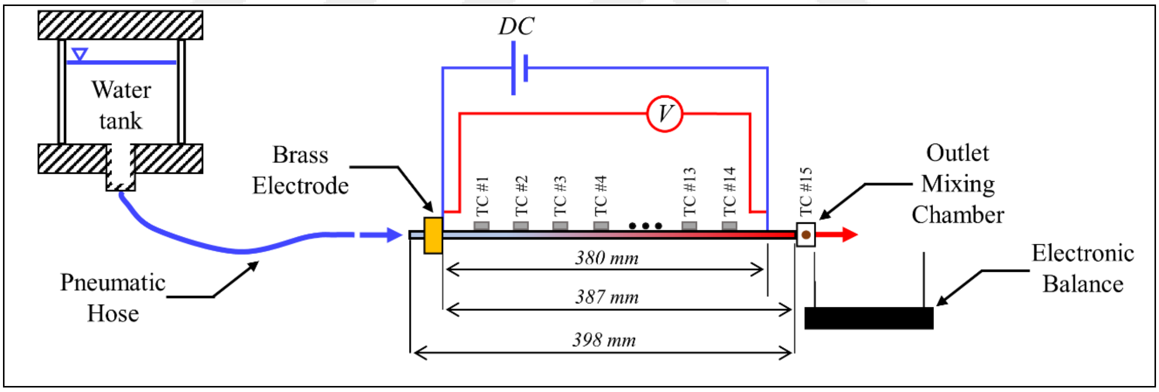


Figure 3.4. Schematic representation of the water test setup

All the thermocouples that are embedded into the small solder casts are placed in a temperature-controlled water bath and calibrated between 10°C and 90°C using a calibrated PT100 sensor. The total uncertainty of temperature measurement is found to be ±0.3°C within a 95 percent confidence level, which includes all uncertainties from the data acquisition (DAQ) system, DAQ cards, thermocouples themselves, and curve fits. The mass flow rate measurement has an accuracy of 1 percent, which is associated with water coming out of the outlet mixing chamber drop by drop.

## 3.3. CARBON DIOXIDE TEST SETUP

The ultimate reason for developing the new method to measure the wall temperature of a microtube has been to investigate the heat transfer characteristics of supercritical $CO_2$ flows near the critical point. Figure 3.5 shows the schematic of the experimental setup, consisting of a $CO_2$ tank, a syringe pump, a flowmeter, a vacuum pump, two absolute pressure sensors, a DC power supply, two DAQ systems, and the test section. In addition, a cooling circulator, not shown in the schematic, controls the $CO_2$ temperature in the tank of the syringe pump. The syringe pump (Teledyne Isco 1000) can be operated either at the constant pressure mode up to 120 bar or at the constant flow rate mode up to 400 mL/min with a sensitivity of 0.1 mL/min. The Coriolis-type flowmeter (Bronkhorst mini CORI-FLOW™ M13) can measure flow rates up to 2000 g/h. The mass flow rate in the system is controlled by a precise needle valve at the outlet of the test section. Moreover, two absolute pressure sensors with a full range of 100 bar and an accuracy of ±0.25 percent are included in the system to obtain pressure data at the upstream and downstream of the test section. A secondary tank provides nearly constant pressure downstream of the test section.

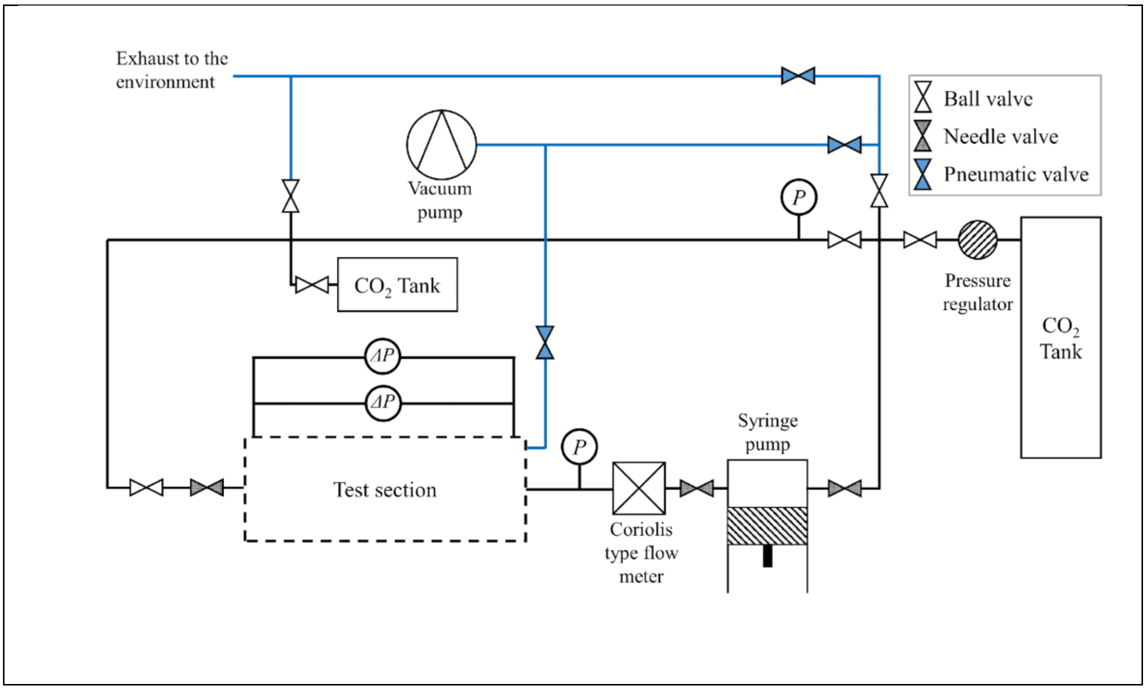


Figure 3.5. Schematic representation of the carbon dioxide test setup

The test section is constructed in a vacuum chamber (1) as shown in Figure 3.6. The vacuum chamber is made of a PVC pipe, 40 cm in diameter and 70 cm in length, and the absolute pressure in the chamber is maintained at less than 1 kPa by the vacuum pump. The vacuum chamber has played an important role in reducing the convection heat loss from the outer surface of the microtube (2) approximately by 50 percent in the present study. The vacuum pump is also used to remove air in the system several times before charging the system with $CO_2$.

The microtube is enclosed by a radiation shield (3) to reduce heat loss by radiation. Two mixing chambers (5) at the inlet and outlet of the microtube are equipped with PT100 sensors (4) to measure the bulk fluid temperature at the inlet and outlet. However, the bulk temperature measurement at the outlet has not been reliable due to the low enthalpy flux of $CO_2$ through the microtube compared to a relatively large mixing chamber. The microtube is heated by a direct current that flows through two brass electrodes (6). Two polyoxymethylene flanges (7) provide electrical insulation for the system.

A voltage across the microtube is measured and thus the total energy input to the tube is calculated from the readings of the voltage and current. Two differential pressure transducers with different ranges are connected to the mixing chambers to measure pressure drop along the tube though the present thesis does not discuss the pressure drop characteristics for $sCO_2$ flows.

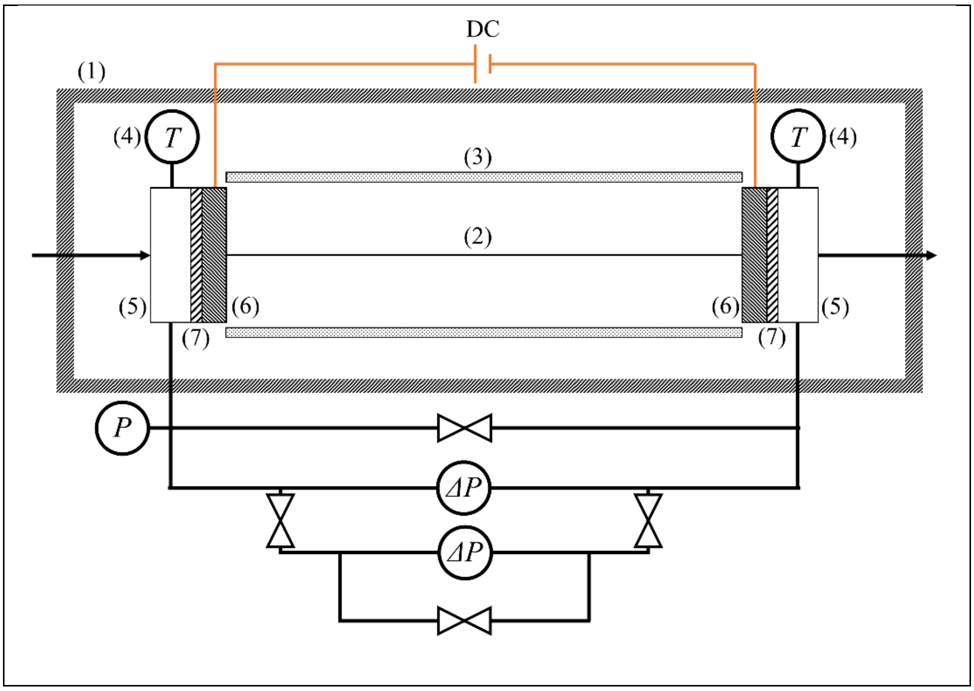


Figure 3.6. Schematic of the test section for carbon dioxide setup

The inner and outer diameters of the microtubes used for $sCO_2$ tests are calibrated as shown in Table 3.1, using two methods described in the water test. The heated and total length of microtubes is also given in Table 3.1. Total 16, 27, and 33 T-type thermocouples are attached to the tube by the proposed method. When placing them, even and odd-numbered thermocouples are attached at the bottom and top of the microtube, respectively. Two or three more thermocouples, depending on the microtube, measure the ambient temperature in the vacuum chamber.

Table 3.1. Inner diameter, outer diameter, heated length, and total length values of the microtubes, and the total number of thermocouples that are attached to the microtubes used for carbon dioxide tests

| **Microtube** | **Inner diameter, $d_i$ [mm]** | **Outer diameter, $d_o$ [mm]** | **Heated length, $L_H$ [mm]** | **Total length, $L_P$ [mm]** | **Total number of thermocouples** |
|---|---|---|---|---|---|
| 1 | 0.317 | 0.505 | 204 | 230 | 16 (Omega® TT-TI-36-SLE) |
| 2 | 0.509 | 0.987 | 301 | 330 | 27 (Omega® TT-TI-36-SLE) |
| 3 | 0.847 | 1.491 | 374 | 403 | 33 (Omega® TT-TI-30-SLE) |

The summary of uncertainties caused by the measured parameters is given in Table 3.2. All thermocouples are calibrated by the same method as explained in the water test section, and the uncertainty of temperature measurement for different microtubes is given in Table 3.2 within a 95 percent confidence level, which includes all uncertainties from the data acquisition (DAQ) system, DAQ cards, thermocouples themselves and curve fits. Note that the uncertainty of the mass flow rate increases up to 0.8 percent (which corresponds to $Re_{in} \approx 500$ for $d_i = 0.317$ mm) whereas it drops to 0.2 percent when $Re_{in} \approx 8000$ for $d_i = 0.847$ mm. These are the minimum and maximum of the test ranges that the experimental setup is capable of. The final uncertainties in the Nusselt number were found to be between 7.2 and 22.8 percent by error propagation of all measured parameters with a 95 percent confidence level. The biggest contribution to the resulting uncertainty was made by temperature measurement, and the highest uncertainties arise when the difference between the wall and mean temperature is very small.

Table 3.2. The uncertainty of each measured parameter for microtubes used for carbon dioxide tests

| Measured parameters | Uncertainty of each variable | | |
|---|---|---|---|
| | **$d_i$ = 0.317 mm** | **$d_i$ = 0.509 mm** | **$d_i$ = 0.847 mm** |
| Inner diameter | ±0.73% | ±0.31% | ±0.18% |
| Current | ±0.2% | | |
| Electrical resistivity | ±0.12% | ±0.80% | ±0.05% |
| Heat loss coefficient, $h_{loss}$ | ±1.5% | ±3.2% | ±2.5% |
| Temperature | ±0.10 °C | ±0.20°C | ±0.15°C |
| Pressure | ±0.25% over the full range of 10 MPa | | |
| Mass flow rate | ±0.20-0.80% | | |

## 3.4. DATA REDUCTION

Heat loss from the outer surface of the tube becomes substantial as the Reynolds number decreases and the tube size becomes smaller. In order to show this, Equation (3.2) was written which examines the ratio of heat loss at the tube surface to the enthalpy increase of fluid over the infinitesimal tube length $\Delta x$. Noting that $Re = 4\dot{m}/(\pi d_i \mu)$ and $Pr = c_p\mu/k$,

$$\frac{heat\ loss}{enthalpy\ increase} = \frac{h_\infty(\pi d_o \Delta x)(T_w - T_\infty)}{\dot{m}c_p \dfrac{dT_m}{dx}\Delta x} = \frac{4h_\infty(T_w - T_\infty)}{Re\ Pr\ k\ \dfrac{dT_m}{dx}}\frac{d_o}{d_i} \tag{3.2}$$

where $d_o$ and $d_i$ denote the outer and inner diameters, respectively, $h_\infty$ denotes the combined heat loss coefficient due to free convection and radiation, and $k$ is the thermal conductivity of the fluid. $T_w$, $T_\infty$ , and $T_m$ are the tube wall temperature, the surrounding air temperature, and the mean fluid temperature, respectively. Equation (3.2) shows that heat loss becomes more significant as the Reynolds number decreases. Moreover, the ratio of $d_o$ to $d_i$ tends to be larger for microtubes than for tubes with large diameters. For example, for a stainless steel tube, 6 mm in outer diameter, with the wall thickness of 1 mm, the ratio of $d_o$ to $d_i$ is 1.5 while the microtube used in the present study has the ratio of 2. Therefore, the microtube tends to have relatively higher heat loss at the surface at the same operating condition. On the other hand, the Morgan correlation for free convection on an isothermal cylinder has the form [45].

$$\overline{Nu}_d = \bar{h}_\infty d/k = C\,\mathrm{Ra}^n \propto d^{3n} \tag{3.3}$$

Thus, the free convection heat transfer coefficient ($h_\infty$) is proportional to $d^{3n-1}$. The value of $n$ becomes smaller for the lower Rayleigh number that is the case for a microtube according to the Morgan correlation. The typical value of the Rayleigh number in the present study is much less than 10 and thus the corresponding $n$ value is 0.148 in the Morgan correlation [45]. (The experiments of $CO_2$ that will be discussed later are conducted in a vacuum chamber and thus the Rayleigh number is less than $10^{-3}$ with the corresponding $n$ value of 0.058. Note that the maximum $n$ value even for very large Rayleigh numbers is 0.333 for the Morgan correlation [45]. Therefore, the power of ($3n$-1) is always less than zero.) Consequently, as the tube diameter becomes smaller, $h_\infty$ in Equation (3.2) becomes larger. Therefore, heat loss from the tube surface may not be neglected for flow in a microtube at a low Reynolds number.

Careful treatment of heat loss from the surface of a microtube is of great importance for two reasons. First, most of the studies in the literature assume that the heat loss from the tube surface is negligible. This may be a good assumption for turbulent flow through a tube with a large diameter that has high enthalpy flux compared to heat loss. However, the heat loss is no longer negligible for a microtube flow at low Reynolds numbers, and the heat loss must be included in the data reduction process to reduce uncertainty in heat transfer results. The second reason is that, for $CO_2$ flow at low Reynolds numbers through a microtube, it is almost impossible to measure the mean fluid temperature at the tube outlet with high accuracy. Thus, the present study of supercritical $CO_2$ flows calculates the net heat flux to flow from the total heat generation and the heat loss from the surface and integrates the enthalpy increase due to the net heat flux. One of the purposes of the validation test with water flow, therefore, is to compare the mean temperature obtained by integrating the enthalpy increase with the mean temperature measured at the tube outlet.

The present study determines heat loss coefficients by another test with no water flow. The microtube with the solder casts is heated by electric current to achieve surface temperatures at different levels, and all the heat generation is assumed to be lost to the surroundings by free convection and radiation. The combined heat loss coefficient for free convection and radiation at each thermocouple location for each surface temperature is calculated by dividing the flux of local heat loss by the temperature difference between the tube wall and the ambiance. Thus, the heat loss coefficient, $h_{loss}$, is obtained as a function of the temperature difference between the surface and the surroundings.

Though the present study intends to have constant heat flux boundary conditions by providing constant electric current, constant heat flux is not achieved in a strict sense for two reasons. One reason is that heat loss from the surface of the tube wall depends on the wall temperature and thus more heat is lost toward the tube outlet. The second reason is that the electrical resistance of the tube depends on the temperature of the wall and the electrical resistance between the inlet and outlet of the microtube may change by up to 3 percent in the present study. Therefore, the present study employs temperature-dependent electrical resistivity along the tube to determine the heat generation in the tube.

The net heat flux to fluid flow is calculated by considering the local heat generation, heat loss from the outer surface of the tube, and axial conduction over an infinitesimal element, $\Delta x$, of a tube as shown in Figure 3.7. The energy balance equation over the infinitesimal control volume can be written as follows.

$$\begin{aligned}\dot{q}A_c\Delta x - q''_{net}\pi d_i\Delta x - q''_{loss}\pi d_o\Delta x + \left(-kA_c\frac{dT}{dx}\right) \\ - \left[-kA_c\frac{dT}{dx} + \frac{d}{dx}\left(-kA_c\frac{dT}{dx}\right)\Delta x\right] = 0\end{aligned} \tag{3.4}$$

where $A_c$ is the cross-sectional area of the tube wall. Though the wall temperature changes in both axial and radial directions, the difference between the inner and outer wall temperatures is usually very small. Therefore, the axial conduction term in Equation (3.4) is analyzed as one-dimensional by approximating $T$ as the average of the inner and outer wall temperatures. The heat generation per unit volume, $\dot{q}$, can be expressed with an infinitesimal electrical resistance, $\Delta R$, over $\Delta x$ as

$$\dot{q} = \frac{I^2\Delta R}{A_c\Delta x} = \frac{I^2}{A_c\Delta x}\frac{\rho\Delta x}{A_c} = \frac{\rho I^2}{A_c^2} \tag{3.5}$$

where $\rho$ is the electrical resistivity of the tube as a function of temperature. Then, an expression for the net heat flux from Equations (3.4) and (3.5) can be written as

$$q''_{net} = \frac{1}{\pi d_i}\frac{\rho I^2}{A_c} - q''_{loss}\frac{d_o}{d_i} + \frac{1}{\pi d_i}kA_c\frac{d^2T}{dx^2} \tag{3.6}$$

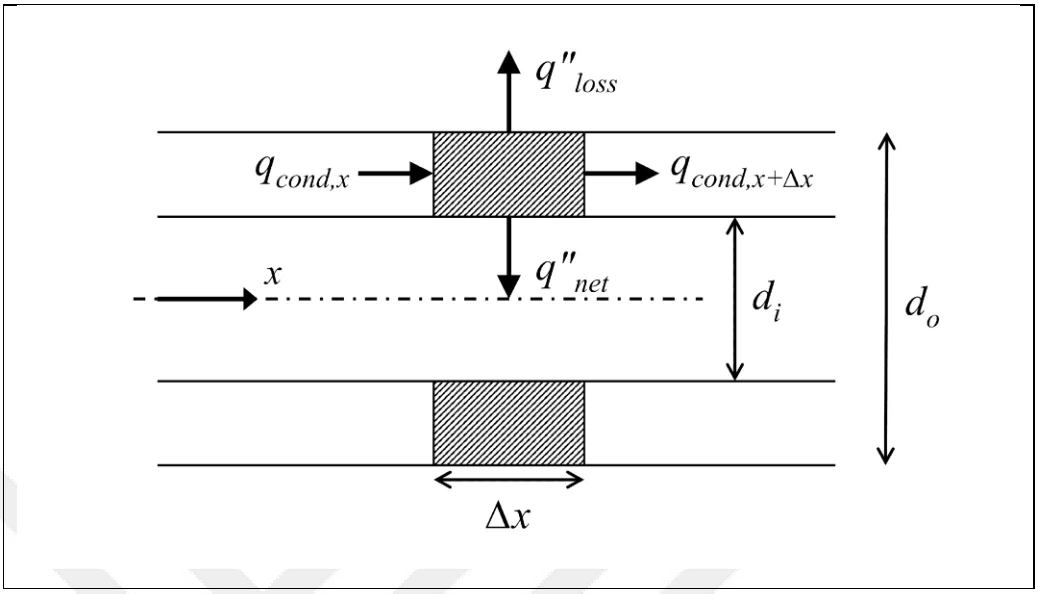


Figure 3.7. Energy balance over an infinitesimal control volume to obtain the net heat flux to flow

The bulk fluid enthalpy through the microtube is obtained by integrating the net heat flux from Equation (3.6) over each interval between two thermocouple locations ($k$ and $k$+1) as shown in Equation (3.7).

$$h_{k+1} = h_k + \frac{\pi d_i}{\dot{m}} \int_k^{k+1} q''_{net} dx \tag{3.7}$$

where $h$ is the bulk fluid enthalpy and $\dot{m}$ is the mass flow rate. The mean fluid temperature is obtained from the bulk enthalpy using NIST REFPROP [46] software. Wang et al. [40] also calculated the local bulk enthalpy in a way similar to Equation (3.7). However, instead of the local net heat flux as used in the present study, they used the average heat flux which is obtained from the total heat measured by the enthalpy increase between the tube inlet and outlet.

Since thermocouples measure the outer wall temperatures, the inner wall temperatures can be obtained by Equation (3.8) which is derived from the one-dimensional heat conduction equation with the outer surface insulated. The heat loss coefficient from the outer surface is much smaller than the convection heat transfer coefficient at the inner surface, and thus the assumption of the outer surface being insulated may provide sufficient accuracy to calculate the temperature difference between the inner and outer walls.

$$T_{wi} = T_{wo} - \frac{\dot{q}r_o^2}{4k}\left[2ln\,\frac{r_o}{r_i} - 1 + \left(\frac{r_i}{r_o}\right)^2\right] \tag{3.8}$$

Local heat transfer coefficient and Nusselt number are calculated as

$$htc_x = \frac{q''_{net}}{(T_{wi} - T_m)} \tag{3.9}$$

$$Nu_x = \frac{htc_x d_i}{k} \tag{3.10}$$

where $k$ is the thermal conductivity of the fluid and is obtained from NIST REFPROP [46] software at the film temperature for the water tests. Note that all the Nusselt numbers are evaluated at the mean temperature in the $sCO_2$ tests unless indicated otherwise. The Graetz number is defined as

$$Gz_{d_i} = RePr\frac{d_i}{x} \tag{3.11}$$

where Prandtl number $Pr$ and viscosity $\mu$ are obtained using NIST REFPROP [46] software at local film temperature as a function of $x$. In the present study, all the data analysis is done by a program written in Fortran linked with NIST REFPROP.

The data analysis method for the water tests described previously is also applied to $sCO_2$ flows. However, it has been unsuccessful to measure the mean fluid temperature at the tube outlet with reasonable accuracy because the enthalpy flux of $CO_2$ through the microtube is low, the thermal mass of the RTD (PT100) is large, and the thick wall of the mixing chamber affects fluid temperature measurements. Therefore, the method of integrating the net heat flux is employed to calculate the mean temperature through the microtube (see Equation (3.7)). Consequently, the accurate calculation of heat loss is very critical in the $CO_2$ tests. Though the tests are conducted in the vacuum chamber, heat loss from the outer surface of the microtube is still found to be as high as 10 to 20 percent of the total energy input at low Reynolds numbers. For turbulent flows, on the other hand, heat loss is determined to be typically 1 to 2 percent.

The dimensionless specific enthalpies at the mean and film temperature are defined as follows.

$$h_m^* = \frac{h_m - h_{in}}{h_{pc} - h_{in}}$$
$$h_f^* = \frac{h_f - h_{in}}{h_{pc} - h_{in}} \tag{3.12}$$

where subscripts *m* and *f* denote the mean and film temperature, respectively. $h_{in}$ is the specific enthalpy at the tube inlet and $h_{pc}$ is the specific enthalpy at the pseudo-critical temperature ($h_{pc}$ = 341.33 kJ/kg at 8.0 MPa for $CO_2$).

The thermophysical properties of $CO_2$ have been obtained from the NIST REFPROP [46] software. It is noted that the properties of supercritical $CO_2$ near the critical point rapidly change as temperature increases along the tube. Since the Reynolds number significantly increases from the inlet to the outlet, it may be more appropriate to describe the data in terms of the mass flux, *G*, as shown in Equation (3.13).

$$G = \frac{\dot{m}}{A_c} = \frac{\dot{m}}{\frac{\pi}{4} d_i^2} \tag{3.13}$$

Because the mass flow rate or mass flux is constant along the tube, the Reynolds number is solely affected by dynamic viscosity as shown in Equation (3.14).

$$Re = \frac{4\dot{m}}{\pi d_i \mu} = \frac{G d_i}{\mu} \tag{3.14}$$

The heat flux can be expressed as follows.

$$q" = \frac{Q}{A_s} = \frac{\dot{m}\Delta h}{\pi d_i x} = \frac{G \frac{\pi}{4} d_i^2 \Delta h}{\pi d_i x} = G\Delta h \frac{d_i}{4x} \tag{3.15}$$

where *Q* is the net heat transfer to the flow, $A_s$ is the inner surface area, and $\Delta h$ is the enthalpy increase over *x*, the distance from the tube inlet. Accordingly, the ratio of heat flux to the mass flux over the heated length of the tube can be written as follows. A constant *q"/G* ratio ensures that the enthalpy increase is the same for the equivalent microtubes.

$$\frac{q"}{G} = \Delta h \frac{d_i}{4L} \tag{3.16}$$

### 3.4.1. More Detailed Analysis on the Effect of the Solder Cast

The solder cast in which a thermocouple is embedded is employed to reduce the thermal contact resistance between the thermocouple and the outer surface of a microtube. But a disadvantage of using the solder cast is that the solder cast leads to a larger surface area from which heat loss occurs. The solder cast acts like a fin with an extended surface over the tube wall. Consequently, the wall temperature under the solder cast is lower than that of its neighboring walls. On the other hand, the lower temperature under the solder cast would prompt axial conduction heat transfer from the neighboring walls to the wall under the solder cast. In this section, therefore, a detailed analysis is presented to examine the effect of the solder cast on heat loss augmentation and axial conduction along the tube wall.

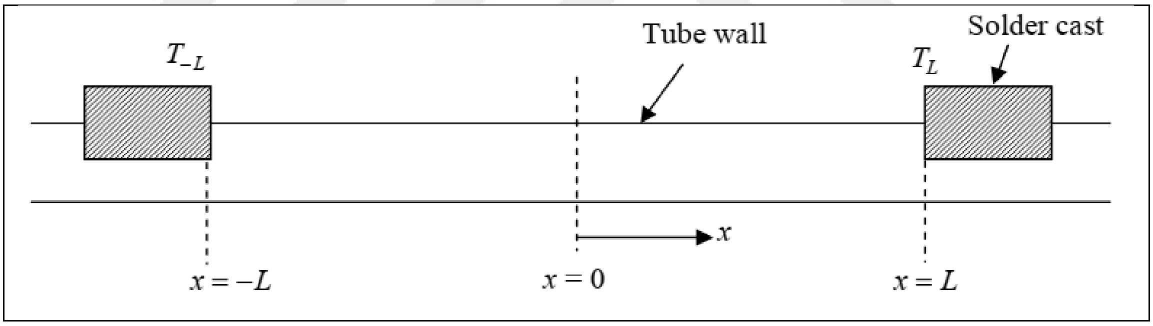


Figure 3.8. A model to analyze the effect of the solder casts on heat loss and axial conduction

Figure 3.8 shows a model of two successive solder casts on a microtube. The thermocouples measure the temperatures of the solder casts. The temperature distribution inside each solder cast is assumed to be uniform due to the high thermal conductivity of the solder and its small size, and the outer wall temperature of the tube underneath the solder cast is also assumed to be uniform. Furthermore, the radial temperature distribution of the tube wall under the solder cast is assumed to be axisymmetric due to the relatively thick wall. Then the outer wall temperature, $T_{wo}$, is obtained from the solder cast temperature, $T_s$, as follows.

$$T_{wo} = T_s + \frac{h_\infty}{k_{tp}} \frac{A_s}{A_e} (T_s - T_\infty) \Delta x_{tp} \tag{3.17}$$

where $k_{tp}$ and $\Delta x_{tp}$ are the thermal conductivity and thickness of the thermal paste between the solder cast and the tube. Note that the thermocouples measure $T_s$. The surface area of the solder cast, and the contact area between the cast and the tube are denoted by $A_s$ and $A_e$, respectively. In the present study, the temperature difference between the solder cast and the outer wall temperature is found to be 0.02 to 0.1°C, depending on heat fluxes applied, with the values of $k_{tp}$ = 8.5 W/m·K and $\Delta x$ = 0.1 mm. A simple analysis shows that free convection heat transfer coefficients on the vertical and horizontal surfaces of the solder cast are almost the same value as that on the microtube. Thus, the heat loss coefficient determined from the heat loss test on the tube is also used for $h_\infty$.

The temperature difference between the inner and outer walls is considerably small compared to the difference between the inner wall and the internal flow, and the difference between the outer wall and air. Therefore, the wall temperature of the tube from $x = -L$ to $x = L$ is only a function of $x$, ignoring the temperature difference between the inner and outer walls. Considering heat loss from the tube surface, convection to the flow, and heat generation, then, the conduction equation can be written at a point between $-L$ and $L$ as follows.

$$kA_c \frac{d^2T}{dx^2} - P_o h_\infty (T - T_\infty) - P_i h_i (T - T_m) + \dot{q} A_c = 0 \tag{3.18}$$

where $T$ is the wall temperature as a function of $x$. Perimeters $P_o$ and $P_i$ are given as $\pi d_o$ and $\pi d_i$, respectively. The mean fluid temperature $T_m$ is assumed to increase linearly from $x = -L$ to $x = L$. Now the convection heat transfer coefficient $h_i$ is assumed to be constant at $h_{i-}$ from $x = -L$ to 0 and constant at $h_{i+}$ from $x = 0$ to $L$. Then the general solution to Equation (3.18) is given in the Equations (3.19) and (3.20).

$$T = \frac{1}{m_-^2} \left( \frac{\dot{q}}{k} + m_o^2 T_\infty + m_{i-}^2 T_m \right) + C_1 e^{m_- x} + C_2 e^{-m_- x} \text{ for } -L < x < 0 \tag{3.19}$$

$$T = \frac{1}{m_+^2} \left( \frac{\dot{q}}{k} + m_o^2 T_\infty + m_{i+}^2 T_m \right) + C_3 e^{m_+ x} + C_4 e^{-m_+ x} \text{ for } 0 < x < L \tag{3.20}$$

where

$$m_o^2 = \frac{h_\infty P_o}{kA_c},\ m_{i-}^2 = \frac{h_{i-}P_i}{kA_c},\ m_{i+}^2 = \frac{h_{i+}P_i}{kA_c},\ m_-^2 = m_o^2 + m_{i-}^2 \text{ and } m_+^2 = m_o^2 + m_{i+}^2 \tag{3.21}$$

Four constants, $C_1$, $C_2$, $C_3$, and $C_4$, are determined by four boundary conditions.

$$T(-L) = T_{-L},\ T(L) = T_L,\ T(0^+) = T(0^-) \text{ and } \frac{dT}{dx}(0^+) = \frac{dT}{dx}(0^-) \tag{3.22}$$

where $T_{-L}$ and $T_L$ are solder cast temperatures at $x = -L$ and $x = L$, respectively. Therefore, axial heat conduction at $x = -L$ and $x = L$ are obtained as follows.

$$\begin{aligned} q_{-L} &= -kA_c \frac{dT}{dx}\bigg|_{x=-L} \\ &= -kA_c\left[\frac{m_{i-}^2}{m_-^2}\frac{T_m(L) - T_m(-L)}{2L} + m_-C_1e^{-m_-L} - m_-C_2e^{m_-L}\right] \end{aligned} \tag{3.23}$$

$$\begin{aligned} q_L &= -kA_c \frac{dT}{dx}\bigg|_{x=L} \\ &= -kA_c\left[\frac{m_{i+}^2}{m_+^2}\frac{T_m(L) - T_m(-L)}{2L} + m_+C_3e^{m_+L} - m_+C_4e^{-m_+L}\right] \end{aligned} \tag{3.24}$$

Thus, the net heat flux to fluid flow at the position of a solder cast is calculated from the total heat generation underneath the solder cast, the net axial heat conduction to both sides of the solder cast, and the heat loss from the entire surface of the solder cast. Then the convection heat transfer coefficients, $h_{i-}$ and $h_{i+}$, for all the solder casts are found by iteration using the multivariable Newton's method with the Jacobian matrix.

The mathematical method presented in this section may be regarded as a first-order correction on the conduction calculated by Equation (3.6) which does not consider the effect of the solder casts. The following section will present results using two methods, namely, one method without considering the effect of the solder cast as described in Section 3.4 and the other method with the effect of the cast as described in this section.

# 4. RESULTS AND DISCUSSION

## 4.1. VALIDATION OF THE NEW METHOD BY LAMINAR WATER FLOW TESTS

Table 4.1 lists four water tests with different Reynolds numbers at the inlet and different heat fluxes. The Reynolds number at the outlet is considerably higher than that at the inlet, as shown in Table 4.1, implying a significant change in fluid properties. Furthermore, the ratio of $Re_{out}$ to $Re_{in}$ is shown to increase as the ratio, $q''_{net} / Re_{in}$, increases. It is noted that the analytical value of $Nu$ = 4.36 for laminar flow with the constant heat flux boundary condition is obtained with the assumption of constant properties. Meyer and Everts [3] discuss that considerable fluid property change, as a result of increasing heat flux, causes the secondary flow due to buoyancy force which would increase Nusselt numbers. Bergles and Simonds [47] state that the assumption of constant fluid property for laminar heat transfer is not valid in actual practice. Therefore, Nusselt numbers in the present tests are expected to be larger than 4.36.

The amount of the total heat loss is analyzed in two ways as shown in Table 4.1. One way is to calculate heat loss flux at each thermocouple location using heat loss coefficients from the heat loss test, determine the net heat flux to fluid, and thus find the mean temperature by integrating the net heat flux using Equation (3.7). The other way is to measure the bulk temperature at the mixing chamber located at the outlet. The heat loss obtained by measuring the outlet bulk temperature is shown to be consistently higher than that obtained by integrating the net heat flux. This is believed to be due to additional heat loss in the mixing chamber and conduction heat loss through the DC cable at the end of the tube as shown in Figure 3.4. The two ways of calculating the heat loss are generally in good agreement while a large discrepancy is found at a low Reynolds number such as in Test #1. As shown in Table 4.1 and as expected from Equation (3.2), heat loss decreases as the Reynolds number increases. It is noted that the outlet temperature differences calculated by the two ways for Tests #3 and #4 are within the uncertainty of temperature measurement.

Table 4.1. Reynolds number at the inlet, the ratio of Reynolds number at the inlet and outlet, net heat flux, the average difference between the inner wall temperature and mean temperature in the fully developed region, the outlet temperature calculated by the integration method, measured outlet temperature, percentage heat loss calculated by integration, percentage heat loss calculated by measurement, and percentage heat loss difference between two methods for different tests

| **Test #** | **1** | **2** | **3** | **4** |
|---|---|---|---|---|
| $Re_{in}$ | 293 | 536 | 681 | 789 |
| $Re_{out}$ / $Re_{in}$ | 1.58 | 1.72 | 1.12 | 1.40 |
| $q''_{net}$ [kW/m$^2$] | 17.20 | 38.74 | 9.07 | 32.42 |
| $q''_{net}$ / $Re_{in}$ | 0.059 | 0.072 | 0.013 | 0.041 |
| $(T_{wi}-T_m)_{fd,ave}$ [°C] | 2.86 | 6.41 | 1.60 | 5.35 |
| $T_{out}$ obtained by integration [°C] | 41.70 | 46.46 | 25.88 | 36.27 |
| $T_{out}$ measured at the outlet [°C] | 40.53 | 46.09 | 25.77 | 36.06 |
| $T_{out,integration}$ - $T_{out,measured}$ [°C] | 1.17 | 0.37 | 0.11 | 0.21 |
| Heat loss by integration [%] | 7.21 | 5.17 | 4.41 | 4.29 |
| Heat loss by measurement [%] | 12.30 | 6.51 | 6.58 | 5.61 |
| Heat loss difference between two methods [%] | 5.08 | 1.34 | 2.16 | 1.33 |

The cases of Tests #1 and #3 in Table 4.1 are examined in Figure 4.1 where the two methods with and without the effect of the solder cast are compared. A method of using the mean temperature that linearly varies from the inlet temperature to the outlet temperature measured at the mixing chamber is also added to the plot. The Nusselt number that is obtained with the method including the effect of the solder cast (as explained in Section 3.4) is calculated consistently lower than that obtained with the method ignoring the effect of the solder cast. This is expected because the solder cast has higher heat loss at the thermocouple location and thus local net heat flux transferred to fluid is lower than the case without the solder cast. It should be emphasized, however, that the discrepancies of Nusselt numbers between the two methods are found to be as small as 4.8 and 2.3 percent for Tests #1 and #3, respectively, at the location of $x/d$ = 350. Nusselt number obtained with the method including the effect of the solder cast lies in a narrow band between 4.36 and 4.36 + 10 percent in the fully developed region. Note that this new method calculates the mean temperature by integrating the net heat flux without knowing the outlet temperature. On the other hand, when the mean temperature is calculated as a linear function of $x$, using the outlet temperature measured at the mixing chamber, the Nusselt numbers for both cases become less than 4.36. This result is believed to be associated with the difficulty of measuring the outlet temperature at the mixing chamber due to low enthalpy flux through the microtube.

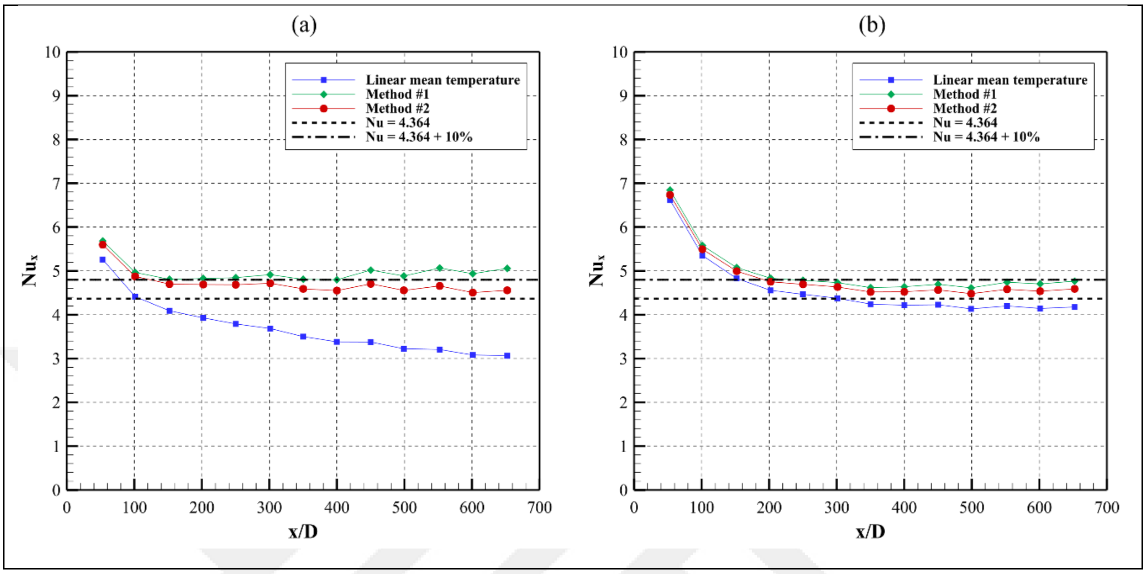


Figure 4.1. Variation of local Nusselt number calculated at the film temperature vs. *x/d*. Three methods are compared: mean temperature linearly calculated using the mean temperature measured at the outlet, method #1 that calculates the mean temperature by integrating the net heat flow without considering the effect of the solder cast, and method #2 that considers the effect of the solder cast as explained in Section 3.4. (a), $Re_{in}$ = 293, the case of Test #1 in Table 4.1; (b), $Re_{in}$ = 681, the case of Test #3 in Table 4.1.

All four cases in Table 4.1 are examined in Figure 4.2 where local Nusselt numbers are plotted as a function of the inverse Graetz number. The lines of $Nu$ = 4.36, $Nu$ = 4.36 + 10 percent, and the correlation by Shah and Bhatti [48] are also included in the figure. All four cases start entering the fully developed region approximately at $Gz^{-1}$ = 0.05. For the fully developed region, all local Nusselt numbers that are calculated including the effect of the solder casts fall within 4.36 and 4.36 + 10 percent. Note that differences between the inner wall and mean fluid temperatures for the four tests range from 1.6°C to 6.4°C as shown in Table 4.1. This proves that the Nusselt number can be obtained with reasonable accuracy even in the case of a temperature difference as small as 1.6°C. Therefore, these results validate the new method using the solder cast to measure the wall temperature.

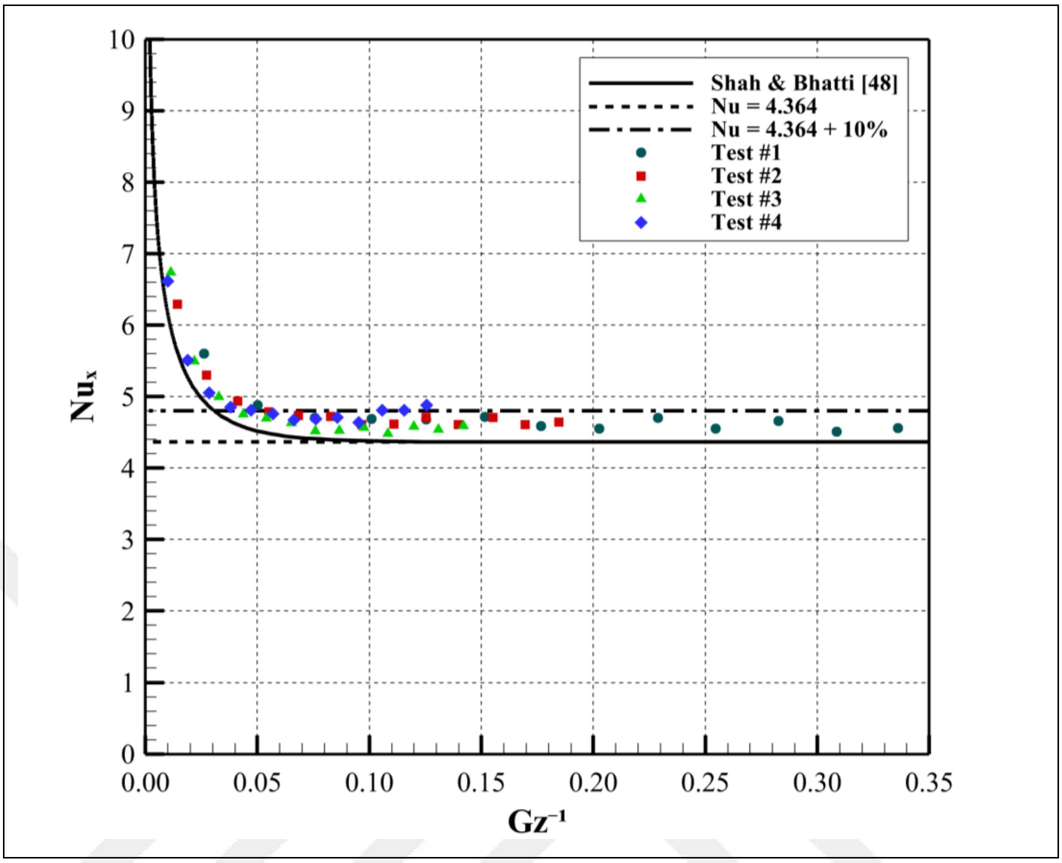


Figure 4.2. Variation of local Nusselt number calculated at the film temperature as a function of inverse Graetz number for four cases described in Table 4.1

### 4.1.1. A Discussion on Uncertainties in the Water Tests

Various uncertainties of measured variables that affect the calculation of the Nusselt number are listed in Table 4.2. The magnitudes of these uncertainties are found to be comparable to those that are found in the literature. Following the procedure by Figliola and Beasley [49], the uncertainties in *Nu* (at the location of $x/L$ = 0.5) propagated from the uncertainty of each variable are calculated by the Fortran program and shown for each test in Table 4.2. Then, the uncertainty of *Nu* propagated from the uncertainties of all measured variables is calculated by taking the square root of the sum of the squares (RSS) of the uncertainties from all the variables, and is shown in the last row of Table 4.2 for each test case. It is apparent from Table 4.2 that the uncertainty of temperature measurement is the largest contributor to the uncertainty in *Nu*. For example, the difference between the mean and wall temperatures for Test #3 is 1.6°C as shown in Table 4.1. The uncertainty in measuring the temperature of the solder cast is propagated to be the uncertainty of 21.1 percent in *Nu*. When it is combined with the error propagations from other variables, the total uncertainty in *Nu* is determined to be 21.2 percent, showing that the uncertainty in temperature measurement is the major source of the total uncertainty in *Nu*. It is recalled that the uncertainty of 0.3°C in the temperature measurement includes all uncertainties from the data acquisition (DAQ) system, DAQ cards, thermocouples themselves, and curve fits.

It is noted that the present study calculates the heat power from the local heat generation that is obtained by the electric current, the electrical resistivity of the tube, the wall temperature, and the tube diameters as shown in Equation (3.5). The uncertainty of the total heat power, when separately calculated from these measurements, is determined to be approximately 0.9 percent for all the water tests. On the other hand, the net heat flux is calculated by the current, mass flow rate, wall temperature, electrical resistivity, heat loss, and diameter. All these measurements are included in Table 4.2 to calculate the uncertainty of the Nusselt number.

Many kinds of research on convection heat transfer in the literature provide information on the uncertainties of various measurements such as the uncertainty in thermocouples and their calibration. And yet, if the thermocouples are not properly placed on the tube wall with a large thermal contact resistance and thus the wall temperatures are not properly measured, the declaration of the uncertainty of the thermocouples becomes meaningless. Therefore, in addition to the methodology of other uncertainty analyses in the literature, the main focus of the present study on the overall uncertainty in Nusselt number or heat transfer coefficient has been how the wall temperature can be measured with the set of thermocouples with reasonable accuracy. It is noted in the present study that the thermocouples measure the solder cast temperature which must be slightly different from the outer wall temperature by 0.02 to 0.1°C in the present analysis. The outer wall temperature is also slightly different from the inner wall temperature. The solder casts cause uneven temperature gradients along the wall due to their role as the extended surfaces, and thus heat conduction along the tube wall may not be neglected in calculating the net local heat flux to the fluid flow. Furthermore, due to their complex interconnectivity, it can be extremely difficult to make an analytical estimation of the uncertainty in the Nusselt number coming from the usage of the solder casts. However, as discussed in Figure 4.2, the water tests have successfully validated the method of using the solder casts with reasonable accuracy. Therefore, it is concluded that the uncertainty related to using the solder casts must not be substantially large, and that our experimental results can be trusted with reasonable accuracy. But it must be expected that the uncertainty in convection heat transfer tests can be high when the temperature difference between the wall and the fluid is very small as in the case of Test #3 where it is 1.60°C as shown in Table 4.1.

Table 4.2. The propagation of uncertainty in measured variables to Nusselt number in the water tests

| **Measured variables affecting *Nu*** | **Uncertainty of each variable** | **Uncertainty of *Nu* at *x/L* = 0.5 by error propagation from each variable** | | | |
|---|---|---|---|---|---|
| | | **Test #1** | **Test #2** | **Test #3** | **Test #4** |
| Electric current | ±0.2% | 2.1% | 1.3% | 1.1% | 1.0% |
| Heat loss coefficient, $h_{loss}$ | ±3.2% | 0.9% | 0.5% | 0.3% | 0.3% |
| Electrical resistivity | ±0.8% | 4.2% | 2.6% | 2.1% | 2.1% |
| Temperature measurement | ±0.3°C | 10.6% | 4.5% | 21.1% | 5.4% |
| Mass flow rate | ±1% | 3.6% | 2.0% | 1.5% | 1.4% |
| Inner diameter of the tube | ±0.34% | 1.2% | 0.7% | 0.6% | 0.6% |
| Uncertainty in *Nu* propagated from the uncertainties of all measured variables | | **±12.2%** | **±5.8%** | **±21.3%** | **±6.1%** |

## 4.2. SUPERCRITICAL CARBON DIOXIDE TESTS

In supercritical carbon dioxide tests, heat transfer characteristics of three different horizontally configured microtubes shown in Table 3.1 were examined at the inlet Reynolds numbers not exceeding 1100.

### 4.2.1. Heat Transfer Characteristics of Microtube #1 ($d_i$ = 0.317 mm)

Figure 4.3 shows the variation of the Nusselt number, mean fluid temperature, and inner wall temperature as a function of *x/d* where the error bars with a 95 percent confidence level are also shown. The mean fluid temperature and inner wall temperature rise monotonously; in addition, the mean temperature remains almost constant near the pseudo-critical temperature ($T_{pc}$ = 34.7°C) where the specific heat is very high. The difference between the wall and mean temperature becomes minimum at *x/d* = 200, and the Nusselts number peaks at the same point where the film temperature is almost equal to $T_{pc}$.

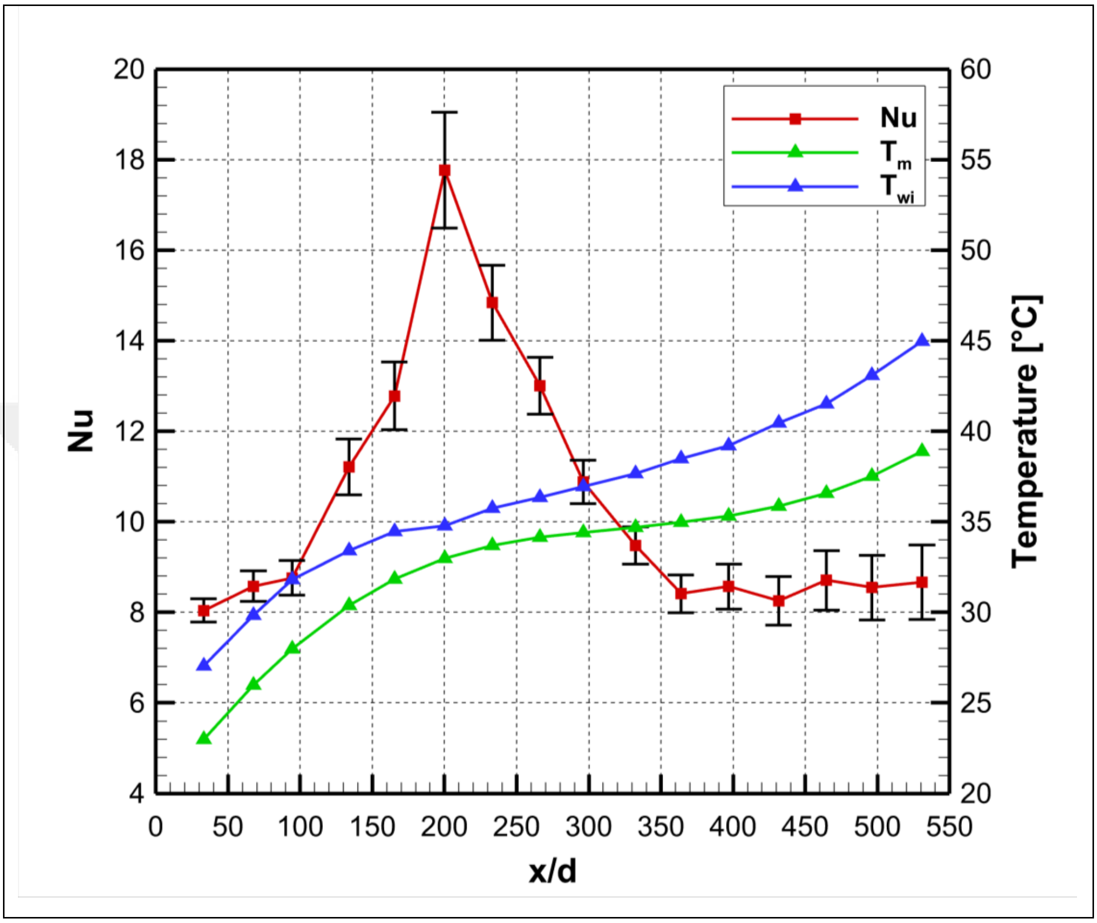


Figure 4.3. The mean fluid temperature, the inner wall temperature, and the Nusselt number as a function of *x/d* for the case of 7.99 MPa, 19.6°C and *Re* = 495 at the tube inlet with $d_i$ = 0.317 mm, *G* = 119 kg/m$^2$·s and *q"/G* = 0.071 kJ/kg. Error bars are shown on the Nusselt number with a 95 percent confidence level. The uncertainty of the peak of *Nu* is 7.2 percent.

The effect of *q"/G* on heat transfer characteristics for almost constant mass flux values varying between 176 and 179 kg/m$^2$·s was examined in Figure 4.4. The Reynolds numbers at the tube inlet are between 726 and 736 while the *Re* at the outlet is ranging from 1830 to 2780 depending on the applied heat flux. In Figure 4.4 (a), 5 different *q"/G* values were plotted against *x/d*. The Nusselt number reaches a peak at around *x/d* = 330 when *q"/G* = 0.049 kJ/kg whereas it has a maximum at *x/d* = 135 if *q"/G* increases to 0.097 kJ/kg. Thus, the location of the peak of the *Nu* moves toward the tube inlet when the $q''/G$ increases, since the mean fluid temperature reaches the pseudo-critical temperature more rapidly.

In Figures 4.4 (b) and (c), the Nusselt number was plotted as a function of dimensionless specific enthalpies at both mean and film temperature (see Equation (3.12)). The peaks of Nusselt numbers given in Figure 4.4 (c) are located at almost the same $h_f^*$ value where it is slightly less than 1. If *Nu* is plotted against $h_m^*$, the peaks appear when $h_m^*$ is in between 0.5 and 0.7. This suggests that the fluid reaches the pseudo-critical temperature near the wall rather than at the core.

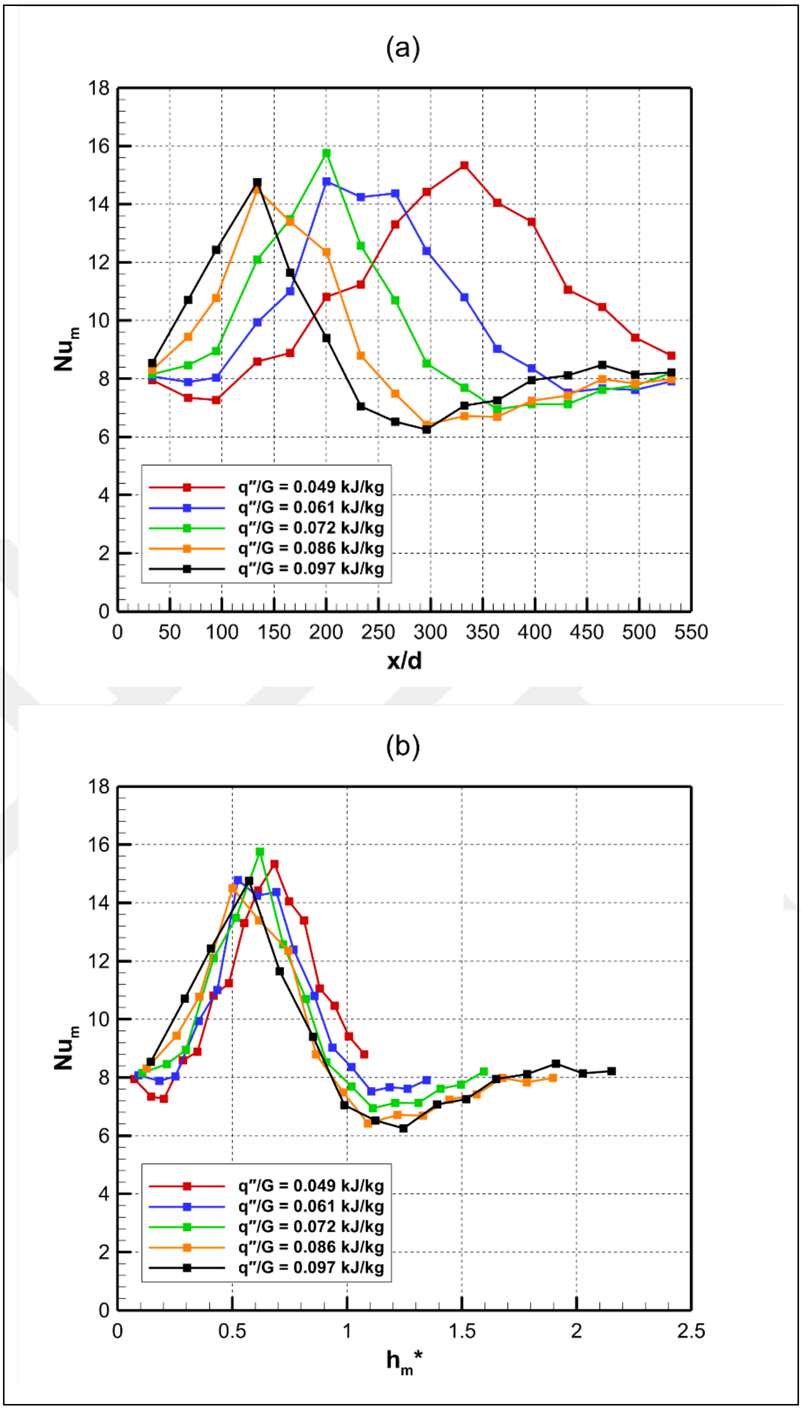
(a)
18
16
14
12
10
8
6
4
2
0
Nu_m
q"/G = 0.049 kJ/kg
q"/G = 0.061 kJ/kg
q"/G = 0.072 kJ/kg
q"/G = 0.086 kJ/kg
q"/G = 0.097 kJ/kg
0
50
100
150
200
250
300
350
400
450
500
550
x/d
(b)
18
16
14
12
10
8
6
4
2
0
Nu_m
q"/G = 0.049 kJ/kg
q"/G = 0.061 kJ/kg
q"/G = 0.072 kJ/kg
q"/G = 0.086 kJ/kg
q"/G = 0.097 kJ/kg
0
0.5
1
1.5
2
2.5
h_m*

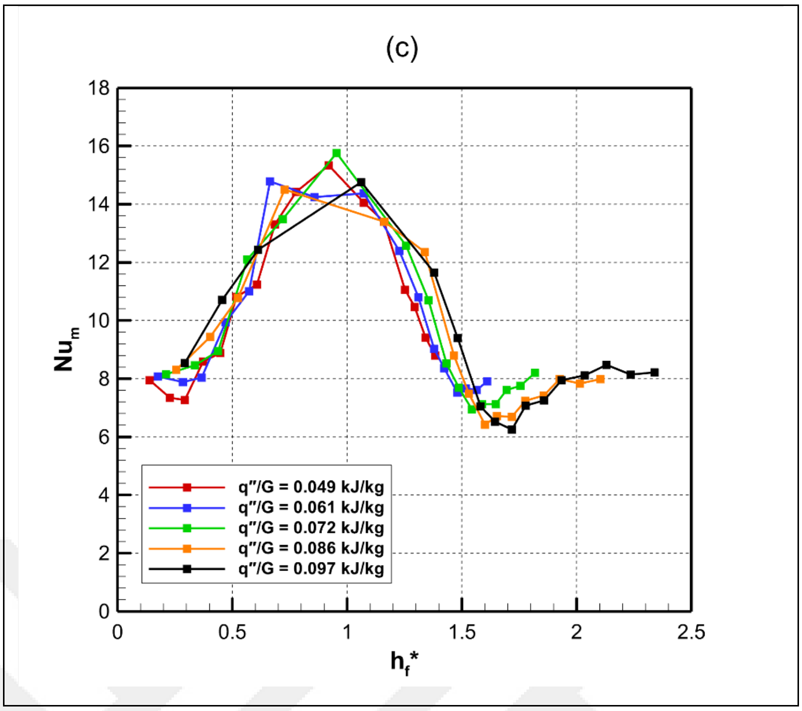


Figure 4.4. Nusselt number as a function of (a) $x/d$, (b) $h_m^*$ and (c) $h_f^*$ for cases of $q''/G$ = 0.049, 0.061, 0.072, 0.086 and 0.097 kJ/kg with $G$ = 176 – 179 kg/m$^2$·s at 8.00-8.02 MPa, 19.2 – 19.3°C and $Re$ = 726 – 736 at the tube inlet.

The effect of mass flux on heat transfer characteristics for a given $q''/G$ ranging from 0.071 to 0.074 kJ/kg is examined in Figure 4.5. The main reason for selecting an almost the same $q''/G$ is that the enthalpy increase from the inlet to the outlet is nearly the same when $q''/G$ is kept constant for different mass fluxes as shown in Equation (3.16). Besides, this ensures that the property change through the tube becomes almost the same if the mean fluid temperatures are close to each other at the tube inlet. Firstly, it is observed that the location where $Nu$ reaches maximum gets closer to the tube inlet when the mass flux increases in Figure 4.5 (a). For a constant $q''/G$, high mass flux results in high heat flux. Although the variation of the mean temperatures along the tube is almost identical for these cases (almost the same $\Delta h$, see Equation (3.16)), the radial temperature profiles are different among these cases depending on the heat flux. The higher heat flux results in a higher temperature gradient near the wall, and thus higher mass flux (higher heat flux for a constant $q''/G$) causes the mean fluid temperature near the wall reaches $T_{pc}$ at a location closer to the inlet.

Secondly, there are some differences between the characteristics of $Nu$ evaluated at the mean and film temperature. The variation of $Nu$ at the film temperature may be erratic in some cases since the thermal conductivity is a strong function of temperature. The thermal conductivity decreases as the temperature increases except for a little peak near the pseudo-critical temperature as shown in Figure 1.1. Thus, the sudden drops in $Nu_f$ observed at $G$ = 119 and 303 kg/m$^2$·s are caused by the variation in thermal conductivity as shown in Figure 4.5 (b). In contrast, the Nusselt number at the mean temperature and heat transfer coefficient show similar behavior, and therefore, it may be more appropriate to present heat transfer characteristics in terms of $Nu_m$ and/or *htc*.

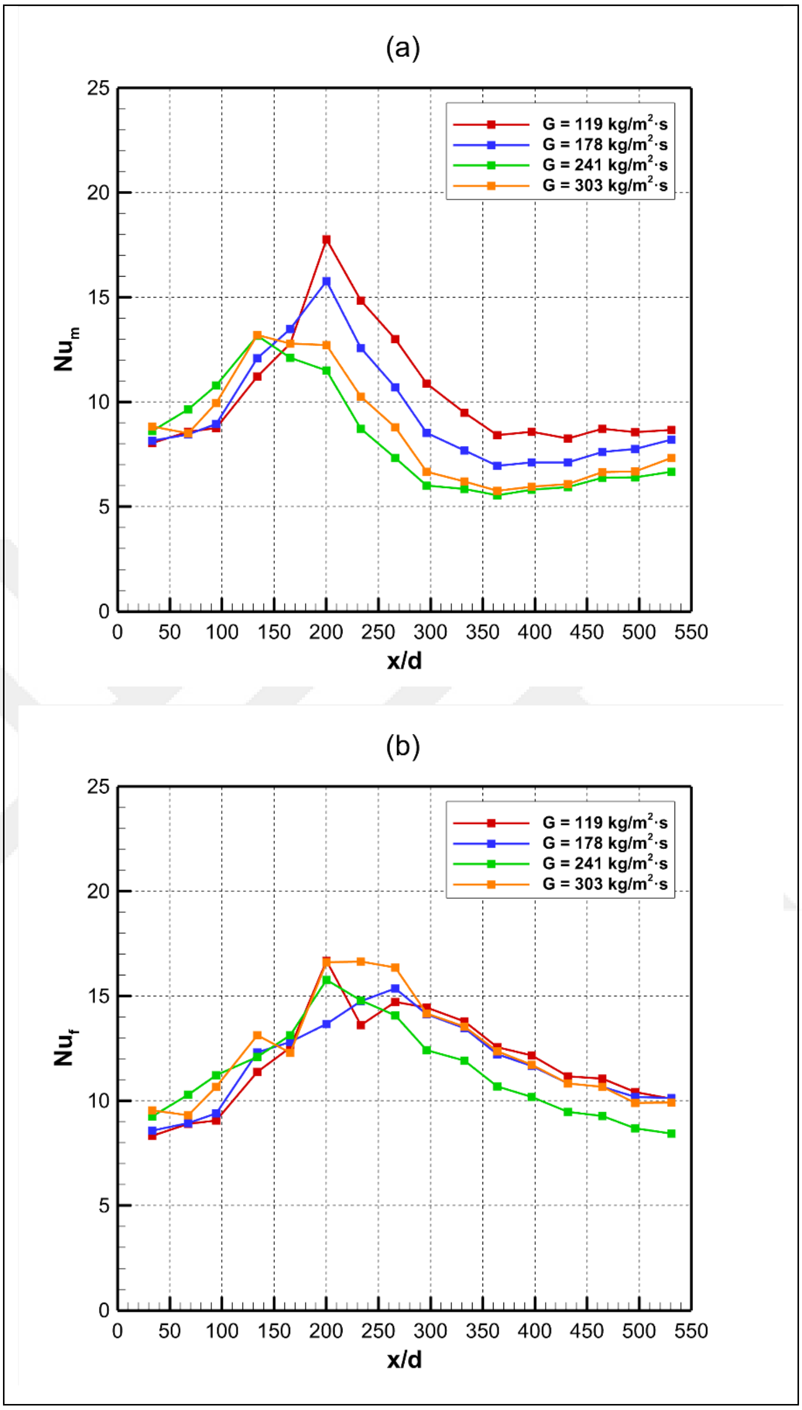
(a)
Nu_m
x/d
G = 119 kg/m²·s
G = 178 kg/m²·s
G = 241 kg/m²·s
G = 303 kg/m²·s
(b)
Nu_f
x/d
G = 119 kg/m²·s
G = 178 kg/m²·s
G = 241 kg/m²·s
G = 303 kg/m²·s

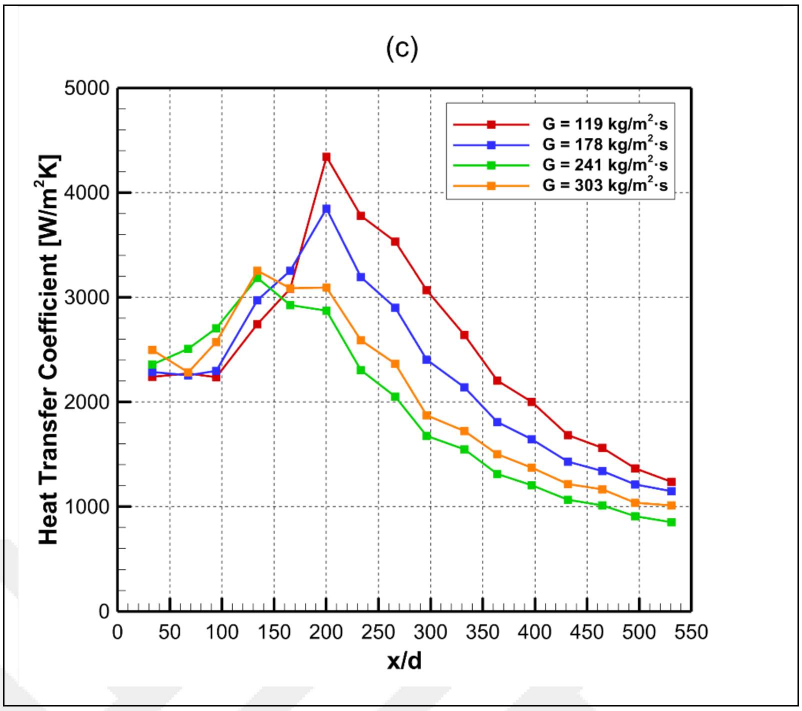


Figure 4.5. The Nusselt numbers (a) at the mean temperature and (b) at the film temperature, and (c) the heat transfer coefficient as a function of *x/d* for cases of $G$ = 119, 178, 241, and 303 kg/m$^2$·s with $q''/G$ = 0.071 – 0.074 kJ/kg at 7.99 - 8.00 MPa and 18.6 – 20.9°C at the tube inlet.

Apart from examining the effect of mass flux for a constant $q''/G$, heat transfer characteristics were also examined for an almost constant heat flux value in Figure 4.6. The heat flux is set to an almost fixed value of $q''$ = 17.2 – 18.3 kW/m$^2$ and different mass flux values of 176, 241, and 297 kg/m$^2$·s were examined. A test with a lower $G$ such as 120 kg/m$^2$·s could not be included in this figure since the wall temperatures at lower mass fluxes may be high enough to cause damaging the thermocouples for a given $q''$. Moreover, the location where the Nusselt number has a peak moves toward the outlet as the mass flux increases as shown in Figure 4.6 (a) since the mean fluid temperature exceeds the pseudo-critical temperature at a location closer to the inlet for a lower $G$. When the Nusselt number was plotted against $h_m^*$ in Figure 4.6 (b), the cases with different mass fluxes behave like a single curve. This is because the heat transfer coefficients (Figure 4.6 (c)), and the difference between the wall and mean temperatures are almost the same for different $G$ values.

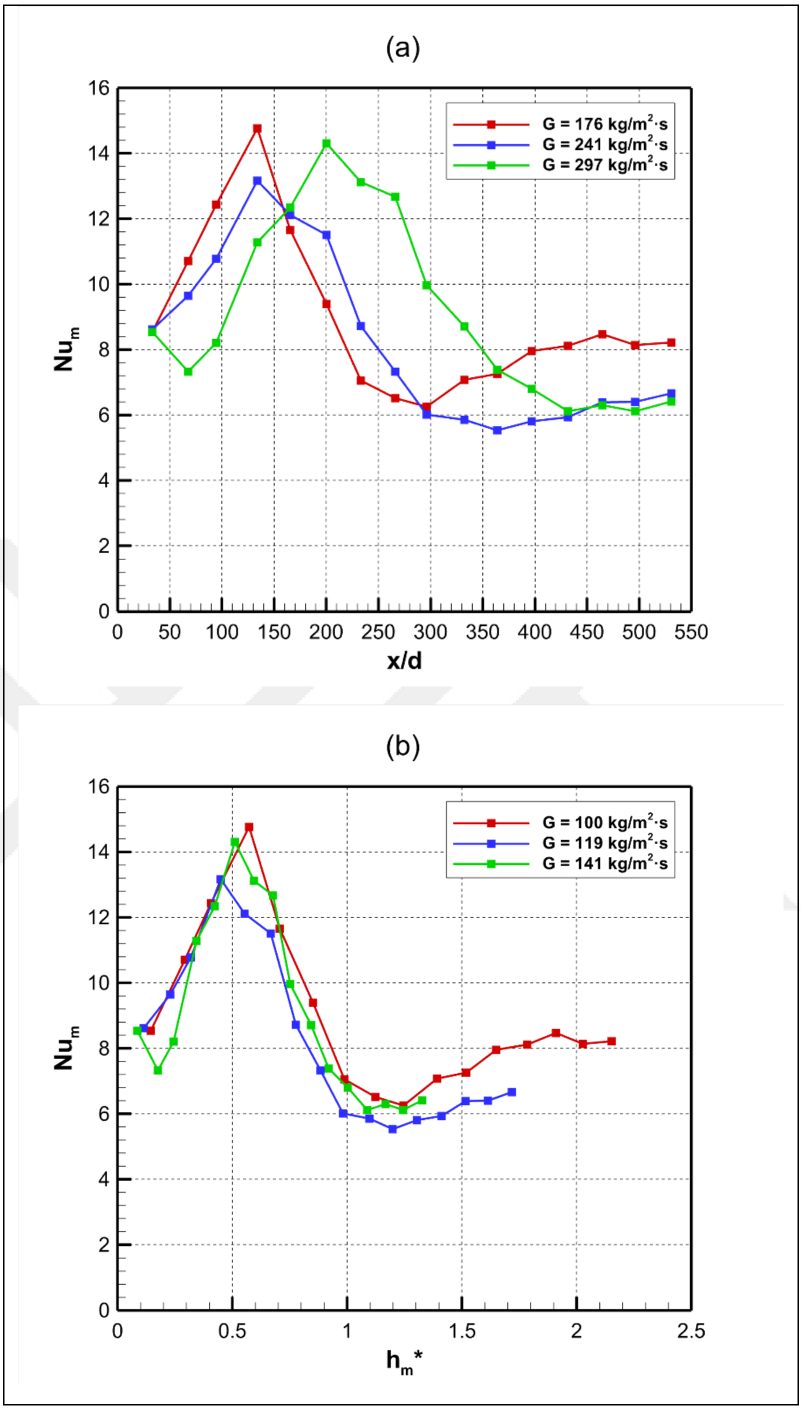
(a)
G = 176 kg/m²·s
G = 241 kg/m²·s
G = 297 kg/m²·s
Nu_m
x/d
(b)
G = 100 kg/m²·s
G = 119 kg/m²·s
G = 141 kg/m²·s
Nu_m
h_m*

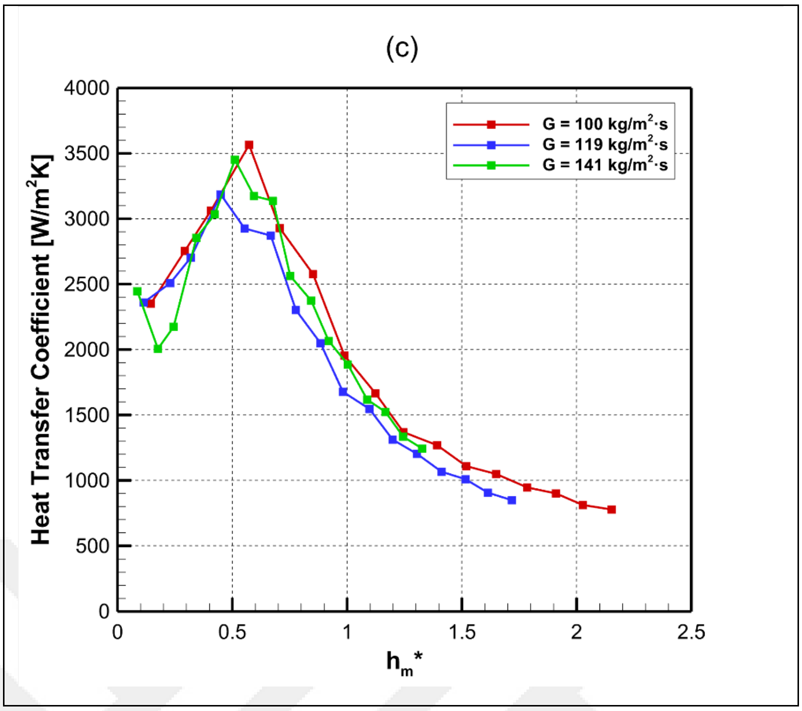


Figure 4.6. The Nusselt number as a function of (a) $x/d$ and (b) $h_m^*$, and (c) the heat transfer coefficient as a function of $h_m^*$ for cases of $G$ = 176, 241, and 297 kg/m$^2$·s with $q''$ = 17.2 – 18.3 kW/m$^2$ at 8.00 - 8.02 MPa and 18.5 - 20.9°C at the tube inlet.

### 4.2.2. Heat Transfer Characteristics of Microtube #2 ($d_i$ = 0.509 mm)

Figure 4.7 shows the variation of the Nusselt number, mean fluid temperature, and inner wall temperature as a function of $x/d$ where the error bars with a 95 percent confidence level are also shown. The mean fluid temperature and inner wall temperature rise monotonously; in addition, the mean temperature remains almost constant near the pseudo-critical temperature ($T_{pc}$ = 34.7ºC) where the specific heat is very high. The difference between the wall and mean temperature becomes minimum at $x/d$ = 140, and the Nusselt number peaks at the same point where the film temperature is almost equal to $T_{pc}$.

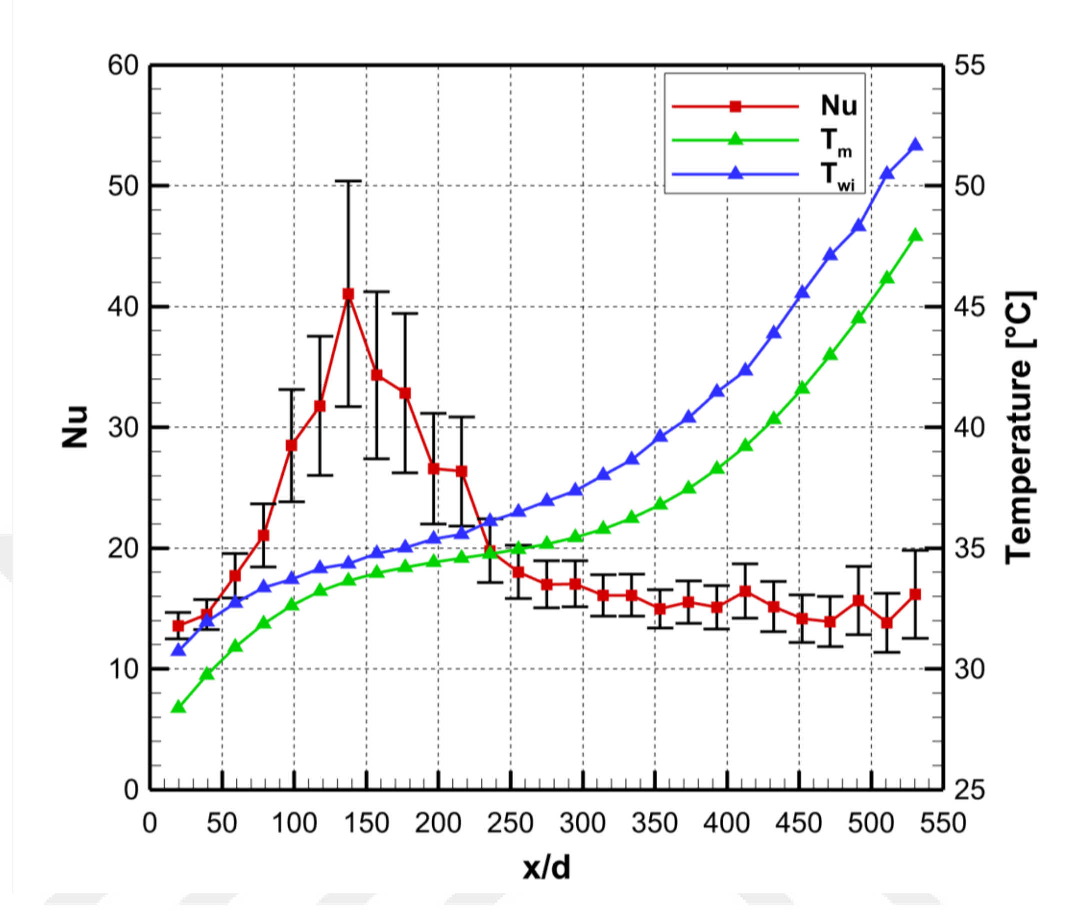


Figure 4.7. The mean fluid temperature, the inner wall temperature, and the Nusselt number as a function of *x/d* for the case of 7.99 MPa, 26.8°C, and *Re* = 485 at the tube inlet with $d_i$ = 0.509 mm, *G* = 60 kg/m$^2$·s and *q″/G* = 0.075 kJ/kg. Error bars are shown on the Nusselt number with a 95 percent confidence level. The uncertainty of the peak of *Nu* is 22.8 percent.

The effect of *q″/G* on heat transfer characteristics for almost constant mass flux values varying between 99 and 100 kg/m$^2$·s was examined in Figure 4.8. The Reynolds numbers at the tube inlet are between 807 and 812 when the *Re* at the outlet is ranging from 2100 to 2550 depending on the applied heat flux. In Figure 4.8 (a), 4 different *q″/G* values were plotted against *x/d*. The Nusselt number reaches a peak at around *x/d* = 215 when *q″/G* = 0.054 kJ/kg whereas it has a maximum at *x/d* = 100 if *q″/G* increases to 0.091 kJ/kg. Thus, the location of the peak of the *Nu* moves toward the tube inlet when the *q″/G* increases, since the mean fluid temperature reaches pseudo-critical temperature more rapidly.

In Figures 4.8 (b) and (c), the Nusselt number was plotted as a function of dimensionless specific enthalpies at both mean and film temperature. The peaks of Nusselt numbers given in Figure 4.8 (c) are located at the values of $h_f^*$ between 0.7 and 1.0. If $Nu$ is plotted against $h_m^*$, the peaks appear when $h_m^*$ is in between 0.5 and 0.7. This suggests that the fluid reaches the pseudo-critical temperature near the wall rather than at the core.

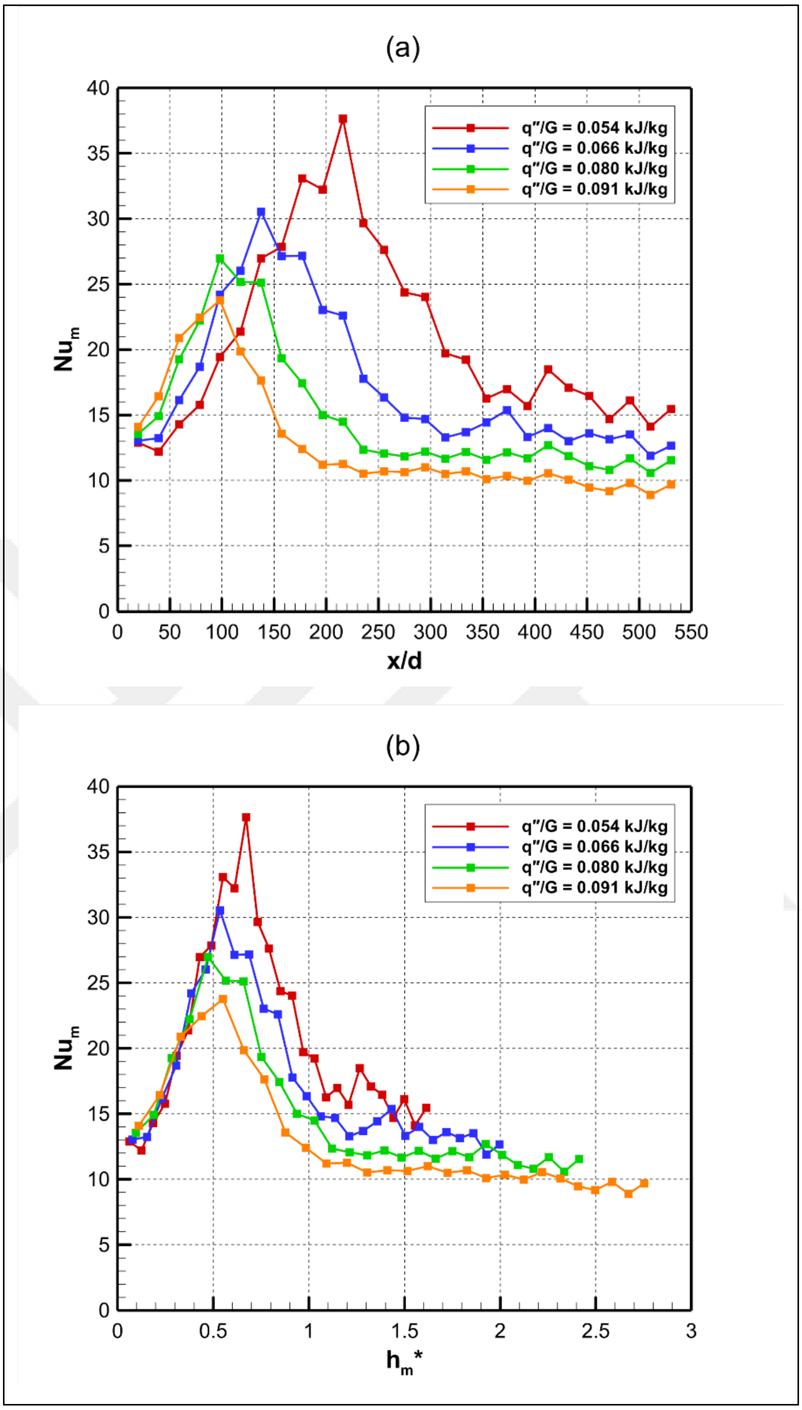
(a)
Nu_m
x/d
q''/G = 0.054 kJ/kg
q''/G = 0.066 kJ/kg
q''/G = 0.080 kJ/kg
q''/G = 0.091 kJ/kg
(b)
Nu_m
h_m*
q''/G = 0.054 kJ/kg
q''/G = 0.066 kJ/kg
q''/G = 0.080 kJ/kg
q''/G = 0.091 kJ/kg

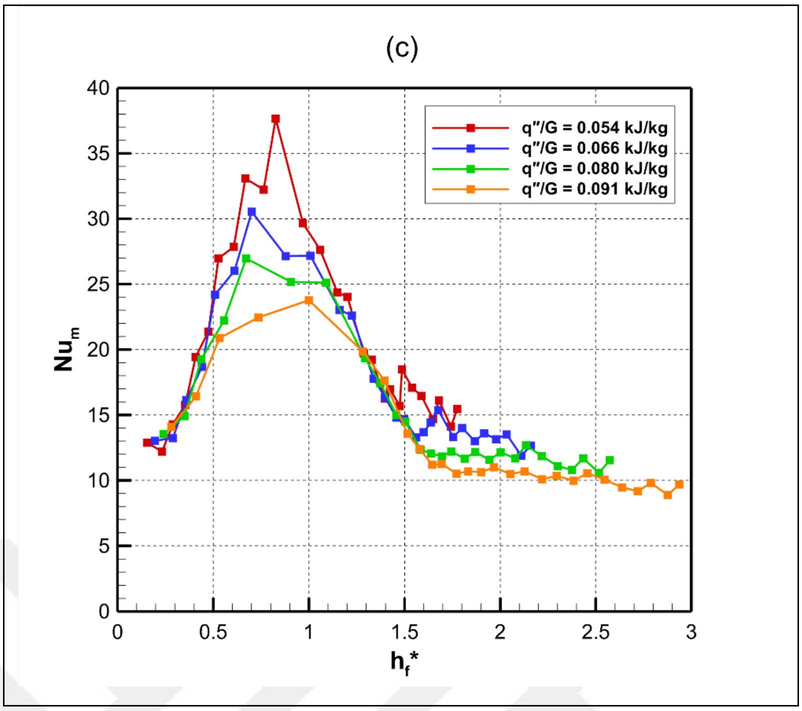


Figure 4.8. Nusselt number as a function of (a) *x/d*, (b) $h_m^*$ and (c) $h_f^*$ for cases of $q''/G$ = 0.054, 0.066, 0.080 and 0.091 kJ/kg with $G$ = 99 – 100 kg/m$^2$·s at 7.98-7.99 MPa, 27.0 – 27.1°C and $Re$ = 807 – 812 at the tube inlet.

The effect of mass flux on heat transfer characteristics for a given $q''/G$ ranging from 0.075 to 0.080 kJ/kg is examined in Figure 4.9. The main reason for selecting almost the same $q''/G$ is that the enthalpy increase from the inlet to the outlet is nearly the same when $q''/G$ is kept constant for different mass fluxes. Firstly, it is observed that the location where *Nu* reaches maximum gets closer to the tube inlet when the mass flux increases in Figure 4.9 (a). For a constant $q''/G$, high mass flux results in high heat flux. The higher heat flux results in a higher temperature gradient near the wall, and thus higher mass flux causes the mean fluid temperature near the wall to reach $T_{pc}$ at a location closer to the inlet (details are given in Section 4.2.1).

Secondly, there are some differences between the characteristics of $Nu_m$ and $Nu_f$. The variation of *Nu* at the film temperature may be erratic in some cases since the thermal conductivity is a strong function of temperature. The thermal conductivity decreases as the temperature increases except for a little peak near the pseudo-critical temperature as shown in Figure 1.1. Thus, the sudden drops in $Nu_f$ observed in these cases are caused by the variation in thermal conductivity as shown in Figure 4.9 (b).

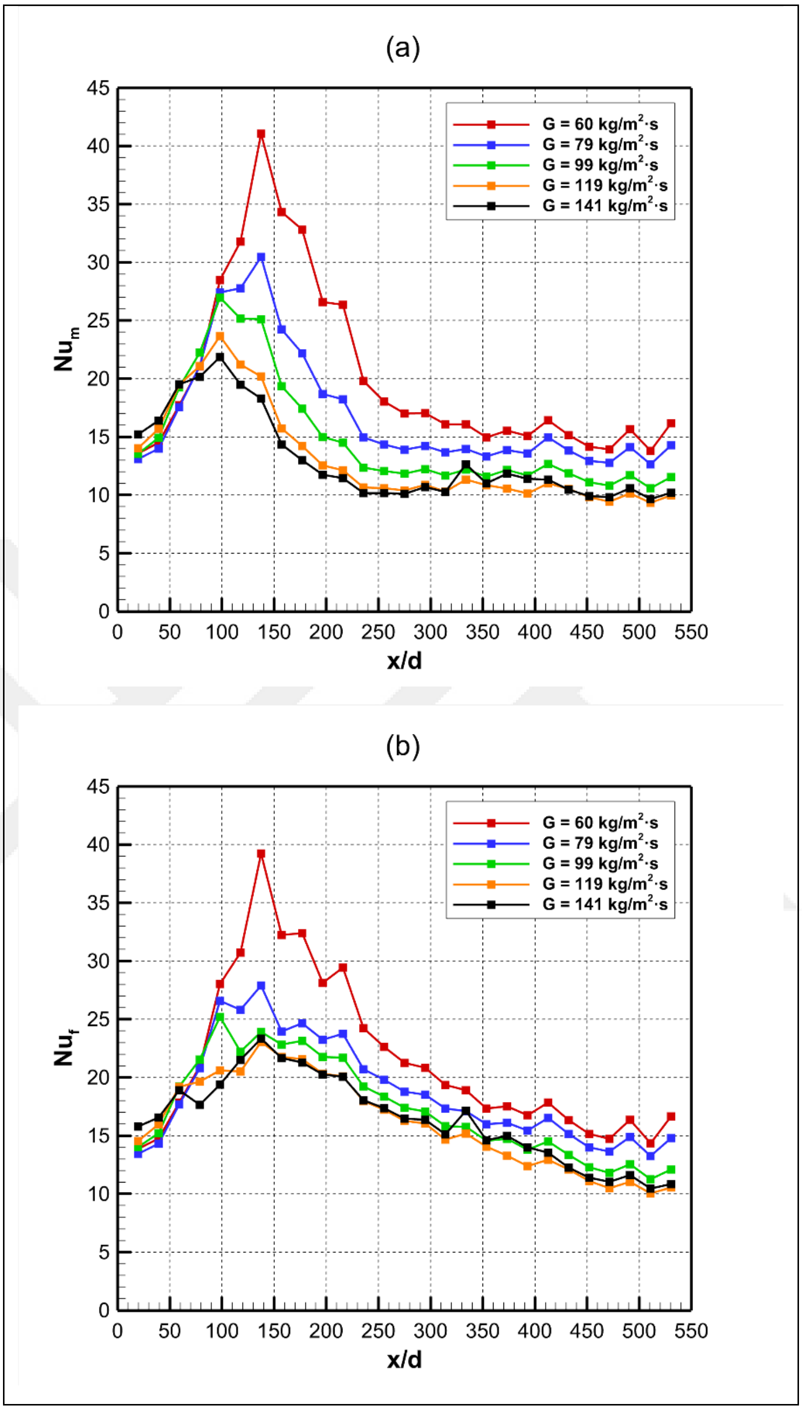
(a)
G = 60 kg/m²·s
G = 79 kg/m²·s
G = 99 kg/m²·s
G = 119 kg/m²·s
G = 141 kg/m²·s
Nu_m
x/d
(b)
G = 60 kg/m²·s
G = 79 kg/m²·s
G = 99 kg/m²·s
G = 119 kg/m²·s
G = 141 kg/m²·s
Nu_f
x/d

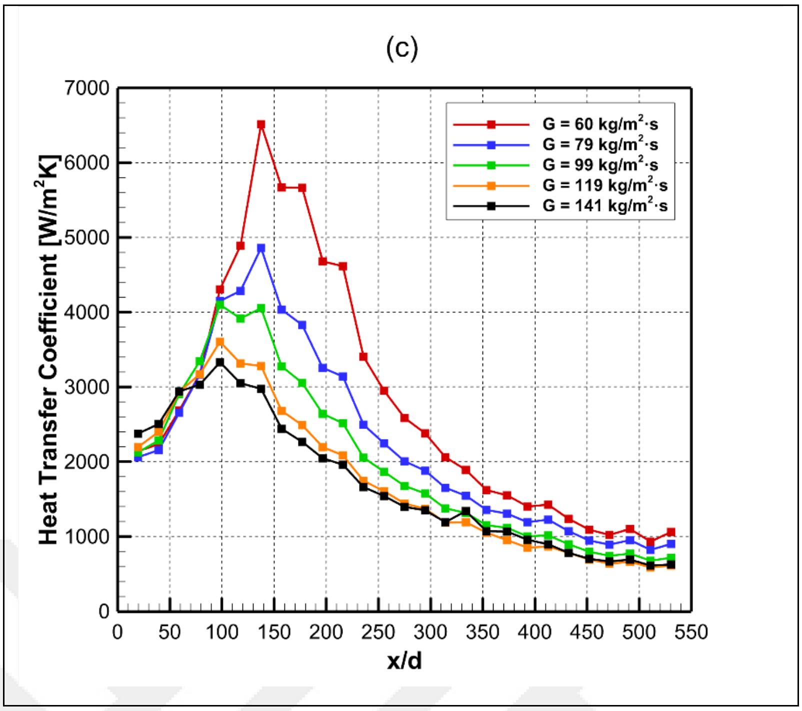


Figure 4.9. The Nusselt numbers (a) at the mean temperature and (b) at the film temperature, and (c) the heat transfer coefficient as a function of *x/d* for cases of $G$ = 60, 79, 99, 119, and 141 kg/m$^2$·s with $q''/G$ = 0.075 – 0.080 kJ/kg at 7.99 - 8.02 MPa and 26.8 - 27.5°C at the tube inlet.

Heat transfer characteristics were also examined for an almost constant heat flux value in Figure 4.10. The heat flux is set to an almost fixed value of $q''$ = 9.1 – 9.5 kW/m$^2$ and different mass flux values of 100, 119, and 141 kg/m$^2$·s were examined. A test with a lower $G$ such as 60 and 80 kg/m$^2$·s could not be included in this figure since the wall temperatures at lower mass fluxes may be high enough to cause damaging the thermocouples for a given $q''$. Moreover, the location where the Nusselt number has a peak moves toward the outlet as the mass flux increases as shown in Figure 4.10 (a) since the mean fluid temperature exceeds the pseudo-critical temperature at a location closer to the inlet for a lower $G$. When the Nusselt number was plotted against $h_m^*$ in Figure 4.10 (b), the cases with different mass fluxes behave like a single curve. This is caused by that the heat transfer coefficients (Figure 4.10 (c)) and the difference between the wall and mean temperatures are almost the same for different $G$ values.

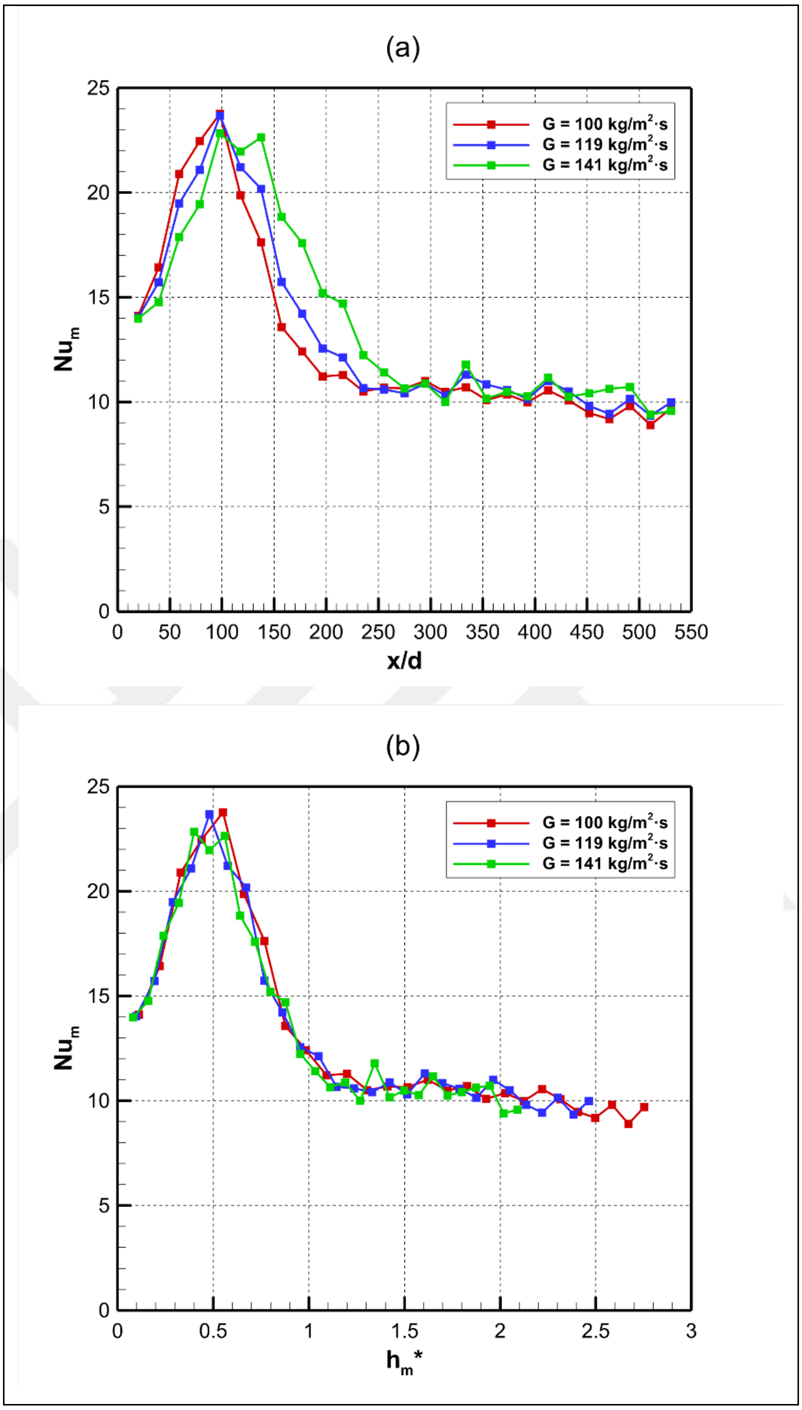
(a)
G = 100 kg/m²·s
G = 119 kg/m²·s
G = 141 kg/m²·s
Nu_m
x/d
(b)
G = 100 kg/m²·s
G = 119 kg/m²·s
G = 141 kg/m²·s
Nu_m
h_m*

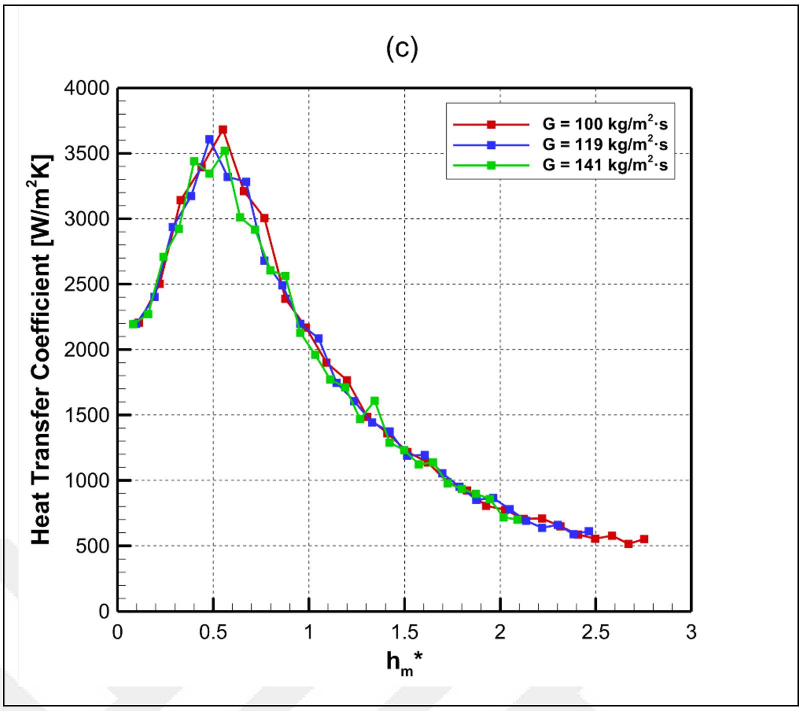


Figure 4.10. The Nusselt number as a function of (a) *x/d* and (b) $h_m{}^*$, and (c) the heat transfer coefficient as a function of $h_m{}^*$ for cases of $G$ = 100, 119, and 141 kg/m$^2$·s with $q''$ = 9.1 – 9.5 kW/m$^2$ at 7.99 - 8.02 MPa and 27.1 - 27.5°C at the tube inlet.

### 4.2.3. Heat Transfer Characteristics of Microtube #3 ($d_i$ = 0.847 mm)

Figure 4.11 shows the variation of the Nusselt number, mean fluid temperature, and inner wall temperature as a function of *x/d* where the error bars with a 95 percent confidence level are also shown. The mean fluid temperature and inner wall temperature rise monotonously; in addition, the mean temperature remains almost constant near the pseudo-critical temperature ($T_{pc}$ = 34.7ºC) where the specific heat is very high. The difference between the wall and mean temperature becomes minimum at *x/d* = 135, and the Nusselts number peaks at the same point where the film temperature is almost equal to $T_{pc}$. The up-down behavior in the Nusselt number which was caused by the buoyancy will be explained in detail in Section 4.2.5.

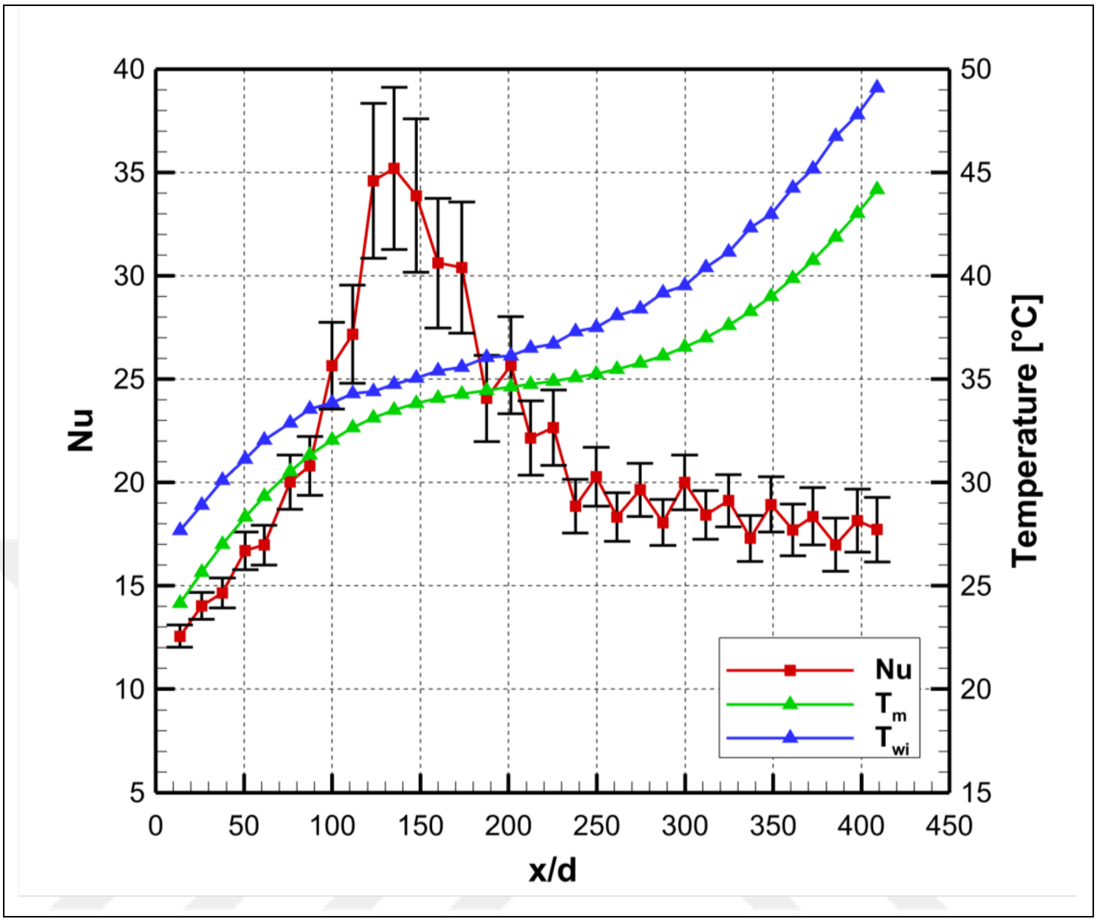


Figure 4.11. The mean fluid temperature, the inner wall temperature and the Nusselt number as a function of *x/d* for the case of 8.00 MPa, 22.3°C, and *Re* = 480 at the tube inlet with $d_i$ = 0.847 mm, *G* = 41 kg/m$^2$·s and *q″/G* = 0.101 kJ/kg. Error bars are shown on the Nusselt number with a 95 percent confidence level. The uncertainty of the peak of *Nu* is 11.2 percent.

The effect of *q″/G* on heat transfer characteristics for a constant mass flux value of 61 kg/m$^2$·s was examined in Figure 4.12. The Reynolds numbers at the tube inlet are between 726 and 736 while the *Re* at the outlet is ranging from 1830 to 2780 depending on the applied heat flux. In Figure 4.12 (a), 4 different *q″/G* values were plotted against *x/d*. The Nusselt number reaches a peak at around *x/d* = 225 when *q″/G* = 0.069 kJ/kg whereas it has a maximum at *x/d* = 100 if *q″/G* increases to 0.122 kJ/kg. Thus, the location of the peak of the *Nu* moves toward the tube inlet when the *q″/G* increases, since the mean fluid temperature reaches the pseudo-critical temperature more rapidly.

In Figures 4.12 (b) and (c), the Nusselt number was plotted as a function of dimensionless specific enthalpies at both mean and film temperature. The peaks of Nusselt numbers given in Figure 4.12 (c) are located at almost the same $h_f^*$ value where it is slightly less than 1. If $Nu$ is plotted against $h_m^*$, the peaks appear when $h_m^*$ is in between 0.6 and 0.7. This suggests that the fluid reaches the pseudo-critical temperature near the wall rather than at the core.

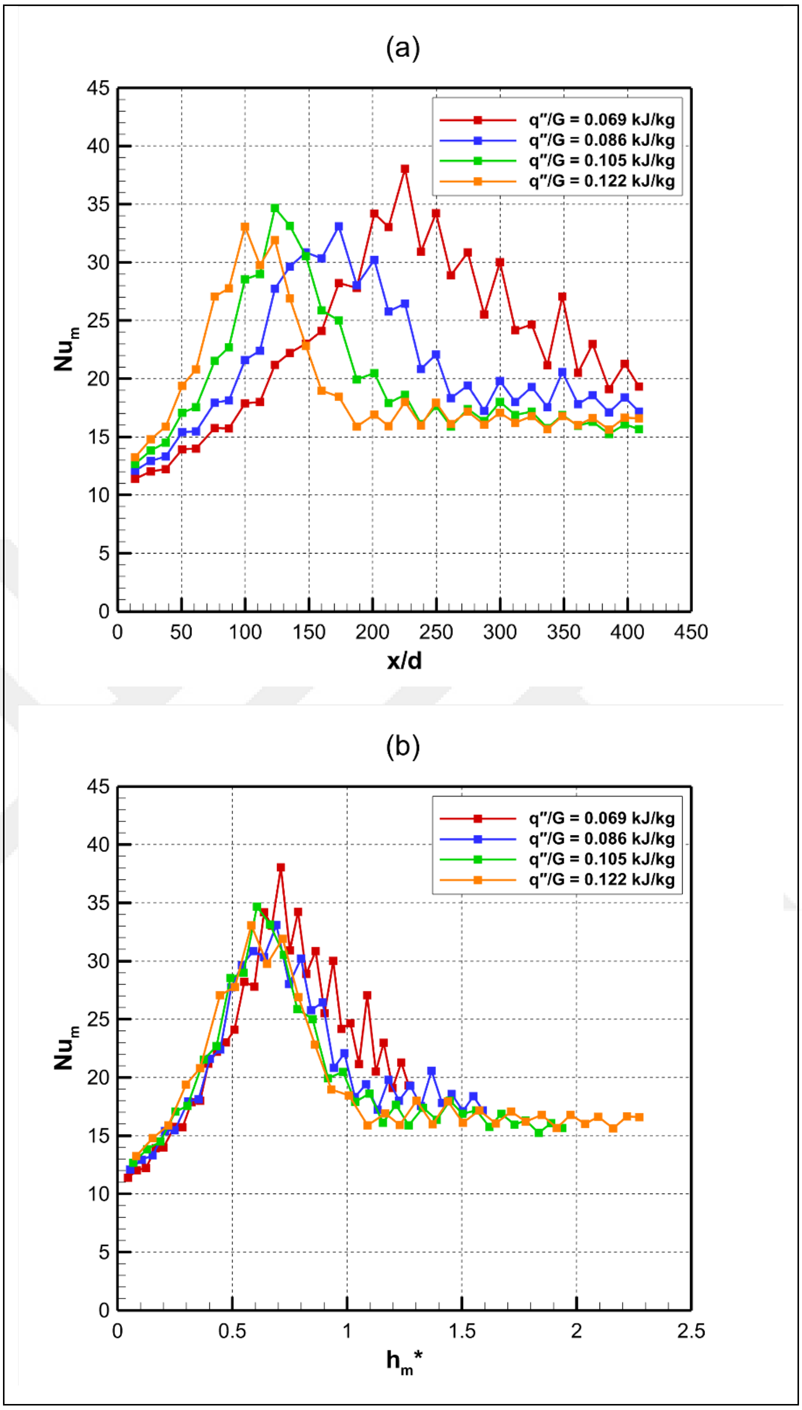
(a)
q"/G = 0.069 kJ/kg
q"/G = 0.086 kJ/kg
q"/G = 0.105 kJ/kg
q"/G = 0.122 kJ/kg
Nu_m
x/d
(b)
q"/G = 0.069 kJ/kg
q"/G = 0.086 kJ/kg
q"/G = 0.105 kJ/kg
q"/G = 0.122 kJ/kg
Nu_m
h_m*

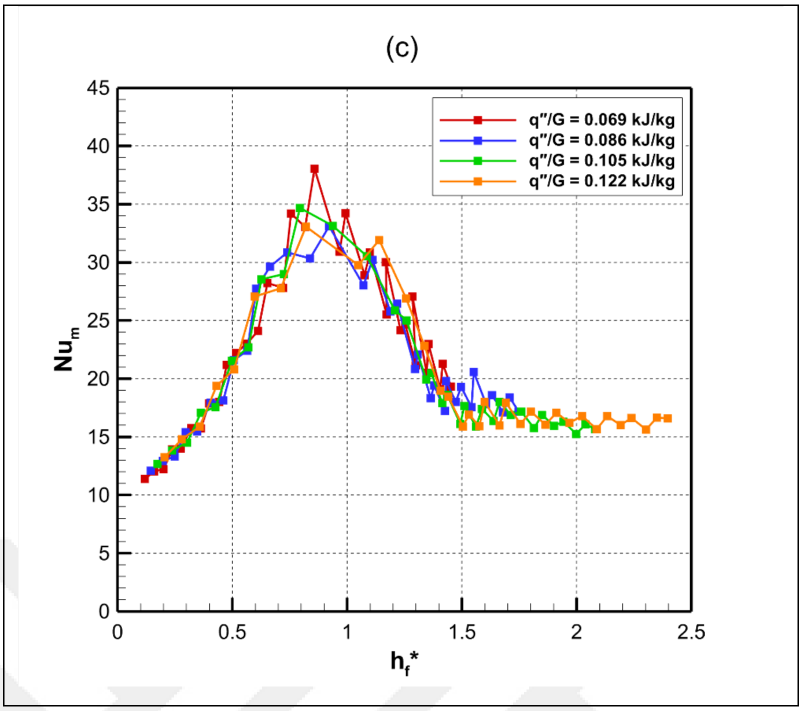


Figure 4.12. Nusselt number as a function of (a) *x/d*, (b) $h_m^*$ and (c) $h_f^*$ for cases of $q''/G$ = 0.069, 0.086, 0.105 and 0.122 kJ/kg with $G$ = 61 kg/m$^2$·s at 7.99-8.00 MPa, 21.9 – 22.0°C and *Re* = 709 – 717 at the tube inlet.

The effect of mass flux on heat transfer characteristics for a given $q''/G$ ranging from 0.083 to 0.091 kJ/kg is examined in Figure 4.13. The main reason for selecting almost the same $q''/G$ is that the enthalpy increase from the inlet to the outlet is nearly the same when $q''/G$ is kept constant for different mass fluxes. Firstly, it is observed that the location where *Nu* reaches maximum gets closer to the tube inlet when the mass flux increases in Figure 4.13 (a). For a constant $q''/G$, high mass flux results in high heat flux. The higher heat flux results in a higher temperature gradient near the wall, and thus higher mass flux causes the mean fluid temperature near the wall to reach $T_{pc}$ at a location closer to the inlet.

Secondly, there are some differences between the characteristics of *Nu* evaluated at the mean and film temperature. Although the variation of *Nu* at the film temperature may be erratic for the other diameters, no sudden drops were observed in this case. The up-down characteristic of *Nu* restrains the observation of sudden drops shown in other diameters.

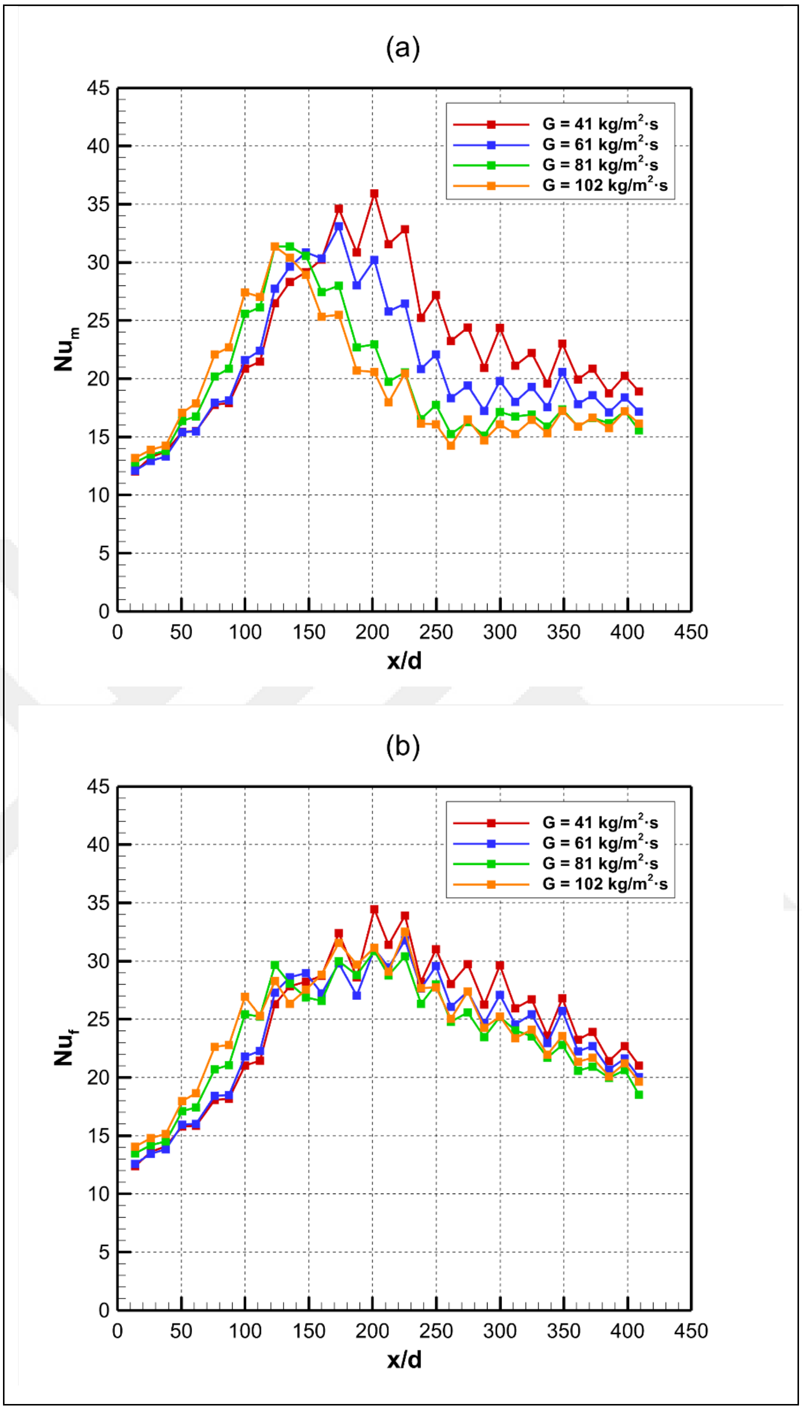

(a)
Nu_m
x/d
G = 41 kg/m²·s
G = 61 kg/m²·s
G = 81 kg/m²·s
G = 102 kg/m²·s
(b)
Nu_f
x/d
G = 41 kg/m²·s
G = 61 kg/m²·s
G = 81 kg/m²·s
G = 102 kg/m²·s

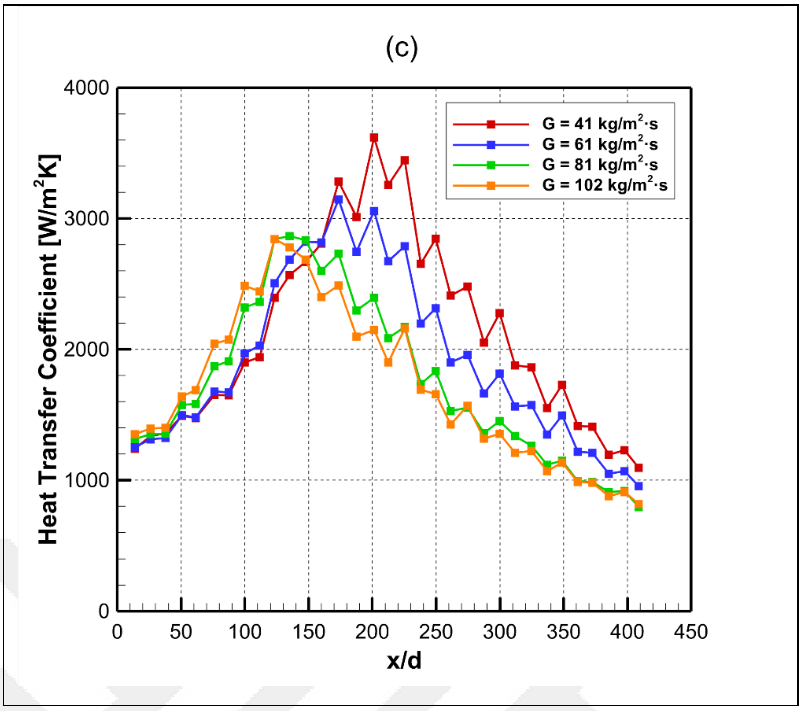


Figure 4.13. The Nusselt numbers (a) at the mean temperature and (b) at the film temperature, and (c) the heat transfer coefficient as a function of *x/d* for cases of $G$ = 41, 61, 81, and 102 kg/m$^2$·s with $q''/G$ = 0.083 – 0.090 kJ/kg at 7.99 - 8.00 MPa and 21.9 - 22.6°C at the tube inlet.

Heat transfer characteristics were also examined for an almost constant heat flux value in Figure 4.14. The heat flux is set to an almost fixed value of $q''$ = 7.2 – 7.4 kW/m$^2$ and different mass flux values of 61, 81, and 101 kg/m$^2$·s were examined. A test with a lower $G$ such as 40 kg/m$^2$·s could not be included in this figure since the wall temperatures at lower mass fluxes may be high enough to cause damaging the thermocouples for a given $q''$. Moreover, the location where the Nusselt number has a peak moves toward the outlet as the mass flux increases as shown in Figure 4.14 (a) since the mean fluid temperature exceeds the pseudo-critical temperature at a location closer to the inlet for a lower $G$. When the Nusselt number was plotted against $h_m^*$ in Figure 4.14 (b), the cases with different mass fluxes behave like a single curve. This has resulted from the fact that the heat transfer coefficients (Figure 4.14 (c)) and the difference between the wall and mean temperatures are almost the same for different $G$ values.

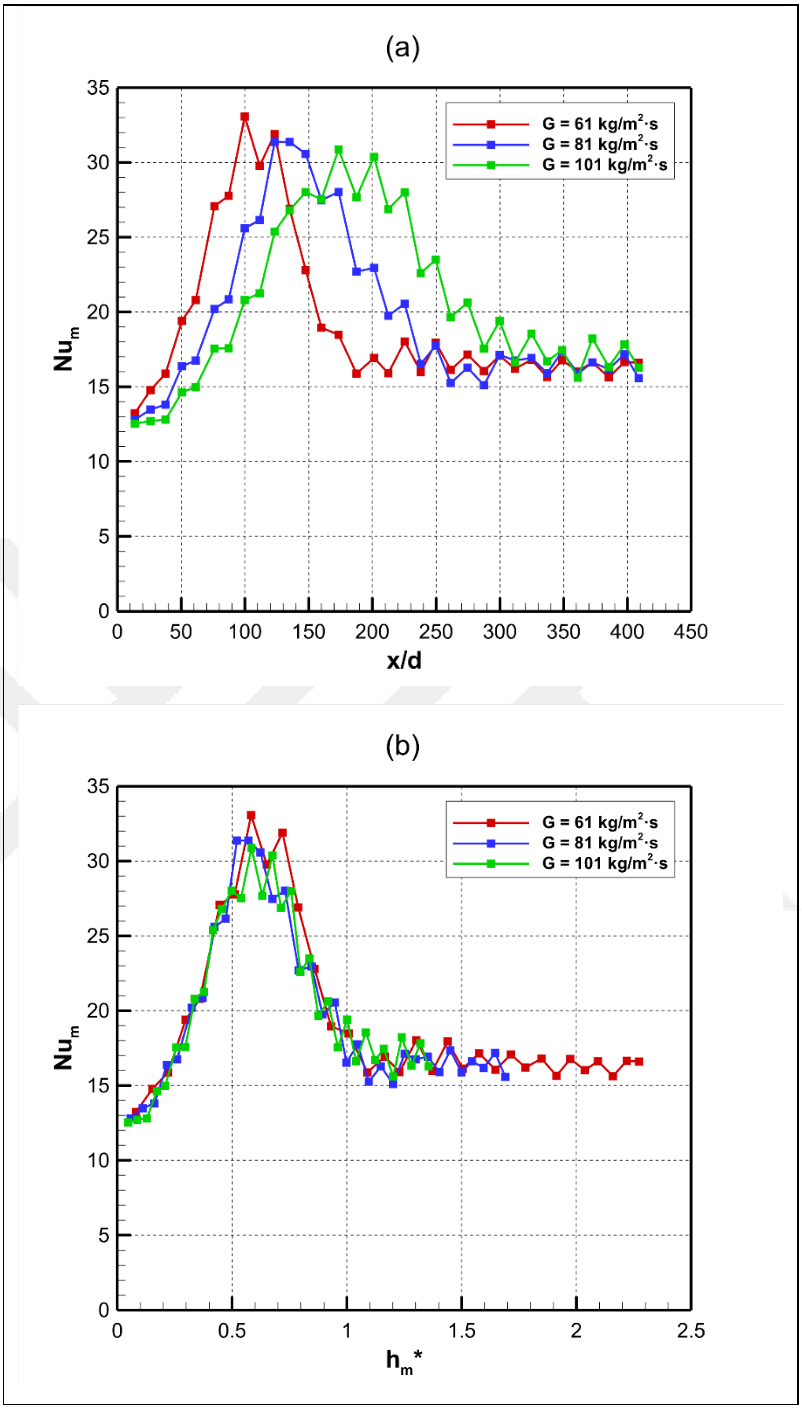
(a)
G = 61 kg/m²·s
G = 81 kg/m²·s
G = 101 kg/m²·s
Num
x/d
(b)
G = 61 kg/m²·s
G = 81 kg/m²·s
G = 101 kg/m²·s
Num
hm*

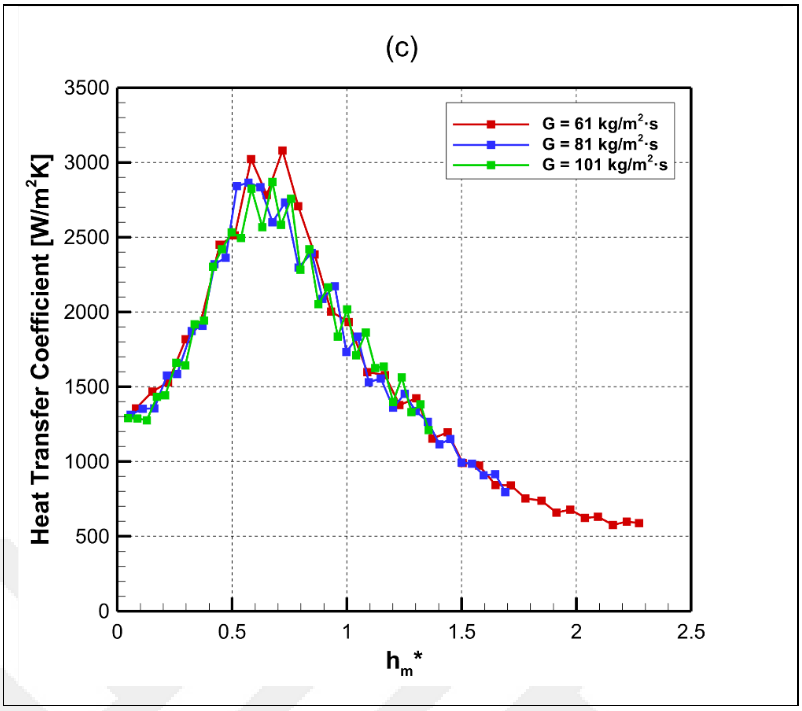


Figure 4.14. The Nusselt number as a function of (a) $x/d$ and (b) $h_m^*$, and (c) the heat transfer coefficient as a function of $h_m^*$ for cases of $G$ = 61, 81, and 101 kg/m$^2$·s with $q''$ = 7.2 – 7.4 kW/m$^2$ at 7.99 - 8.01 MPa and 22.0 - 22.6°C at the tube inlet.

### 4.2.4. The Effect of Diameter on Heat Transfer Characteristics

The effect of the diameter on the heat transfer characteristics was examined in Figures 4.15 and 4.16 for similar inlet Reynolds numbers with a given $q''/G$. In Figure 4.15, the inlet Reynolds numbers are 491, 542, and 480 for $d_i$ = 0.317, 0.509 and 0.847 mm, respectively. The corresponding outlet Reynolds numbers for these cases are 1850, 1990, and 1620. The heat transfer coefficients reach a maximum for $h_m^*$ between 0.5 and 0.6 where the film temperature is close to the pseudo-critical temperature for each diameter as shown in Figure 4.15 (a). Also, the heat transfer coefficients measured at the inlet increase as the inner diameter decreases. In contrast, the heat transfer coefficients become almost the same after $h_m^*$ = 0.8 no matter what the diameter is. When the Nusselt numbers at the mean temperature are plotted, the magnitude of $Nu$ along the tube is always greater for larger diameters as shown in Figure 4.15 (b). The magnitudes at and after the peak location are almost proportional to the diameters of the microtubes. Even though the heat transfer coefficients continue to decrease after $h_m^*$ = 1, the Nusselt numbers flatten for each diameter when $h_m^*$

exceeds 1 since the variation in thermal conductivity compensates for the decrease in *htc* (see Equation (3.10)). However, the Nusselt number at the film temperature (Figure 4.15 (c)) tends to decrease for $h_m^* > 1$.

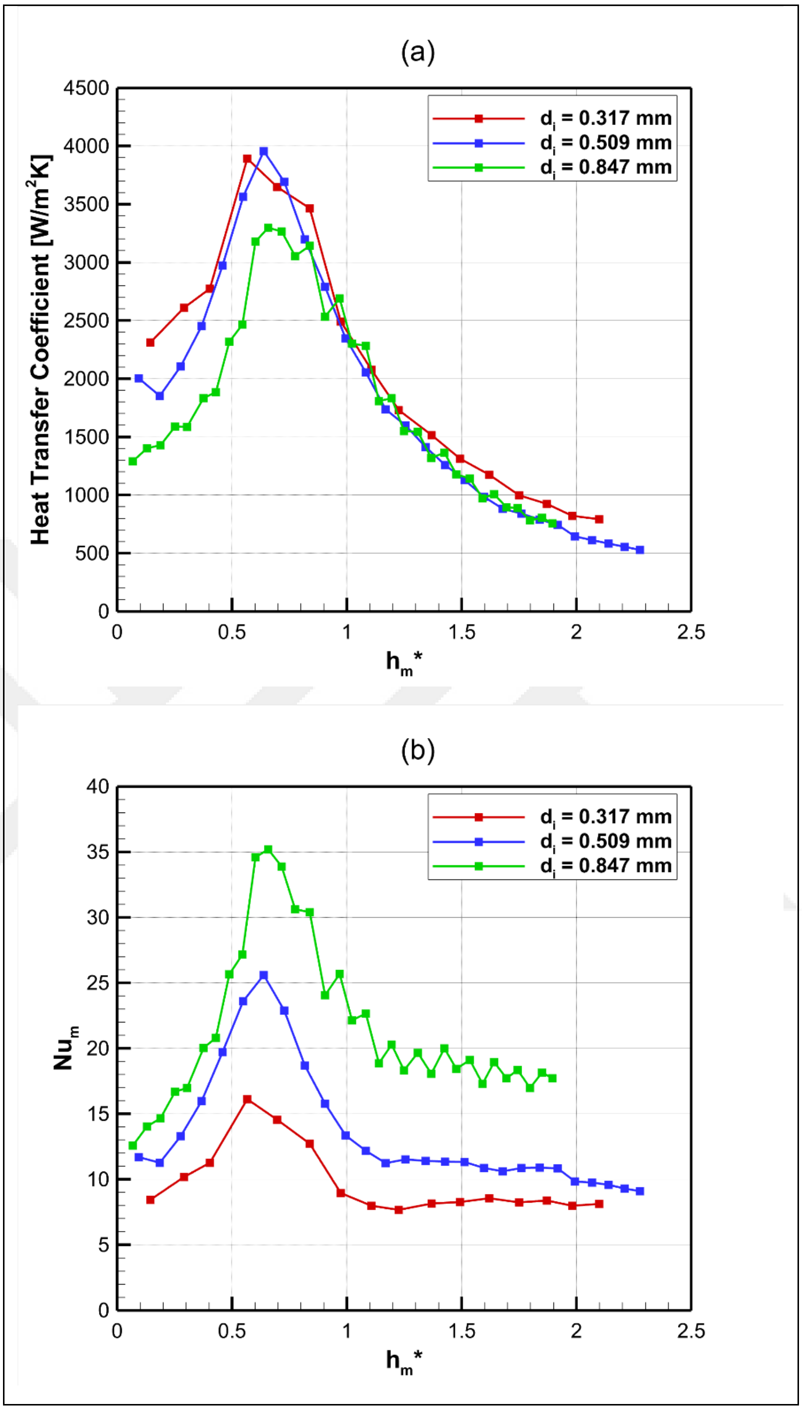

(a)
Heat Transfer Coefficient [W/m²K]
h_m*
d_i = 0.317 mm
d_i = 0.509 mm
d_i = 0.847 mm
(b)
Nu_m
h_m*
d_i = 0.317 mm
d_i = 0.509 mm
d_i = 0.847 mm

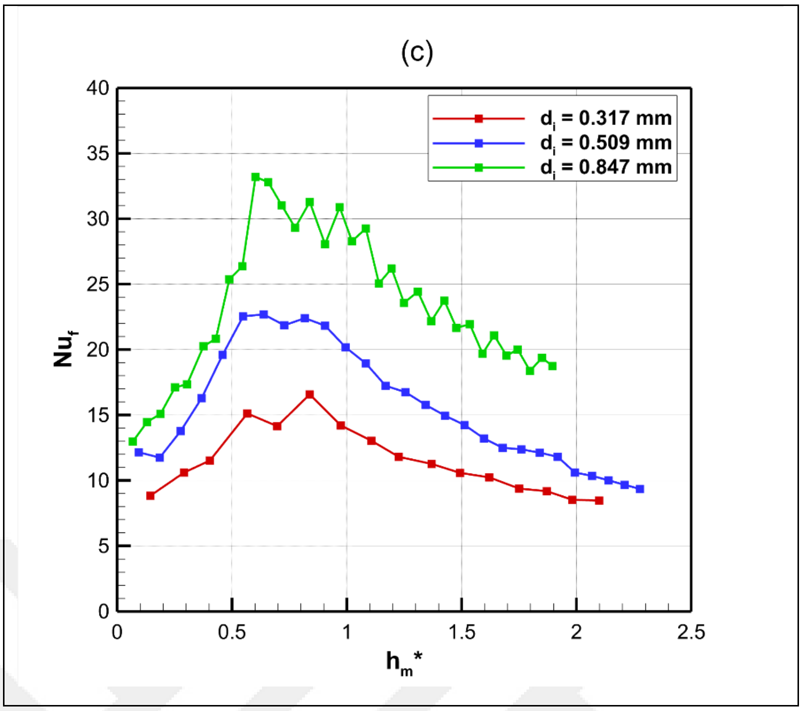


Figure 4.15. (a) The heat transfer coefficient, the Nusselt numbers (b) at the mean temperature and (c) at the film temperature as a function of $h_m^*$ at $Re$ = 480 – 542, 7.98 - 8.02 MPa and 19.7 - 22.3°C at the tube inlet with $q''/G$ = 0.093 – 0.101 kJ/kg for $d_i$ = 0.317, 0.509 and 0.847 mm.

In Figure 4.16, the inlet Reynolds numbers are 1029, 999, and 964 for $d_i$ = 0.317, 0.509 and 0.847 mm, respectively. The corresponding outlet Reynolds numbers for these cases are 3670, 3310, and 3050. The peaks in both heat transfer coefficient and Nusselt number appear around $h_m^*$ = 0.5 for each diameter. Different from the previous case (Figure 4.15), the Nusselt numbers up to the peak location closer to each other for $d_i$ = 0.509 and 0.847. After the peak, heat transfer coefficients exhibit the same behavior, and the magnitude of Nusselt numbers is proportional to the diameter.

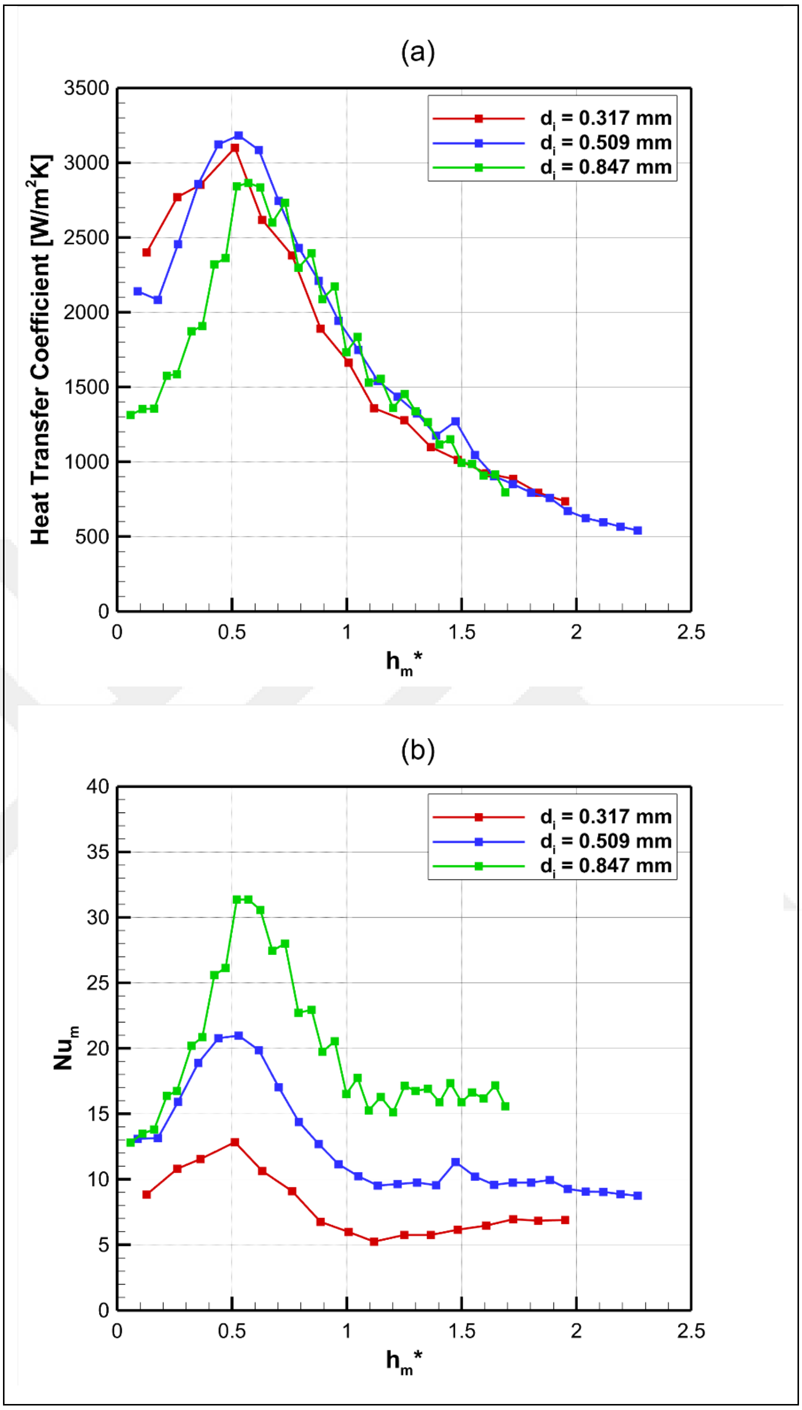
(a)
Heat Transfer Coefficient [W/m²K]
d_i = 0.317 mm
d_i = 0.509 mm
d_i = 0.847 mm
h_m*
(b)
Nu_m
d_i = 0.317 mm
d_i = 0.509 mm
d_i = 0.847 mm
h_m*

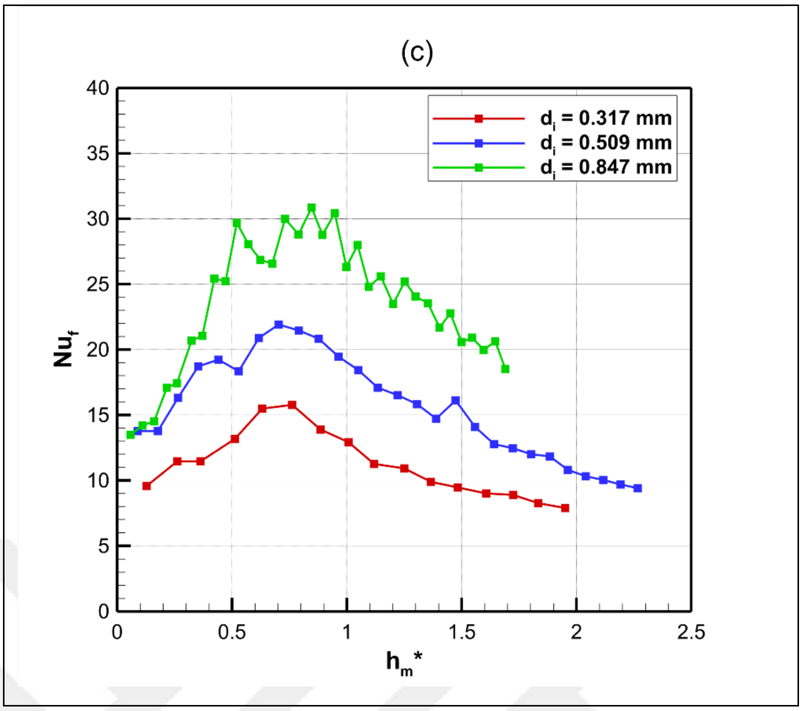


Figure 4.16. (a) The heat transfer coefficient, the Nusselt numbers (b) at the mean temperature and (c) at the film temperature as a function of $h_m^*$ at $Re$ = 964 – 1029, 7.99 - 8.01 MPa and 20.9 - 24.7°C at the tube inlet with $q''/G$ = 0.084 – 0.089 kJ/kg for $d_i$ = 0.317, 0.509 and 0.847 mm.

### 4.2.5. A Discussion on the Effect of Buoyancy

For a vertical flat plate, the Navier-Stokes boundary-layer equation that includes the free convection effect can be written as follows [50].

$$u\frac{\partial u}{\partial x} + v\frac{\partial u}{\partial y} = -\frac{1}{\rho}\frac{\partial p}{\partial x} + \frac{\mu}{\rho}\frac{\partial^2 u}{\partial y^2} + g\beta(T - T_\infty) \tag{4.1}$$

Where $g$ is the gravitational acceleration, $\beta$ is the thermal expansion coefficient and $T_\infty$ is the ambient temperature. This equation can be non-dimensionalized by substituting $X$ for $x/L$, $Y$ for $y/L$, $\theta$ for $(T - T_\infty)/(T_0 - T_\infty)$, $P$ for $(p - p_\infty)/(U_\infty^2/2g)$, $U$ for $u/U_\infty$, and $V$ for $v/U_\infty$ in Equation (4.1), and this results in

$$U\frac{\partial U}{\partial X} + V\frac{\partial U}{\partial Y} = -\frac{1}{2}\frac{\partial P}{\partial X} + \left(\frac{\mu}{\rho U_\infty L}\right)\frac{\partial^2 U}{\partial Y^2} + \left[\frac{g\beta L^3(T_0 - T_\infty)}{\nu^2}\right]\frac{\nu^2}{U_\infty^2 L^2}\theta \tag{4.2}$$

where $U_\infty$ is the free stream velocity over a flat plate, $T_0$ is the reference temperature, and $L$ is the characteristic length of the plate. When the coefficient of $\theta$ is of the order of 1 or larger in Equation (4.2), it determines whether the buoyancy will affect the velocity and temperature distribution or not. This coefficient is identical to the ratio of the Grashof number to the square of the Reynolds number which is also known as the Richardson number as shown in Equation (4.3). The Richardson number is used as a parameter to make a comparison between free and forced convection effects. The combined effects of free and forced convection (mixed convection) should be taken into account for $Ri \approx 1$, and thus, the Nusselt number expression will be of the form $Nu = f\,(Re_L, Gr_L, Pr)$. Free convection effects are more dominant and $Nu = f\,(Gr_L, Pr)$ for $Ri \gg 1$. In contrast, free convection effects can be neglected and $Nu = f\,(Re_L, Pr)$ for $Ri \ll 1$.

$$\frac{[g\beta L^3(T_0 - T_\infty)/\nu^2]}{(U_\infty L/\nu)^2} = \frac{Gr_L}{Re_L^2} = Ri \tag{4.3}$$

The above equations are for a flat plate, however, $sCO_2$ flows through microtubes are examined in this study. Therefore, the Grashof number for internal flows can be written as follows by substituting the characteristic length $L$ for $d_i$ in Equation (4.3). For internal flows, the reference temperature, $T_0$, and ambient temperature, $T_\infty$, can be replaced by $T_w$ and $T_m$, respectively.

$$Gr = \frac{g\beta(T_w - T_m)d_i^3}{\nu^2} = \frac{g\beta\Delta T d_i^3}{\nu^2} \tag{4.4}$$

where the temperature difference, $\Delta T$, is the difference between the inner wall and mean temperature. The buoyancy-influenced forced flows are classified into three categories such that the buoyancy force and flow are in the same direction (aiding or assisting flow), opposite direction (opposing flow), and perpendicular direction (transverse flow). Although Equations (4.1), (4.2), and (4.3) are derived for a vertical flat plate, it is theoretically proven that if the Richardson number is less than $10^{-3}$ in horizontal channels (transverse flow), the buoyancy becomes insignificant [26, 27].

$$Ri = \frac{Gr}{Re^2} < 10^{-3} \tag{4.5}$$

Some up-down behavior was observed in the Nusselt number plots, especially for the microtube that has an inner diameter of 0.847 mm and it can be explained as follows. As explained in Section 3.3, even and odd-numbered thermocouples are attached at the bottom and top of the microtube, respectively. The main reason to have up-down behavior in the Nusselt number is that thermocouples placed at the top and bottom measure different temperatures due to the buoyancy. The density of the $sCO_2$ is quite sensitive to the temperature, especially near the pseudo-critical point. As the $CO_2$ is heated, its density decreases, and $CO_2$ at the bottom moves upward with the buoyancy effect. As a result, there is a high-density fluid at the bottom and a low-density fluid at the top flowing through the microtube. The same discrepancy between the top and bottom surface was also observed by Yu et al. [36] in their study with supercritical water flows through horizontal tubes with inner diameters of 26 and 43 mm.

The effect of buoyancy increases as the diameter increases by the definition of the Richardson number as shown in Equation (4.5). Therefore, there is almost no up-down behavior for the flows through the microtube that has an inner diameter of 0.317 mm whereas they are very obvious for $d_i$ = 0.847 (see Figures 4.15, 4.16, and 4.17). Moreover, again from the definition of the Richardson number, the difference between the top and bottom shrinks as the Reynolds number increases as shown in Figure 4.13 since the forced convection effects dominate the free convection effects for the higher *Re*. The results are quite comparable with the results in [36–38].

In Figure 4.17, the effect of buoyancy on different inner diameters is examined at very low $q''/G$ for the inlet Reynolds numbers around 1000. The outlet Reynolds numbers are 1230, 1290, and 1210 for the inner diameters of 0.317, 0.509, and 0.847 mm, respectively. The corresponding average temperature difference between the inner wall and mean are 2.2, 1.0, and 1.2°C for these cases. Note that neither the mean fluid temperature nor the film temperature has exceeded the pseudo-critical temperature in these cases. On the same plot, *Nu* = 4.364 which is an analytical solution for laminar flows under constant heat flux boundary condition with constant thermophysical properties, and the criteria for the buoyancy defined with the Richardson number given in Equation (4.5) are also included.

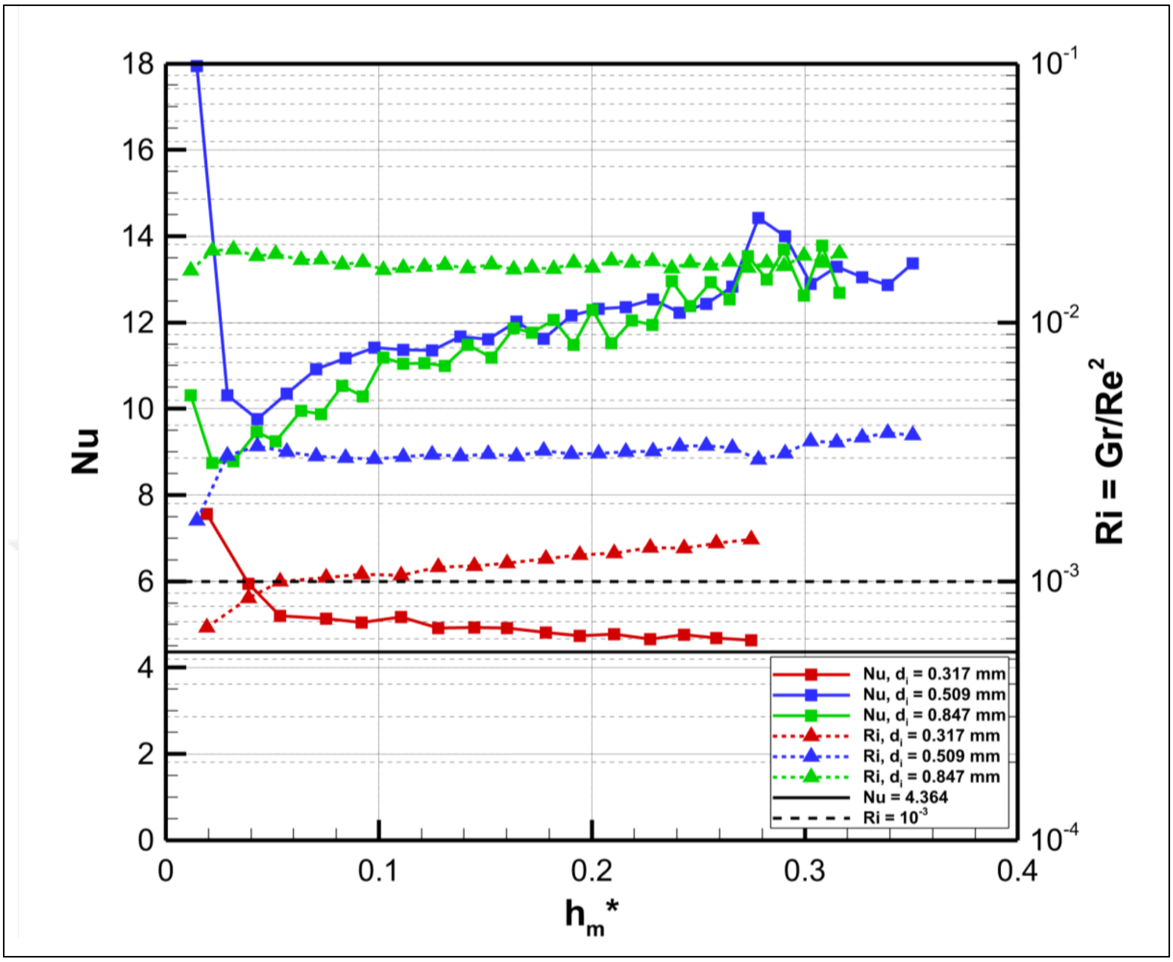


Figure 4.17. The Nusselt number and Richardson number as a function of $h_m^*$ at $Re$ = 966 – 1016, 7.99 - 8.02 MPa and 21.0 – 24.5°C at the tube inlet with $q''/G$ = 0.012 – 0.017 kJ/kg for $d_i$ = 0.317, 0.509 and 0.847 mm. The Richardson numbers are evaluated at the mean temperature.

For $d_i$ = 0.317 mm in Figure 4.17, the Richardson number varies between 0.0010 and 0.0015, and the Nusselt number lies between 4.63 and 5.05. When the diameter increases to 0.509 mm, $Ri$ is around 0.003, and the $Nu$ increases from 10 to 14. For the largest diameter, namely, 0.847 mm, $Ri$ is almost equal to 0.020 and $Nu$ gradually increases from 9 to 13. Though the properties of the $CO_2$ are quite sensitive to the temperature, the experimental Nusselt number was approached to the theoretical value with the constant properties for $d_i$ = 0.317 mm. Thus, it can be said that the heat transfer characteristic was not affected by the buoyancy if the Richardson number is around 0.001. This proves the validity of the criteria given in Equation (4.5) and [27]. Note that the uncertainty in the Nusselt number is about 19 and 12 percent through the microtube for $d_i$ = 0.509 and 0.847 mm, respectively. However, the uncertainty is almost 5 percent along the tube for $d_i = 0.317$ mm. Furthermore, the buoyancy starts to be effective on heat transfer activity if the Richardson number is more than trebled as observed for $d_i = 0.509$ and 0.847 mm.

The peak in the Nusselt number was associated with the high specific heat at the pseudo-critical temperature in previous sections. It can be explained in more detail as follows. Firstly, high specific heat means a high Prandtl number near the pseudo-critical temperature, and thus, the thermal boundary layer for developing flow is very thin compared to the momentum boundary layer as explained in our study [51]. This results in a steeper temperature profile at the wall, and accordingly, a high heat transfer rate. Apart from reasoning the peak with high specific heat, a rapid decrease in the density prompts the thermal acceleration and buoyancy effects. The thermal acceleration leads to a high velocity and temperature gradient in the axial direction which yields a high heat transfer rate. Also, the thermal expansion coefficient peaks at $T_{pc}$ which substantially increases the Grashof number. The secondary flow formed in the transverse direction due to the buoyancy also contributes to the enhancement of the heat transfer at the peak location.

In Figure 4.18, the effect of the buoyancy on the cases examined in Figure 4.15 was shown. In addition to Figure 4.15 (b), the Richardson number evaluated at the mean temperature and film temperature were included in the same plot. The Richardson numbers at the mean and film temperatures in these cases are always greater than 0.001 showing that the buoyancy is significant. For each diameter, $Ri_m$ and $Ri_f$ have similar characteristics along the tube except for the location of their maximum value. $Ri_m$ experiences a maximum at $h_m^* = 1$ whereas $Ri_f$ reaches a maximum between 0.6 and 0.7 since the mean fluid temperature is equal to the pseudo-critical temperature at $h_m^* = 1$. However, the peak in the Nusselt number was better defined by the maximum of the Richardson number at the film temperature as shown in Figure 4.18 (b) which indicates the effect of buoyancy on the peak of $Nu$. The magnitudes of $Ri_m$ at the peak location is 0.062, 0.180 and 0.535 for $d_i = 0.317$, 0.509 and 0.847, respectively.

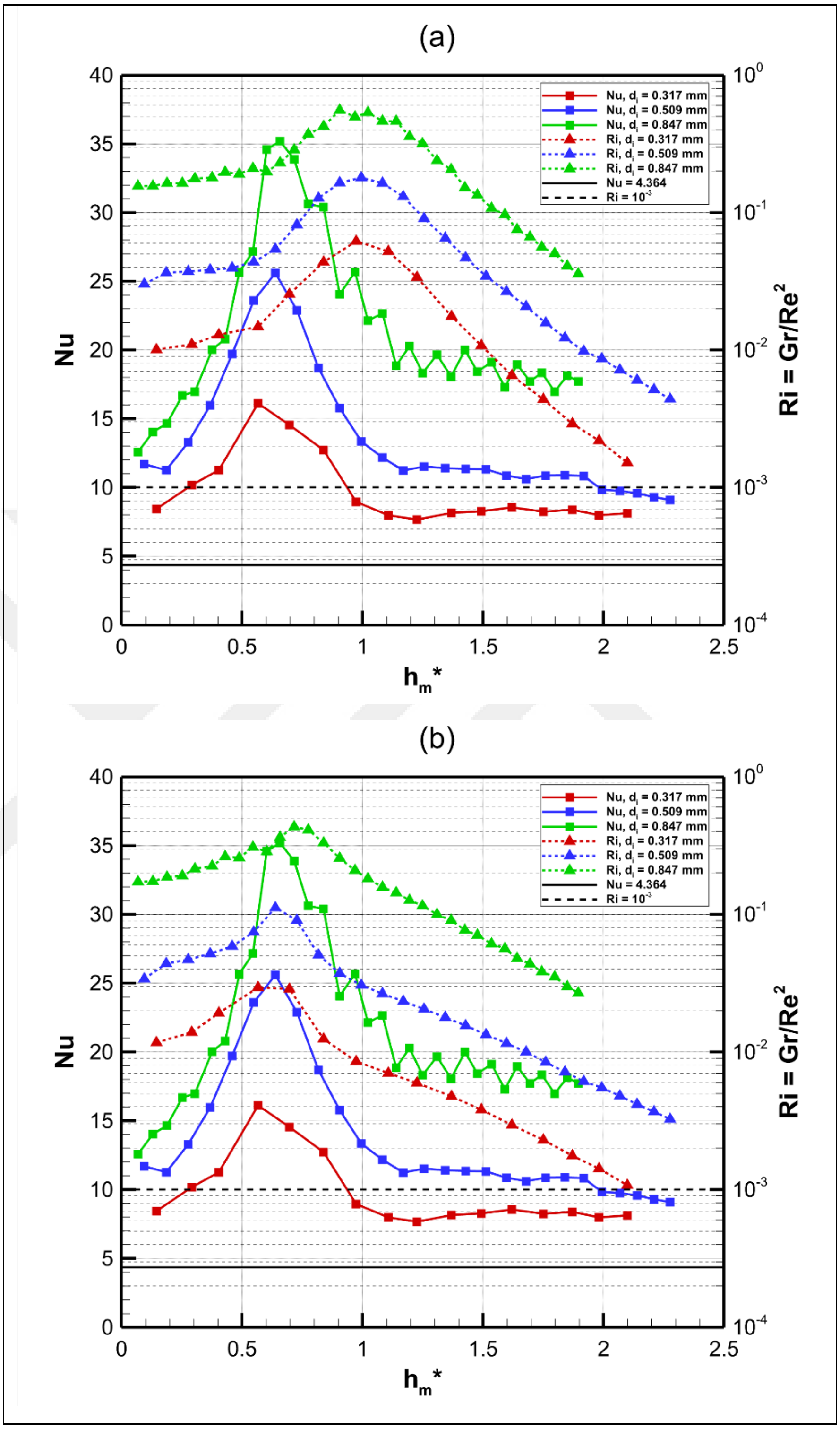


Figure 4.18. The Nusselt number and Richardson number as a function of $h_m^*$ at $Re$ = 480 – 542, 7.98 - 8.02 MPa and 19.7 – 22.3°C at the tube inlet with $q''/G$ = 0.093 – 0.101 kJ/kg for $d_i$ = 0.317, 0.509 and 0.847 mm. The Richardson numbers are evaluated (a) at the mean temperature and (b) at the film temperature which is the same case as Figure 4.15.

In Figure 4.19, the effect of the buoyancy on the cases examined in Figure 4.16 was shown. In addition to Figure 4.16 (b), the Richardson number evaluated at the mean temperature and film temperature were included in the same plot. The inlet Reynolds numbers are around 1000 whereas the outlet Reynolds numbers vary between 3000 and 3700. The Richardson numbers at the mean and film temperatures in these cases are always greater than 0.001 except for $Ri_f$ after $h_m^* = 1.5$ for $d_i = 0.317$ mm. In this case, the magnitudes of $Ri_m$ at the peak location reduce to 0.040, 0.107, and 0.344 for the diameters of 0.317, 0.509, and 0.847, respectively. The main reason for this is that the $Re$ increases, and accordingly, $\Delta T$ increases proportionally. However, the Richardson number is a function of $1/Re^2$ (see Equation (4.5)), and thus the rise in the $Re$ has more affected the $Ri$ when Figure 4.19 is compared to Figure 4.18.

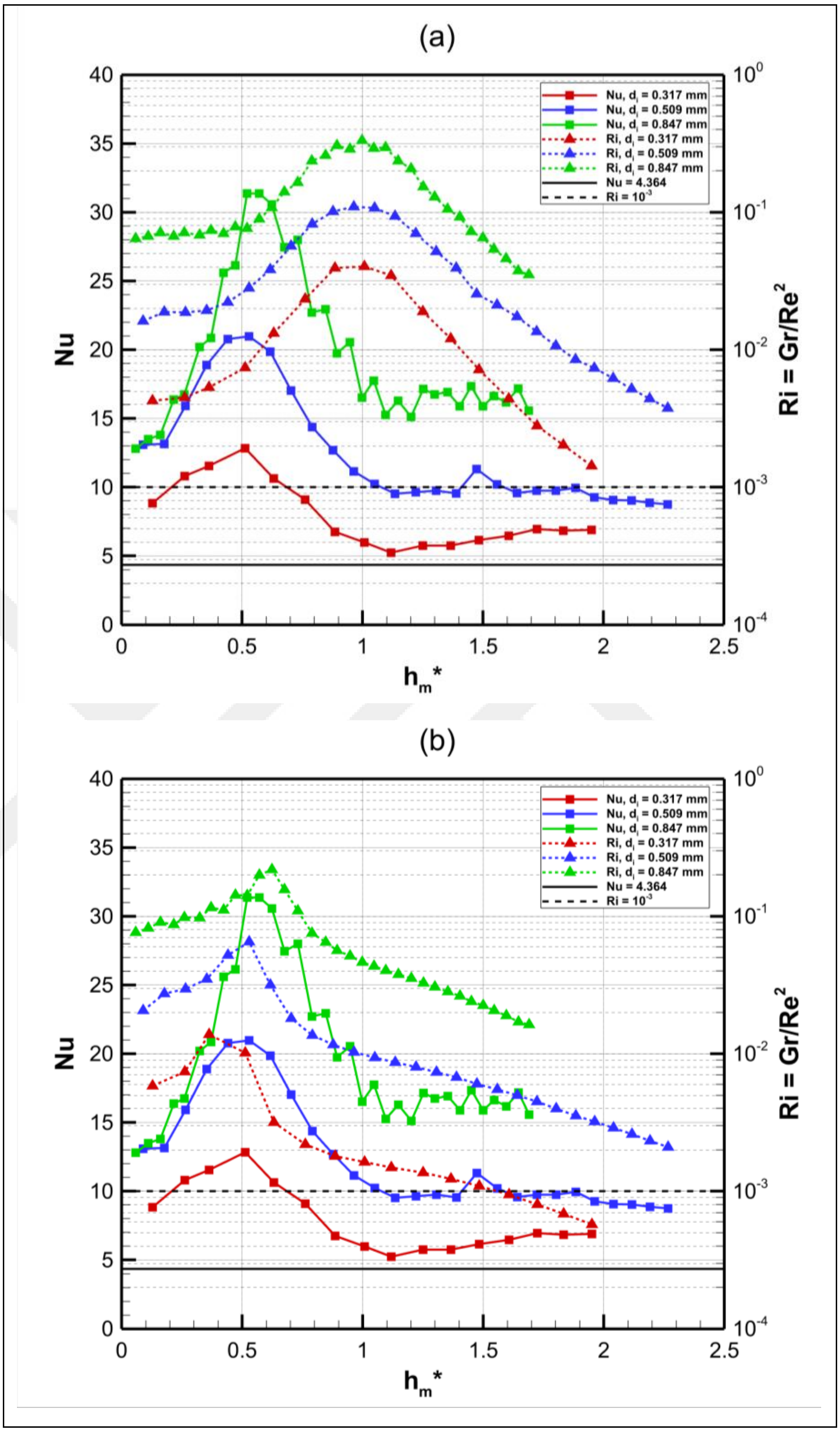


Figure 4.19. The Nusselt number and Richardson number as a function of $h_m^*$ at $Re$ = 964 – 1029, 7.99 - 8.01 MPa and 20.9 - 24.7°C at the tube inlet with $q''/G$ = 0.084 – 0.089 kJ/kg for $d_i$ = 0.317, 0.509 and 0.847 mm. The Richardson numbers are evaluated (a) at the mean temperature and (b) at the film temperature which is the same case as Figure 4.16.

# 5. CONCLUSION

Research on convective heat transfer experiments through microtubes faces many challenges. Conventional methods of measuring the tube wall temperature may not be applicable to the microtube due to its reduced size. A microtube experiences more heat loss from its outer surface because the ratio of the outer diameter to the inner diameter is large. Often it is not possible to provide thermal insulation on the outer surface since the critical radius of insulation can easily be larger than the tube radius. Furthermore, the heat loss becomes significant compared to the total energy input when the flow rate is low. Especially if the working fluid is gas, it is extremely difficult to measure the bulk temperature at the tube outlet as the heat loss in the mixing chamber is relatively large compared to the enthalpy flux of fluid out of the microtube.

The present study, therefore, has developed a method to measure the tube wall temperature by manufacturing small solder casts in each of which a thermocouple is embedded. Subsequently, the solder cast is placed on the half part of the tube with a thermal paste and an instant adhesive. Since the solder cast has a large surface area, heat loss at the location of the solder cast is augmented. Therefore, a detailed analysis has been conducted to examine the effect of the solder cast on heat loss increase and axial conduction along the tube.

The local heat generation within the tube wall is obtained with the electrical resistivity of the tube wall that depends on the wall temperature. The heat loss from the outer surface of the tube wall is locally calculated as a function of the temperature difference between the wall and the environment. Thus, the local net heat flux to fluid flows is calculated from the local heat generation underneath the solder cast, the local heat loss from the tube surface, and the axial heat conduction along the tube wall. The net heat flux is then integrated to yield the local mean enthalpy from which the mean temperature is calculated along the tube.

The method of using the solder cast developed in this study has been validated with laminar water flows through a microtube, 0.501 mm in inner diameter. All Nusselt numbers are found to lie between 4.36 and 4.36 +10 percent. The outcome of the measured Nusselt numbers being greater than 4.36 is not surprising since the secondary flow caused by the change in fluid properties enhances heat transfer. The test results show the discrepancy between the two methods of analyses with and without the effect of the solder casts to be not significant.

The method of using the solder cast is applied to supercritical $CO_2$ flowing in horizontal microtubes having inner diameters of 0.317, 0.509, and 0.847 mm at 8.0 MPa. The inlet Reynolds number was kept lower than 1100 during the experiments. A peak in the Nusselt number was observed when the fluid temperature approaches the pseudo-critical temperature at which the properties of $CO_2$ undergo a rapid change. The high specific heat at the pseudo-critical temperature was related to the peak in the Nusselt number. High specific heat indicates a high Prandtl number at the pseudo-critical temperature, implying that the thermal boundary layer for developing flow is quite thin in comparison to the momentum boundary layer. As a result, the temperature profile at the wall becomes steeper, leading to an enhanced heat transfer rate.

When the effect of heat flux on heat transfer activity for a constant mass flux was examined, it was found that the location of the peak moves toward the tube inlet. This is because the mean fluid temperature exceeds the pseudo-critical temperature more rapidly when the heat flux is higher. Moreover, the effect of mass flux was studied with the heat flux-to-mass flux ratio kept constant. The results showed that the Nusselt number experiences an earlier maximum for higher mass fluxes. This was associated with the higher temperature gradient near the wall for high mass flux since high mass flux results in high heat flux for a constant heat flux-to-mass flux ratio. Finally, the effect of mass flux was examined for a constant heat flux. The peak location of the Nusselt number moved toward the outlet for high mass fluxes. Also, the heat transfer coefficients and Nusselt numbers behaved like a single curve when they were plotted against dimensionless specific enthalpy at the mean temperature.

Finally, the effect of diameter on heat transfer characteristics was investigated. The magnitude of the Nusselt number increased as the diameter was increased which was reasoned with the buoyancy effects. The effect of buoyancy was judged by using the Richardson number, and it was shown that the Nusselt number converges to 4.364 when the mean fluid temperature does not exceed the pseudo-critical temperature and the buoyancy is not significant. Furthermore, it is observed that the Grashof number increased significantly at the pseudo-critical temperature since the volume expansivity peaked at the same point. As a result, the buoyancy-induced secondary flow in the transverse direction also contributed to the augmentation of heat transfer at the peak point.

## REFERENCES

1. Dixit T, Ghosh I. Review of micro- and mini-channel heat sinks and heat exchangers for single phase fl uids. *Renewable and Sustainable Energy Reviews* 2015; 41: 1298–1311.

2. Bucci A, Celata GP, Cumo M, et al. Water single-phase fluid flow and heat transfer in capillary tubes. *International Conference on Microchannels and Minichannels* 2003; 1: 319–326.

3. Meyer JP, Everts M. Single-phase mixed convection of developing and fully developed flow in smooth horizontal circular tubes in the laminar and transitional flow regimes. *International Journal of Heat and Mass Transfer* 2018; 117: 1251–1273.

4. Jiang PX, Zhang Y, Xu YJ, et al. Experimental and numerical investigation of convection heat transfer of $CO_2$ at supercritical pressures in a vertical tube at low Reynolds numbers. *International Journal of Thermal Sciences* 2008; 47: 998–1011.

5. Lei X, Zhang Q, Zhang J, et al. Experimental and numerical investigation of convective heat transfer of supercritical carbon dioxide at low mass fluxes. *Applied Sciences (Switzerland)* 2017; 7: 1–18.

6. Lei X, Zhang J, Gou L, et al. Experimental study on convection heat transfer of supercritical $CO_2$ in small upward channels. *Energy* 2019; 176: 119–130.

7. Zhang H, Xu J, Wang Q, et al. Multiple wall temperature peaks during forced convective heat transfer of supercritical carbon dioxide in tubes. *International Journal of Heat and Mass Transfer* 2021; 172: 121171.

8. Anderson RL, Adams RK, Duggins BC. Limitations of Thermocouples in Temperature Measurements. *25th ISA Anaheim CA* 1979; 1–33.

9. Kim DE, Kim MH. Experimental study of the effects of flow acceleration and buoyancy on heat transfer in a supercritical fluid flow in a circular tube. *Nuclear Engineering and Design* 2010; 240: 3336–3349.

10. Kline N, Feuerstein F, Tavoularis S. Onset of heat transfer deterioration in vertical

pipe flows of $CO_2$ at supercritical pressures. *International Journal of Heat and Mass Transfer* 2018; 118: 1056–1068.

11. Jiang PX, Zhang Y, Shi RF. Experimental and numerical investigation of convection heat transfer of $CO_2$ at supercritical pressures in a vertical mini-tube. *International Journal of Heat and Mass Transfer* 2008; 51: 3052–3056.

12. Sadaghiani AK, Koşar A. Numerical and experimental investigation on the effects of diameter and length on high mass flux subcooled flow boiling in horizontal microtubes. *International Journal of Heat and Mass Transfer* 2016; 92: 824–837.

13. Cooper TE, Meyer JF, Field RJ. Liquid Crystal Thermography and Its Application To the Study of Convective Heat Transfer. *American Society of Mechanical Engineers (Paper)* 1975; 442–450.

14. Muwanga R, Hassan I. Local heat transfer measurements in microchannels using liquid crystal thermography: methodology development and validation. *Journal of Heat Transfer* 2006; 128: 617–626.

15. Lin TY, Yang CY. An experimental investigation on forced convection heat transfer performance in micro tubes by the method of liquid crystal thermography. *International Journal of Heat and Mass Transfer* 2007; 50: 4736–4742.

16. Yang CY, Chen CW, Lin TY, et al. Heat transfer and friction characteristics of air flow in microtubes. *Experimental Thermal and Fluid Science* 2012; 37: 12–18.

17. Baek S, Radebaugh R, Bradley PE. A new method for heat transfer coefficient measurements of single-phase fluids during laminar flow in microchannels. *International Journal of Heat and Mass Transfer* 2020; 157: 119891.

18. Wang L, Pan YC, Lee J Der, et al. Experimental investigation in the pressure drop characteristics of supercritical carbon dioxide in the uniformly heated horizontal miniature tubes. *Journal of Supercritical Fluids* 2020; 162: 104839.

19. Wang L, Pan YC, Lee J Der, et al. Convective heat transfer characteristics of supercritical carbon dioxide in vertical miniature tubes of a uniform heating experimental system. *International Journal of Heat and Mass Transfer* 2021; 167: 120833.

20. Rosa P, Karayiannis TG, Collins MW. Single-phase heat transfer in microchannels: The importance of scaling effects. *Applied Thermal Engineering* 2009; 29: 3447–3468.

21. Yang C, Lin T. Heat transfer characteristics of water flow in microtubes. *Experimental Thermal and Fluid Science* 2007; 32: 432–439.

22. Incropera FP, Dewitt DP, Bergman TL, et al. *Fundamentals of Heat and Mass Transfer*. 7th ed. John Wiley & Sons, New Jersey, 2011.

23. Maranzana G, Perry I, Maillet D. Mini- and micro-channels: Influence of axial conduction in the walls. *International Journal of Heat and Mass Transfer* 2004; 47: 3993–4004.

24. Mori Y, Futagami K, Tokuda S, et al. Forced convective heat transfer in uniformly heated horizontal tubes 1st report-Experimental study on the effect of buoyancy. *International Journal of Heat and Mass Transfer* 1966; 9: 453–463.

25. Mori Y, Futagami K. Forced convective heat transfer in uniformly heated horizontal tubes (2nd report, theoretical study). *International Journal of Heat and Mass Transfer* 1967; 10: 1801–1813.

26. Jackson JD, Hall WB, Fewster J, et al. Heat Transfer to Supercritical Pressure Fluids. *UKAEA AERE-R 8158, Design Report 34*.

27. Kakac S. The Effect of Temperature-Dependent Fluid Properties on Convective Heat Transfer. In: *S. Kakac, R.K. Shah, W. Aung (Eds.), Handbook of Single-Phase Convective Heat Transfer*. 1987.

28. Iverson BD, Conboy TM, Pasch JJ, et al. Supercritical $CO_2$ Brayton cycles for solar-thermal energy. *Applied Energy* 2013; 111: 957–970.

29. Wu P, Ma Y, Gao C, et al. A review of research and development of supercritical carbon dioxide Brayton cycle technology in nuclear engineering applications. *Nuclear Engineering and Design* 2020; 368: 110767.

30. Katz A, Aakre SR, Anderson MH, et al. Experimental investigation of pressure drop and heat transfer in high temperature supercritical $CO_2$ and helium in a printed-circuit

heat exchanger. *International Journal of Heat and Mass Transfer* 2021; 171: 121089.

31. Park JH, Kwon JG, Kim TH, et al. Experimental study of a straight channel printed circuit heat exchanger on supercritical $CO_2$ near the critical point with water cooling. *International Journal of Heat and Mass Transfer* 2020; 150: 119364.

32. Park JH, Kwon JG, Kim MH, et al. Experimental investigation of buoyancy effects on local heat transfer of supercritical pressure $CO_2$ in horizontal semicircular tube. *International Journal of Heat and Mass Transfer* 2021; 164: 120496.

33. Liao SM, Zhao TS. Measurements of heat transfer coefficients from supercritical carbon dioxide flowing in horizontal mini/micro channels. *Journal of Heat Transfer* 2002; 124: 413–420.

34. Yang C, Xu J, Wang X, et al. Mixed convective flow and heat transfer of supercritical $CO_2$ in circular tubes at various inclination angles. *International Journal of Heat and Mass Transfer* 2013; 64: 212–223.

35. Cao XL, Rao ZH, Liao SM. Laminar convective heat transfer of supercritical $CO_2$ in horizontal miniature circular and triangular tubes. *Applied Thermal Engineering* 2011; 31: 2374–2384.

36. Yu S, Li H, Lei X, et al. Influence of buoyancy on heat transfer to water flowing in horizontal tubes under supercritical pressure. *Applied Thermal Engineering* 2013; 59: 380–388.

37. Kim TH, Kwon JG, Kim MH, et al. Experimental investigation on validity of buoyancy parameters to heat transfer of $CO_2$ at supercritical pressures in a horizontal tube. *Experimental Thermal and Fluid Science* 2018; 92: 222–230.

38. Theologou K, Mertz R, Laurien E, et al. Experimental investigations on heat transfer of $CO_2$ under supercritical pressure in heated horizontal pipes. *Energy* 2022; 254: 124171.

39. Zhang XR, Yamaguchi H. Forced convection heat transfer of supercritical $CO_2$ in a horizontal circular tube. *Journal of Supercritical Fluids* 2007; 41: 412–420.

40. Wang L, Pan YC, Der Lee J, et al. Experimental investigation in the local heat transfer

of supercritical carbon dioxide in the uniformly heated horizontal miniature tubes. *International Journal of Heat and Mass Transfer*; 159.

41. Dang C, Hihara E. Numerical study on in-tube laminar heat transfer of supercritical fluids. *Applied Thermal Engineering* 2010; 30: 1567–1573.

42. Viswanathan K, Krishnamoorthy G. The effects of wall heat fluxes and tube diameters on laminar heat transfer rates to supercritical $CO_2$. *International Communications in Heat and Mass Transfer* 2021; 123: 105197.

43. Öztabak E, Gökkaya O, Ahn H. Experimental investigation on heat transfer characteristics of supercritical carbon dioxide flowing in horizontal and vertical microtubes. In: *17th UK Heat Transfer Conference (UKHTC2021)*. Manchester, UK, 2022.

44. Öztabak E, Gökkaya O, Ahn H. A novel method of measuring microtube wall temperatures by thermocouples to investigate $sCO_2$ flows. *Applied Thermal Engineering* 2022; 209: 118299.

45. Morgan VT. The Overall Convective Heat Transfer from Smooth Circular Cylinders. In: *T. F. Irvine and J. P. Hartnett, Eds., Advances in Heat Transfer, Vol. 11*. New York: Academic Press, 1975, pp. 199–264.

46. Lemmon EW, Huber ML, McLinden MO. NIST Standard Reference Database 23: Reference Fluid Thermodynamic and Transport Properties-REFPROP, Version 10.0, National Institute of Standards and Technology, Standard Reference Data Program, Gaithersburg.

47. Bergles AE, Simonds RR. Combined forced and free convection for laminar flow in horizontal tubes with uniform heat flux. *International Journal of Heat and Mass Transfer* 1971; 14: 1989–2000.

48. Shah RK, Bhatti MS. Laminar convective heat transfer in ducts. In: *S. Kakac, R.K. Shah, W. Aung (Eds.), Handbook of Single-Phase Convective Heat Transfer*. New York: Willy, 1987.

49. Figliola RS, Beasley DE. *Theory and Design for Mechanical Measurements*. John Wiley & Sons, Hoboken, New Jersey, 2011.

50. Kreith F, Bohn M. *Principles of Heat Transfer*. 6th ed. Brooks/Cole Pub., 2001.

51. Gökkaya O, Öztabak E, Ahn H. Experimental investigation on heat transfer characteristics of supercritical $CO_2$ flowing upward and downward through a microtube at low Reynolds numbers. *Experimental Thermal and Fluid Science* 2022; 110717.